
Towards efficient siRNA delivery and gene silencing kinetics on the single-cell level

Rafał Stanisław Krzysztoń



München 2018

Towards efficient siRNA delivery and gene silencing kinetics on the single-cell level

Rafał Stanisław Krzysztoń

Dissertation

durchgeführt an der Fakultät für Physik
der Ludwig–Maximilians–Universität
München

vorgelegt von

Rafał Stanisław Krzysztoń
aus Drawsko Pomorskie, Polen

München, den 09.08.2018

Erstgutachter: Prof. Dr. Joachim O. Rädler

Zweitgutachter: Prof. Dr. Jan Lipfert

Tag der mündlichen Prüfung: 20.09.2018

Table of Contents

Zusammenfassung.....	v
Abstract.....	vi
1. Introduction.....	1
1.1. Discovery of RNA interference and its consequences.....	1
1.2. siRNA in systemic gene therapy – latest advances in gene delivery systems.....	3
1.3. Applications of microfluidics in bioscience and technology.....	6
1.4. Microfluidic synthesis of nanoparticles	9
1.5. Relevance of single-cell observations in biosciences	11
1.6. Time-lapse microscopy as a tool to investigate single-cell behaviour.....	15
1.7. Scope of presented work	18
2. Experimental methods and approaches.....	18
2.1. Microfluidic chip devices	18
2.1.1. Hydrodynamic focusing micro-mixing chip device.....	18
2.1.2. Microfluidic chip device for calibrating fluorescence intensities	23
2.2. Fluorescence Correlation Spectroscopy (FCS) and confocal microscopy.....	23
2.2.1. Basic theoretical background	24
2.2.2. Autocorrelation function in systems characterized by pure diffusion.....	27
2.2.3. Triplet blinking kinetics.....	29
2.2.4. FCS and Confocal microscopy instrumentation.....	29
2.3. Flow cytometry (FC)	31
2.3.1. Flow cytometry instrumentation	33
2.4. Live – cell Imaging of Single-Cell Arrays (LISCA)	33
2.4.1. Micro-patterned surfaces for cell cultivation	34
2.4.2. Time-lapse microscopy instrumentation	35
2.4.3. Fluorescence background correction algorithm and image analysis.....	35
2.4.4. Fluorescence calibration to protein numbers	37
2.4.5. Data processing and analysis	40
3. Results	41
3.1. mNALP assembly and activity	42
3.1.1. Evaluation of starting solvent conditions	43
3.1.2. Influence of mixing modes and synthesis optimization	45
3.1.3. mNALP stability in blood serum and plasma	49
3.1.4. Cell binding and uptake experiments.....	52
3.1.5. Silencing experiments	55
3.2. siRNA mediated mRNA degradation kinetics.....	56
3.2.1. Dual-reporter assays.....	57

3.2.2. Comparison of single-cell and population-averaged fluorescence analysis	59
3.2.3. Kinetic analysis of mRNA expression time courses	63
3.2.4. Translation inhibition experiments.....	66
3.2.5. Correlation analysis.....	68
3.2.6. Codon optimality of eGFP- and CayRFP-mRNA constructs.....	74
4. Conclusions.....	78
Appendix.A1. Protocols	81
A1.1. Master micro-structures for stamp and micro-chip preparation.....	81
A1.2. Fabrication of microfluidic chip devices.....	82
A1.3. Cell culture	82
A1.4. mNALP assembly and activity.....	83
A1.4.1. Materials.....	83
A1.4.2. dsDNA and siRNA sequences.....	83
A1.4.3. Annealing of complementary oligonucleotides.....	84
A1.4.4. Blood serum and blood plasma collection.....	84
A1.4.5. Preparation of mNALP samples.....	84
A1.4.6. Cell binding and uptake experiments – Confocal Microscopy.....	85
A1.4.7. Cell binding and uptake experiments – Flow Cytometry	86
A1.4.8. mNALP-induced silencing experiments – luciferase assay	87
A1.5. siRNA mediated mRNA degradation kinetics.....	87
A1.5.1. Surface patterning and microscopy slide preparation.....	87
A1.5.2. <i>In vitro</i> transcription.....	88
A1.5.3. LISCA - silencing experiments	88
A1.5.4. LISCA – translation inhibition experiments.....	90
A1.5.5. Protein expression and purification.....	91
A1.5.6. Plasmid and siRNA sequences, plasmid maps	91
Appendix.A2. Related publications.....	99
Appendix.A3. Conference contributions.....	99
Appendix.A4. List of abbreviations.....	100
Appendix.A5. List of figures and tables.....	102
A5.1. Figures	102
A5.2. Tables.....	104
Acknowledgements	104
Bibliography	105

Zusammenfassung

RNA-Interferenz (RNAi) ist ein natürlicher sequenzspezifischer Mechanismus der posttranskriptionellen Genregulation, der von kurzen, doppelsträngigen RNA-Fragmenten (small interfering RNAs (siRNA)) ausgeführt wird. Trotz ihres hohen therapeutischen Potenzials bleibt die sichere und effiziente systemische Abgabe von siRNAs an eine große Anzahl von erkrankten Zellen, um einen therapeutischen Gen-Knockdown auszulösen, eine Herausforderung. Darüber hinaus werden neue quantitative Methoden zur schnellen und präzisen Beurteilung der Aktivität von siRNA-basierten Therapeutika benötigt.

In dieser Arbeit wurden zunächst Folat-gerichtete monomolekulare Nucleinsäure / Lipid-Partikel (FolA-mNALPs) entwickelt, die mit Hilfe mikrofluidischer Methoden hergestellt wurden. Nachfolgend wurde die Funktionalität dieser Partikel hinsichtlich der zukünftigen Verwendung als siRNA-Lieferanten getestet. Zweitens wurde die Einzelzellkinetik des Gen-Silencing durch siRNA mit mikrostrukturierten Zellkultivierungssubstraten in Kombination mit Zeitraffer-Fluoreszenzmikroskopie (Life-Cell-Imaging auf Single-Cell-Arrays, LISCA) quantifiziert.

Insbesondere konnten wir zeigen, dass mikrofluidische Selbstorganisation kombiniert mit rationalem Design der Lipidformulierung zu Nanopartikeln kleiner Größe und enger Größenverteilung führt, die im Durchschnitt einzelne siRNA-Moleküle enthalten, welche mit einer einzelnen Lipiddoppelschicht bedeckt sind (mNALP). Die Stabilität von Folat-funktionalisierten mNALPs in biologischen Flüssigkeiten und ihre biologische Leistungsfähigkeit hinsichtlich der zellulären Internalisierung und Gen-Silencing wurde untersucht. Kleine Größen, effizientes Targeting und vorgestellte Gen-Silencingfähigkeiten im Anschluss an die erleichterte Freisetzung aus Endosomen machen mNALP zu einem vielversprechenden System für die zukünftige Entwicklung eines *in vivo* siRNA-Wirkstoffs.

Darüber hinaus untersuchten wir mit LISCA die Größenordnung des durch siRNA induzierten mRNA-Abbaus. Durch mathematische Modellierung der Genexpression und Anpassung der Expressionszeitverläufe konnten die Populationsverteilungen der biochemischen Raten, einschließlich der mRNA-Abbauratenkonstanten für einzelne Zellen bestimmt werden. Die Expressionszeitverläufe wurden durch Überwachung der dynamischen Veränderungen der Einzelzellfluoreszenzintensitäten von Reporterproteinen (eGFP-Ziel und CayRFP-Referenz) bestimmt. Die daraus resultierenden kinetischen Parameter erlaubten sowohl die Quantifizierung der Effizienz des Gen-Silencing als relative Änderung der mRNA-Abbauraten, als auch die Identifikation der Subpopulationen von Zellen, welche von der siRNA-Aktivität betroffen sind. Zusätzlich konnten durch Analyse von Korrelationen zwischen kinetischen Parametern von CayRFP- und eGFP-Expression die Eigenschaften der mRNA-Abgabe und Expressionskinetik bestimmt werden. Der vorgestellte Ansatz ermöglicht die genaue Quantifizierung der Aktivität von siRNA-basierten Therapeutika auf eine akkurate und schnelle (<30h) Weise.

Abstract

RNA interference (RNAi) is a natural sequence-specific mechanism of post-transcriptional gene regulation mediated by short, double stranded RNA fragments *e.g.* small interfering RNAs (siRNA). Despite its high therapeutic potential, the safe and efficient systemic delivery of siRNAs into a large number of diseased cells to trigger therapeutic gene knockdown remains challenging. Moreover, novel quantitative methods for assessing activity of siRNA-based therapeutic agents in a fast and precise manner are needed.

In this work, we first present the development of the folate-targeted monomolecular nucleic acid/lipid particles (FolA-mNALPs) formed using microfluidic-based method and studied their functionality regarding prospective use as a siRNA delivery agent. Secondly, we quantify the single-cell kinetics of siRNA-mediated gene silencing using micro-patterned cell cultivation substrates combined with time-lapse fluorescence microscopy (life-cell imaging on single-cell arrays, LISCA).

In particular, we demonstrate that microfluidic self-assembly combined with rational design of lipid formulation results in nanoparticles of small size and narrow size distribution that on average contain a single siRNA molecule covered with a single lipid bilayer (mNALP). We investigate the stability of folate-functionalized mNALPs in biological fluids, and their biological performance in terms of cellular internalisation and silencing efficiency. Small sizes, efficient targeting and silencing capability following facilitated endosomal release make mNALP a promising system for the future development of an *in vivo* siRNA delivery agent.

Furthermore, using LISCA we investigate the magnitude of siRNA-induced mRNA degradation. By mathematical modelling of gene expression and fitting of expression time-courses we obtain the population distributions of biochemical rate constants, including single-cell mRNA degradation rate constants. The expression time-courses are gained by monitoring the dynamic changes in single-cell fluorescence intensities of reporter proteins (eGFP target and CayRFP reference). Obtained kinetic parameters allow us to quantify the silencing efficiency as a relative change in mRNA degradation rate constants, to identify the subpopulations of cells affected by siRNA activity and, by analysis of correlations between kinetic parameters of CayRFP and eGFP expression, to infer on the properties of mRNA delivery and expression kinetics. The presented approach allows for the precise quantification of the activity of siRNA-based therapeutics in an accurate and fast (<30h) manner.

1. Introduction

1.1. Discovery of RNA interference and its consequences

For years, the biological functions of RNA were thought to be limited to information transfer and decoding or structural functions in forms of messenger (mRNA), transfer (tRNA) and ribosomal RNA (rRNA) respectively. Although, the discoveries of last 40 years have extended our understanding of RNA functionality giving evidence of *e.g.* enzymatic activity of RNA.¹ What could be even more important, the revealed regulatory behaviour of non-coding RNA forms have revolutionized our understanding of biological plasticity of functional gene regulation and its impact on variety of natural processes of embryo development, cell differentiation and many others.²

The most prominent evidence of the significance of RNA-mediated post-transcriptional regulation of genes is the process of RNA interference (RNAi). RNAi relies on selective enzymatic degradation of targeted mRNA or blocking of protein translation that is led by short complementary RNA fragments. The mechanism is highly specific towards targeted mRNA sequences and is widely spread among many eukaryotic organisms including roundworms (*C.elegans*),³ flies (*D. melanogaster*),⁴ plants (*P. hybrida*),^{5,6} yeasts (*S.pombe*),⁷ mammals⁸ including humans⁹ and many others. The core cascade of RNAi pathway consists of two enzymatic processes performed sequentially by Dicer endoribonuclease and RNA-induced silencing complex (RISC).¹⁰ Dicer processes precursor forms of non-coding RNAs - double stranded (dsRNA), short hairpin (shRNA) or pre-micro RNA (pre-miRNA). Namely, they are cleaved into active, 20-25 bp, helical forms - double strands of small interfering RNA (siRNA) or short hairpins of microRNA (miRNA). miRNA or the guiding strand of siRNA are further incorporated into the RISC complex and serve as a targeting templates to recognize mRNA molecules of complementary sequence. siRNA-guided recognition leads to enzymatic degradation of mRNA by Argonaute 2 (AGO2) endonuclease that constitutes the active subunit of RISC. In contrast, miRNA repress the translation of encoded proteins by ribosome blocking activity of RISC complex. Importantly, it has been shown that introduction of the short double-stranded siRNA into the cells results in successful gene silencing circumventing Dicer activity.¹¹ Aside those two general mechanisms multiple other RNAi-related pathways were discovered revealing wide-spread relevance of the process.²

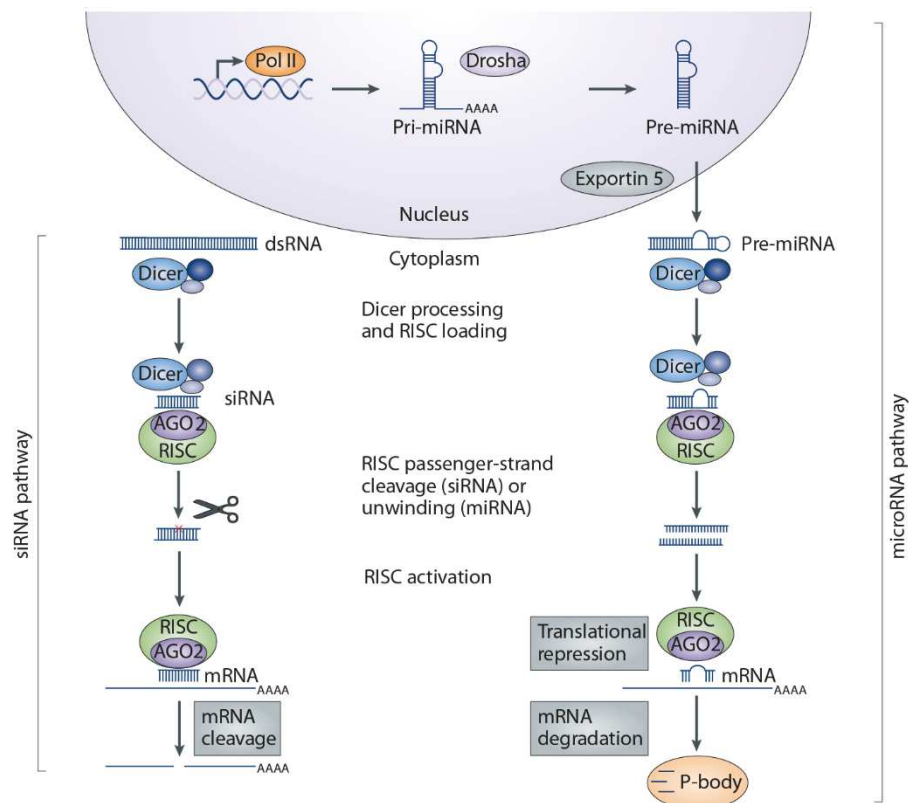


Fig.1.1. Two major pathways of RNA interference in mammalian cells

In the siRNA pathway starts by cleavage of double stranded RNA into short 21-25 bp siRNA fragments by Dicer enzyme. siRNA is further incorporated into AGO2 and RISC complex is formed. The perfect complementarity of siRNA guide strand to its mRNA target leads to enzymatic cleavage of mRNA by catalytic domain of AGO2. The cascade can be also triggered by introduction of siRNA in intermediate steps. The endogenous miRNA pathway starts with primary micro RNA (pri-miRNA) transcribed by polymerase II (Pol II) in the cell nucleus. Upon processing of pri-miRNA by Drosha enzyme complex into precursor miRNA (Pre-miRNA) and nuclear export into the cytoplasm mediated by Exportin 5, the Pre-miRNA template enters the main Dicer-RISC pathway. The imperfect base pairing within miRNA releases the passenger strand leaving the mature miRNA bounded to active RISC. The recognition of targeted mRNA leads to effective inhibition of translation. RISC binding may also lead to degradation of mRNA in processing (P)-bodies. Reprinted with permission from De Fougères et al.¹⁰ Copyright (2007) Springer Nature.

Steadily unfolding research has shown that RNAi plays important roles in cell differentiation,^{12, 13} embryonic development,^{14, 15} cancer metabolism¹⁶⁻¹⁸ and processes of viral infection and host response to it^{19,20} etc.. In particular, it is proposed that RNAi pathways have opened the area for co-evolutionary interaction of host organisms and viral parasites. Host organism can use RNAi as a defence mechanism that provides control over components of innate immunity pathways by modulating gene expression using genome-encoded miRNAs^{21, 22} or as a direct defence against the viral gene expression.²³ On the other hand, viruses can modulate host responses by blocking the resistance

mechanisms.^{23,24} Furthermore, the genetically-encoded forms of miRNA have been proven to play crucial role in meiotic maturation of mice oocytes,^{25, 26} during zygotic development of zebrafish embryos,¹⁵ hematopoietic lineage¹² and dendritic cell differentiation.¹³ The characteristic distorted miRNA profiles have been observed in different types of tumours and constitute a sensitive cancer biomarkers.¹⁸ Moreover, the exosome-derived miRNA that are secreted from tumour cells have been shown to interact with stromal cells in the tumour micro-environment modulating cancer progression, metastasis, angiogenesis and escape from immune recognition.¹⁷ siRNA- and shRNA-driven RNA interference have been also successfully utilized for genome-scale loss-of-function screens (high-throughput RNAi screens) in cultured cells and model organisms.^{27,28} The method facilitates broad modality in analysis of gene functions due to high specificity of optimized siRNA sequences towards their mRNA targets.²⁹

1.2. siRNA in systemic gene therapy – latest advances in gene delivery systems

The high modality in terms of sequence-specific silencing, practical flexibility and sequence specificity of RNAi opened a new field for therapeutic endeavours. By exploiting the siRNA-induced RNAi, silencing of nearly any gene can be achieved that reveals broad therapeutic potential of siRNA beyond the prospects for typical small-molecule drugs. Moreover, single siRNA-loaded RISC complex can be responsible for degradation of multiple mRNA molecules that is reflected in high efficiency in gene silencing.³⁰ RISC recycling ensures efficient therapeutic effect for 3-7 days in rapidly dividing cells and for up to several weeks in non-dividing cells.³¹ Importantly, the use of intermediate, short siRNA is crucial from a point of pharmaceutical interest as it reduces the potential for innate immune interferon response that can occur due to the interactions of long (>30 bp) shRNA with intracellular RNA receptors.³² The therapeutic action of synthetic siRNA against *e.g.* liver cirrhosis,³³ hepatitis B virus (HBV),³⁴ ovarian cancer,³⁵ bone cancer,³⁶ hypercholesterolaemia³⁷ and many other diseases have been shown and many clinical trials have been initiated.³⁸ Despite evidence that "naked", chemically-modified forms of siRNA have been effective in targeting particular brain³⁹ and lung⁴⁰ diseases, the systemic delivery of therapeutic siRNA to the most of tissues in human body still requires systems to facilitate efficient transfection of targeted cells.

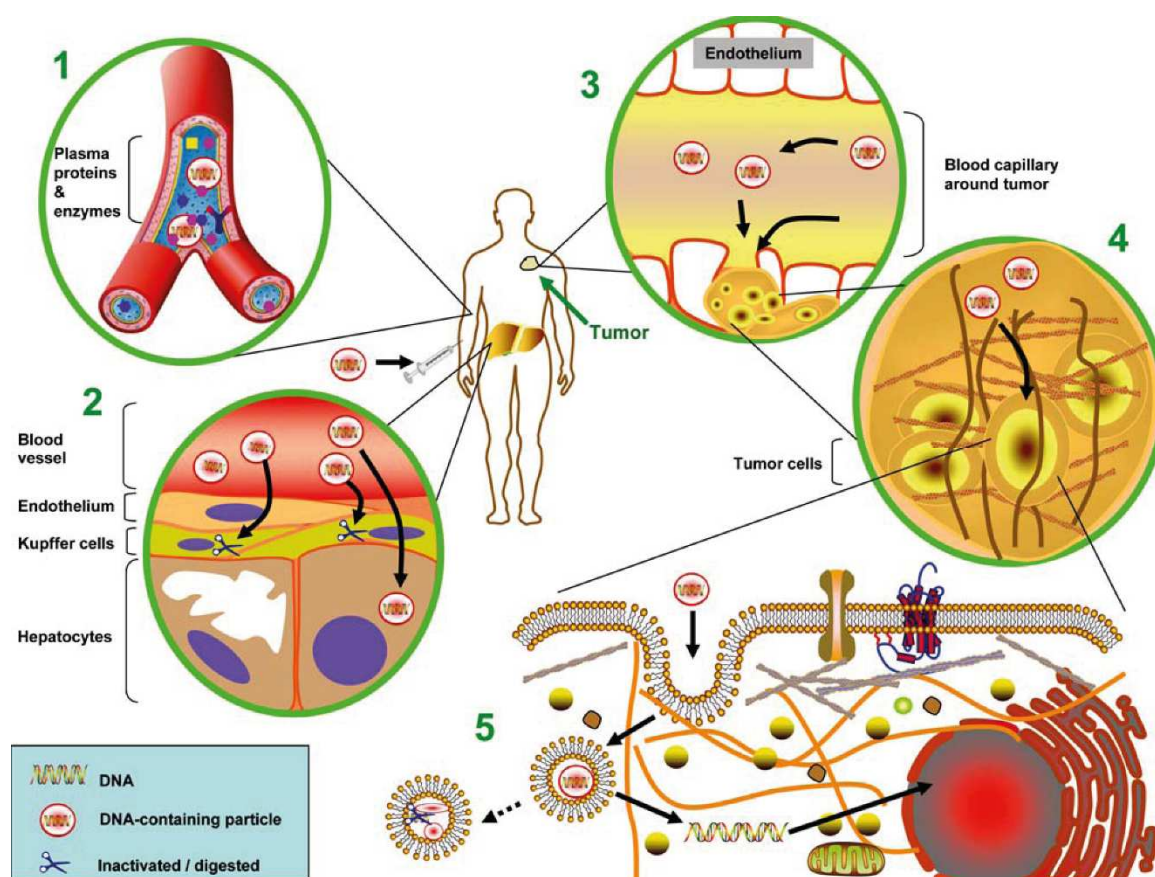


Fig.1.2. Barriers on efficient systemic delivery of nucleic acid nanoparticles

Following intravenous injection the nanoparticles can bound to serum protein or being opsonized by antibodies leading to elimination from bloodstream by components of complement system [1]. Particles can be eliminated in the liver by activity of Kupffer cells that limits their activity in the targeted side of the disease, including hepatocytes [2]. Loose structure of blood vessels in tumour surrounding allow the relatively large (~100 nm) nanoparticles to accumulate in the tumour tissue (the enhanced permeability and retention (EPR) effect) [3]. Additionally, access to the cell surface is limited by the dense structure of extracellular matrix that is penetrable only by small and shielded nanoparticles [4]. Finally, when the particles reach the side of therapeutic action and are successfully internalized by diseased cells e.g. by endocytosis, they need to be capable to escape the endosomes efficiently before being degraded in late endosomes/lysosomes [5]. Reprinted with permission from Szoka et al.⁴¹ Copyright (2007) Springer Nature.

Therapeutic nucleic acids (NAs) are not easily incorporated by cells and require involvement of active transport mechanisms to pass the cellular membranes due to its high molecular weight (~13 kDa in case of siRNA) and highly negative surface charge. Moreover, they are prone to degradation by nucleases present in the bloodstream and extracellular matrix. For this reason, multiple methods for selective and safe delivery of exogenous nucleic acids into a large numbers of cells in human body are under constant development. Both, viral and non-viral approaches have been verified for systemic delivery of NAs. Despite the high efficiency of viral vectors their limited packing capacity and

safety concerns have spurred the quest for alternative, non-viral systems.⁴² The research on self-assembled nucleic-acid-based nanoparticles has made significant progress by exploiting the synergies between material science and nanotechnology. Some of systemic delivery issues have been partially resolved by using complexes of NAs assembled with cationic agents (*e.g.* lipids or polymers). Multiple of those first- and second-generation systems exploit the relations between particle structure and function.⁴³ For instance, tuned composition of particle-forming lipids can lead to structural changes in lipid membrane structure leading to triggered transitions into endosomolytic inverted hexagonal phase.^{44, 45} Similarly, polyethyleneimine (PEI) delivery systems exploit the "proton sponge" effect of polymer swelling in low-pH endosome environment to facilitate efficient release.⁴⁶ Further advances in non-viral lipid-based delivery of siRNA include the development of stable nucleic acid/lipid particles (SNALP) that present efficient therapeutic action against HBV,⁴⁷ the synthesis of novel lipid-like molecules (lipoids) and the screening of produced chemical libraries for increased efficiency;⁴⁸ use of ionizable lipids for improved escape from endosomes⁴⁵ and tunable microfluidic-based synthesis of lipid nanoparticles (LNPs).⁴⁹

In general, three key criteria of the non-viral delivery systems need to be met. Namely, a) the nanoparticles need to encapsulate and shield the NAs efficiently against the degradation of nucleases and opsonisation in bloodstream, b) the nanoparticles need to be provided with selective targeting method coupled with effective mechanism for the entry into the cell c) the synthesis needs to be robust, easily scalable and yield small particles with narrow size distribution and controlled structure.

In particular, the stability of nanoparticles is commonly increased by surface coating with polyethylene glycol (PEG). PEG chains provide a steric hindrance on interactions with blood proteins and the components of complement system.⁵⁰⁻⁵³ It also prevents nonspecific interaction with cell membranes and unwanted side effects in healthy cells. However, the PEG-shielding can also interfere with the release of particles from endosomes into the cell cytoplasm. For this reason, several detachment strategies (*e.g.* use of pH-cleavable chemical linkers like AzMMMAn) can be introduced in order to remove the PEG-grafting layer from the nanoparticle surface on demand, *i.e.* due to the pH drop in the late endosomes.^{54, 55}

Moreover, the targeting to a specific cell types or cells in distinct metabolic state can be achieved using various surface ligands that can trigger specific uptake of nanoparticles by receptor-mediated endocytosis.^{56–59} Targeting, used together with PEG-shielding, minimizes the potential side effects in non-targeted cells. Here, the non-specific cell binding is reduced and the biological effect of delivered NAs is limited to the cells, tissues or organs targeted. The representative examples of successful targeted delivery systems for siRNA include Genospheres, SNALPs and folate- or GalNAc-targeted lipo- and polyplexes.^{52, 56–61}

Finally, the colloidal properties of NPs determine their pharmacokinetics. Aspects, such as particle morphology, zeta potential and size distribution have significant influence on their biological functions *in vivo*.^{62, 63} Large (>100 nm) and charged particles are prone to protein absorption, fast clearance from the bloodstream and cannot penetrate the solid tumours and dense tissues.⁴¹ Contrary, the small (<50 nm) nanoparticles can diffuse through the structure of extracellular matrix and show increased efficiency of the drug delivery into solid tumours.^{64, 65} Recently, novel microfluidic synthesis methods have improved the control over the size and size polydispersity of formed nanoparticles.^{49, 66–70} In the future, the method can provide an efficient control over the self-assembly allowing for rational bottom-up design of particle structure and functionality.

1.3. Applications of microfluidics in bioscience and technology.

Currently, the microfluidic technology have found numerous applications, improving analytical and preparative methods for chemical synthesis, biological analysis, cell biology and many other disciplines. Particularly, the small sample volumes, precise control of reaction micro-environment and facilitated automation of sequential processes show great benefits in development of high-throughput screening methods or lab-on-chip approaches to improve standard biochemical assays.

The major premise of microfluidic technology lies in the employment of the unique characteristics of fluid flow in the microscopic scale.^{71, 72} Conditions of fluid flow in micro-scale systems are determined by the relation between the magnitudes of viscous and inertial effects. The quantity describing the relative contributions of both phenomena on fluid behaviour is the dimensionless Reynolds number given by the relation:

$$Re = \frac{\rho L_h u_{ave}}{\mu} \quad (\text{eq.1.1})$$

where: L_h is the characteristic length scale (*e.g.* the diameter of the micro-channel), u_{ave} is the average velocity of the flow, ρ is the fluid density and μ is its viscosity. Based on empirical studies, the Reynolds number values larger than 2000 describe turbulent flows where the inertial forces are dominant. On the other hand, the values below 1000 correspond to laminar (streamline) flows. In this regime, dominated by viscous contributions, flow loses significantly its chaotic nature and occurs in parallel layers with no disruption between them. The laminar flow regime is dominant in micro-channels due to their small dimensions, where the speed of flows often would have to exceed the speed of sound in order to enter the turbulent regime.

The increased determinism of the flow behaviour allows for a precise control in processing small sample volumes (*e.g.* in droplet microfluidics approaches⁷³), for manipulation on micrometer length scales^{74–76} and to exploit micro-scale transport phenomena^{77, 78} *etc.* Among others, the successful execution of those principles allowed for high-throughput screens of protein crystallization conditions using micro-droplets,^{79,80} size-dependent cell sorting,⁷⁵ single-cell trapping⁸¹ or control over compound gradients in optimizing cell culture conditions.⁸²

Moreover, development of soft lithography in PDMS allowed for fast prototyping and fabricating devices⁸³ that, when optimized, can be incorporated as a generic components into a elaborative integrated platforms.⁸⁴ Due to automated sequential fluid handling methods⁸⁵ and possibilities for incorporation of the detection units within the single multifunctional on-chip device⁸⁶ the entire pipeline of analytical procedures can be executed within one chip and with minimal sample volume requirements. The most prominent examples of such systems are the microfluidic-based digital PCR systems,^{87,88} single cell sequencing^{89, 90} and protein crystallization assays^{79, 91} accompanied by multiple others.^{92–94}

Microfluidics have also found applications in cell and tissue biology. The significant advantages compared with conventional methods arises here from the increased control of the cell micro-environment and opportunities to incorporate fluid flows or mechanical forces that all together brings the assays closer to *in-vivo*-like conditions.⁹⁶ In particular, it was shown that mouse fibroblasts reveal increased viability when exposed to CdSe/ZnSe quantum dots under flow conditions in microfluidic device when compared to

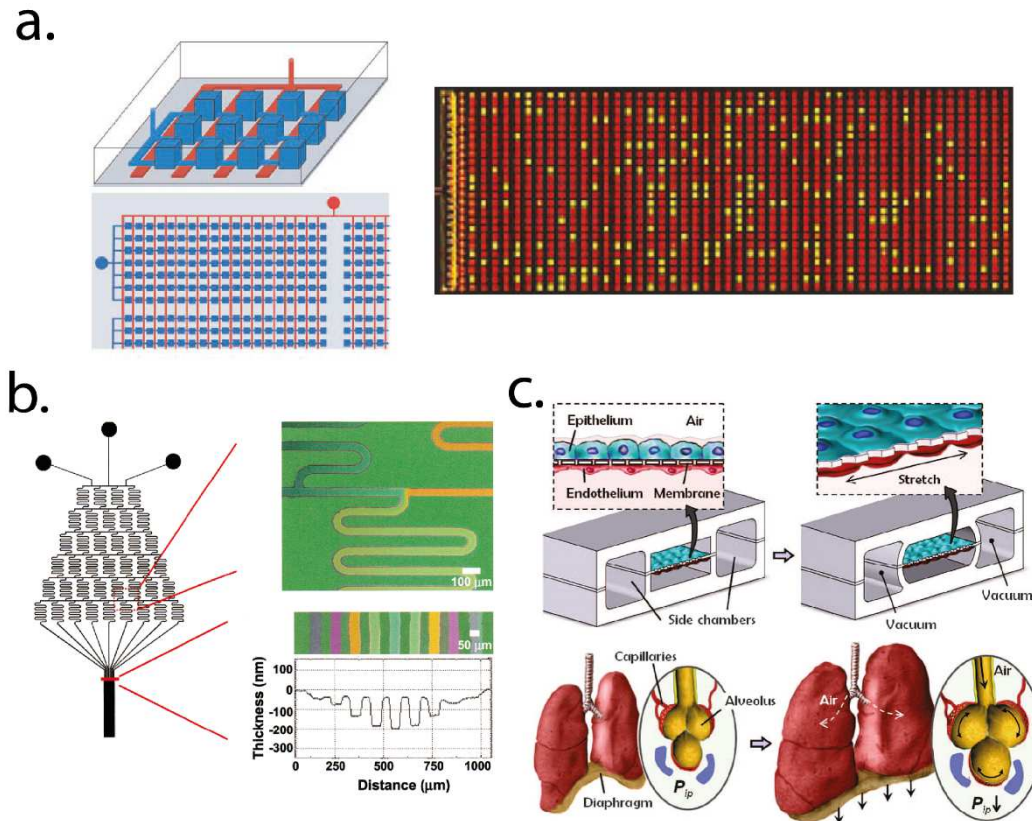


Fig.1.3. Examples of microfluidic applications in bioscience and technology

a) The single-cell digital PCR chip design (left) consists of micro-chambers (blue) separated using pneumatic valve system (red). Each chamber can entrap a single bacterium cell. The outcome of single-cell PCR analysis of bacteria extracted from hindgut content of a single *Z. nevadensis* (termite) individual (right). Red signal is related with 16S rRNA gene present in multiple bacteria species. Green signal indicates presence *FTHFS* gene specific to bacteria activating homoacetogenesis pathway. b) The microfluidic chip design to generate concentration gradients (left). The gradient of hydrofluoric acid (HF, middle inlet channel) was generated in stepwise dilutions with water (side channels). The colors in close-up frames indicate the depth of FH-etched SiO_2 micro-channels (right). The depth profile is also shown in the graph in bottom right c) The microfluidic device mimicking in vivo environment of breathing lung (top). The alveolar-capillary barrier was modelled by tissue grown on flexible, thin and porous PDMS membrane inside compartmentalized channels. The contraction forces were applied by changing the pressure within adjacent chambers causing mechanical stretching of the membrane. Similar changes in the lung membranes are present when the movement of the diaphragm causes changes in intrapleural pressure (bottom). Adapted with permission from: a) Ottesen et al.⁸⁷ Copyright (2006) The American Association for the Advancement of Science., b) Jeon et al.⁷⁷ Copyright (2000) American Chemical Society. and c) Huh et al.⁹⁵ Copyright (2010) The American Association for the Advancement of Science.

standard assays.⁹⁷ Recent years have brought also numerous approaches to develop biomimetic systems resembling the organ-level functions like *i.e.* blood-brain barrier models,⁹⁸ “lung-on-chip”,⁹⁵ “gut-on-chip”⁹⁹ or “liver-on-chip”¹⁰⁰ systems. For instance, it was shown that exposition to mechanical strains in “lung-on-chip” system that are similar to those occurring while breathing altered responses of cultured tissues in terms of toxic and inflammatory responses to silica nanoparticles. Similarly, shear forces caused by flow in “gut-on-chip” system improved the ability to sustain intestinal microbe co-cultures. Those and similar approaches can also improve the reliability of *in vitro* assays in terms of novel drug development and toxic responses to therapeutic nanoparticles. Furthermore, the multiple techniques for cell trapping, single cell detection and single-cell lysate analysis spurred the efforts in cell-to-cell variability investigations^{94,101–103} that are discussed in further sections.

1.4. Microfluidic synthesis of nanoparticles

The microfluidic technology offers a well-controlled environment for synthesis of inorganic and organic nanoparticles. Gained control facilitates precise tuning of particle properties that includes size and size distribution. As mentioned before, those two parameters are of crucial importance in terms of *in vivo* performance of gene delivery systems. Microfluidic synthesis is also easily scalable without losses in nanoparticle quality that allows for production of significant amounts of the product for therapeutic use.¹⁰⁴

Generally, in case of inorganic nanoparticles the synthesis occurs by controlled nucleation and growth that might be triggered by several factors including changes in temperature or relative concentration of substrates.¹⁰⁵ Obtaining narrow size distribution requires homogenous, rapid nucleation and subsequent growth to the desired size in an absence of further nucleation. Those processes can be tuned by control over time of reagent mixing, reaction temperature and reaction time. In conventional macroscopic scale methods all of mentioned parameters can vary significantly within a sample leading to broadly distributed local mixing times, temperature and concentration gradients and uncontrolled reaction times. In contrast, microfluidic approaches offer precise control over mixing times by varying solvent flow rates or channel geometry. The temperature gradients are also reduced due to better heat transfer related with large surface area of the sample and small volume. The reaction time can be tuned by micro-channel length that directly corresponds to incubation times or by adding the quenching agents at precise downstream

channel locations during the process of particle formation.¹⁰⁶ In particular, two-phase droplet mixers based on chaotic advection¹⁰⁷ were used with success to synthesize *e.g.* quantum dots, gold and iron oxide nanoparticles.^{108–110} As a result, the control over the size and polydispersity of quantum dots, which relate directly to their spectral properties was achieved. Similarly, the system allowed for synthesis of gold nanoparticles of controlled size and shape or iron oxide nanoparticles with high magnetization.

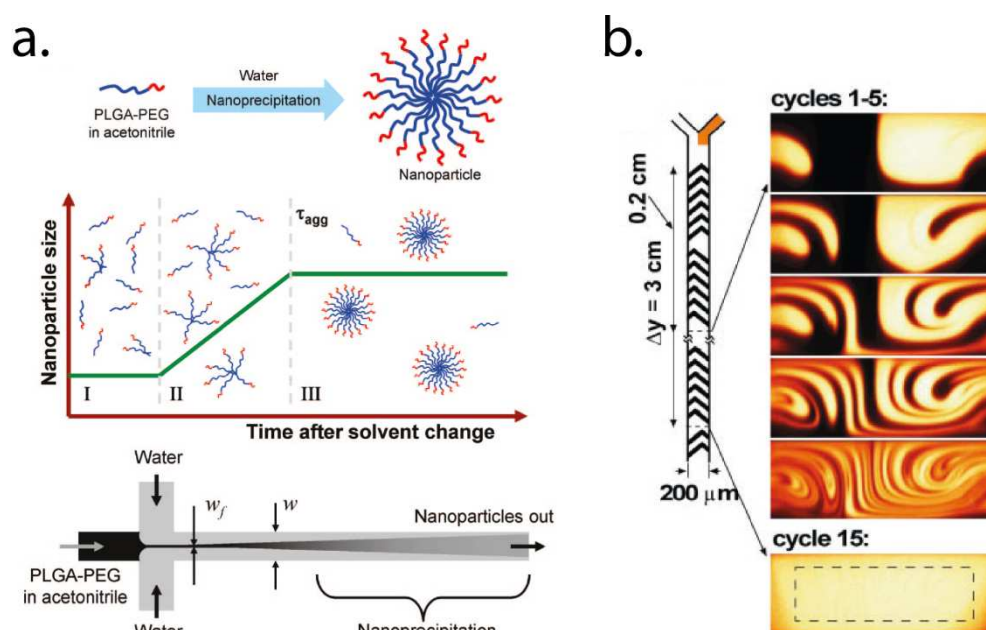


Fig.1.4. Continuous flow microfluidic micro-mixers

a) The PLGA-PEG nanoparticles formed by solvent exchange method on hydrodynamic-focusing microfluidic device (top). The nanoprecipitation of particles happens by nucleation and aggregation within characteristic time scale (τ_{agg} , middle). When the mixing is performed in a micro-scale the diffusive mixing time of solvents is shorter than the time of forming particles causing homogenous environment of the particle synthesis (bottom). b) The diffusive mixing time can be shorten even more by complex folding of mixed fluids caused by herringbone micro-stirring structures within the channel. The perturbations in flow profile increase the contact area between the fluids and shorten the diffusive distance between the solvent layers. Adapted with permission from: a) Karnik et al.⁶⁶ Copyright (2008) American Chemical Society., b) Stroock et al.¹¹¹ Copyright (2002) The American Association for the Advancement of Science.

Amphiphilic organic molecules, like *e.g.* lipids or block copolymers can self-assemble into nanoparticles when they experience change in the quality of surrounding solvent. A common way to execute the solvent exchange is to mix the solutions of particle-forming molecules (*e.g.* in alcohol) with anti-solvent (*e.g.* water). Similarly like in case of inorganic particles, the kinetics of the solvent exchange relates with the homogeneity of nanoparticle nucleation and the time of mixing solvents directly influence the size and size

distribution of formed particles.¹¹² In particular, if the mixing time exceeds the characteristic timescale for molecules to nucleate and particles to grow (between ~10 and 100 ms depending on the size of amphiphilic molecules) the particle assembly happens under varying solvent quality.¹¹³ This prevents efficient stabilization of nanoparticles where effects related with mass transport can lead to large, polydisperse particles of varying structure and composition. The described scenario takes place when macroscopic mixing is introduced. In contrast, if the mixing time is shorter than the characteristic timescale of particle aggregation the hydrophilic parts of molecules (e.g. PEG chains) efficiently stabilize the nanoparticle leading to formation of uniform particles of small size.¹¹⁴ Shortening of solvent mixing times can be accomplished using microfluidic mixing devices, which enable control of the mixing kinetics and by that facilitate tuning of size and polydispersity of formed nanoparticles.

Several microfluidic micro-mixers facilitating rapid solvent exchange have been reported.¹¹⁵ Among the most widely used are hydrodynamic-focusing mixers⁶⁶ and continuous flow mixers with stirrer micro-structures (e.g. herringbone micro-mixer¹¹¹). In hydrodynamic focusing geometry the solvent stream is squeezed between two adjacent water streams and mixing occurs rapidly due to diffusion in the outlet channel. The micro-stirrers positioned alongside the mixing channel geometry result in complex folding of mixed fluids and increasing the contact area for improved diffusive mixing. Multiple polymer and lipid nanoparticle systems have been reported all of which have presented tunable sizes, narrow size distribution, high batch-to-batch reproducibility and increased loading with drugs and therapeutic nucleic acid compared with conventional solvent exchange methods.⁶⁹ Special distinction should be granted to lipid nanoparticles (LNPs) composed of novel ionisable lipid (DLinKC2-DMA) and siRNA that were prepared using herringbone micro-mixer¹¹⁶ since this drug delivery system have presented high performance during *in vivo* trials for siRNA-based gene therapy.¹¹⁷

1.5. Relevance of single-cell observations in biosciences

The cell is a basic structural and functional unit of living organisms. Most molecular processes occur on the cellular level, they act out their own specialized function, they are capable of reacting to external micro-environment and of being involved in complex signalling with other cells in their surroundings. The complex behaviour of cells within clonal populations, tissues and organs emerge as a consequence of single-cell interactions

and decision making. Importantly, it was shown that even genetically identical cells from the same population present tremendous differences in *e.g.* mRNA and protein levels or phenotype variations.^{118, 119} Understanding the behaviour of single cells is often crucial to resolve the details of processes that, as a consequence, emerge on the higher levels of biological organization. Although, most cellular processes including molecular network interactions, dynamic responses and cell morphology are examined by cell-population-average techniques where the single cell information is lost.

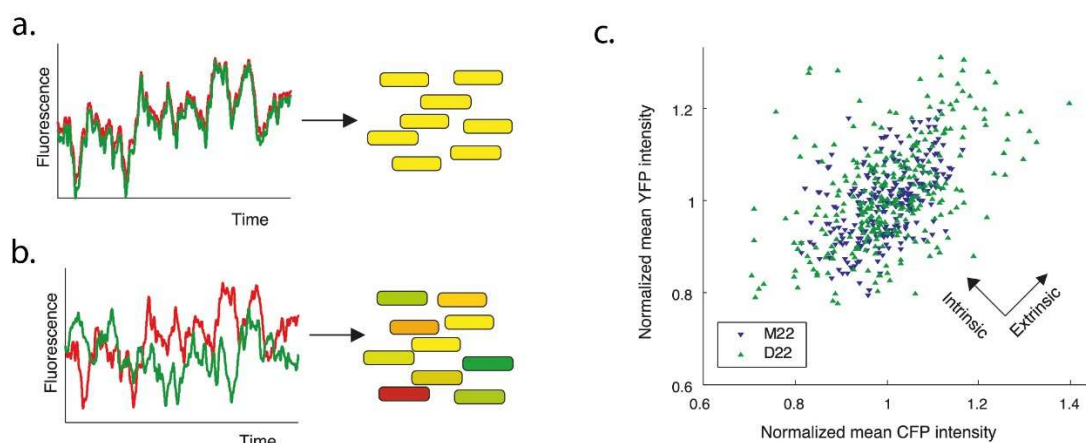


Fig.1.5. Estimation of intrinsic and extrinsic cellular noise contributions

Two genes controlled by identical regulatory sequences (*e.g.* CFP and YFP presented in green and red respectively) can serve as system decoupling the intrinsic and extrinsic contributions to the noise in bacteria. a) In the absence of intrinsic contributions, the amount of both fluorescent proteins and thus the single-cell fluorescence intensity fluctuate in a correlated fashion. Although, the protein levels might vary significantly from cell to cell within the clonal population due to extrinsic contributions. b) The expression of proteins in individual cells become uncorrelated as the stochastic effects of biochemical noise (intrinsic cellular noise) contribute to the variability. c) The plot presenting the population distributions of YFP vs. CFP normalized fluorescence derived from single-cells of clonal *E.coli* populations. Each point represents the mean fluorescence intensity of each cell. The spread of the scattered cluster perpendicular to the diagonal reflects the intrinsic noise contribution whereas spread parallel to the diagonal corresponds to extrinsic effects. Adapted with permission from Elowitz *et al.*¹²⁰ Copyright (2002) The American Association for the Advancement of Science.

The non-genetic cell-to-cell variability is referred frequently as cellular noise and is divided within framework of intrinsic and extrinsic contributions. The intrinsic noise indicates the variation within identically-regulated quantities occurring within the same cell. The intrinsic noise arises from the inherently probabilistic and discrete nature of biochemical reactions. In particular, the intrinsic contributions in cellular noise present in transcription and translation have been extensively investigated on the single-cell and molecular level.^{120, 121} Moreover, there is evidence that certain motifs of molecular

signalling pathways might evolve to regulate the uncertainty levels caused by intrinsic noise within the regulatory networks.^{122, 123} The examples of such stochastic regulatory systems have been reviewed.^{120–125} The influence of stochastic contributions on protein and mRNA levels have been investigated in the genome-wide studies on cell-to-cell variability in clonal populations of *E.coli* and *Saccharomyces*.^{118, 126} Although the molecular make-up of the genetically identical cells revealed vast cell-to-cell variations, the studies indicate that the origins of observed variability come from the upstream influences rather than from the intrinsic expression noise directly.^{127, 128} Those upstream influences refer to the interactions between investigated stochastic system and other regulatory elements originating from inside the cell or its environment. Discussed effects may affect multiple genes simultaneously contributing to the variations in identically-regulated quantities occurring between individual cells in clonal population and therefore constitute the extrinsic effects in cellular noise. However, the upstream variability might originate from the stochastic as well as deterministic influences. Moreover, even if the upstream source has probabilistic contributions, the system in total might not be stochastic. For instance, there is evidence that an increased number of regulatory mechanisms (also those of stochastic nature) contribute to increased robustness of the system to the intrinsic noise.^{129–132} Interestingly, this observation might explain the tendency of biological systems to evolve into the complexity observed in the eukaryotic domain of life. Although, there are empirical difficulties in clearly defining the magnitude of stochastic and deterministic influences on cell-to-cell variability, especially at the level of cell activity or phenotype, the determinism can be qualitatively stated by correlating the predetermining factors with the observed cell response. Along those lines, multiple studies have revealed causal links affecting cell-to-cell variability in case of apoptosis,^{133–135} induced pluripotency,¹³⁶ differentiation of stem cells,^{137,138} cancer cell heterogeneity,^{139–141} viral infection,^{142, 143} endocytosis¹⁴³ as well as nuclear factor- κ B (NF- κ B) signalling,¹⁴⁴ yeast pheromone response^{145, 146} etc. The variations in phenotypes and activity of single-cells have been found to originate (at least in part) from *e.g.* differences in cell size, growth rate, metabolic state of the cell, cell ancestry, nutrient availability, cell micro-environment (*e.g.* substrate rigidity or spatial confinement) and population context of individual cells including cell-cell contacts, local cell density, amount of free space per cell or relative location within group of growing cells. All those factors, that are often present in *in vitro* studies, might result in complex and heterogenic multicellular behaviour presented normally in natural environments of cell colony or multicellular organism. Examples could be found in the

mechanisms of quorum sensing in bacterial colonies^{147–149} or, in case of eukaryotes, in subpopulations of cancer cells presenting different proclivity for viral infection and endocytic activity within clonal cell colonies.¹⁴³ Importantly, discussed effects might not be efficiently deduced using methods based on population averaged measurements. In particular, sparse or otherwise poorly-identified subpopulations might be lost during analysis. For instance, the rare subpopulations of slow-growing "persister cells", that are less susceptible for Ampicilin treatment and enable the colony survival under stress conditions, have been identified in clonal populations of *E.coli*.¹⁵⁰

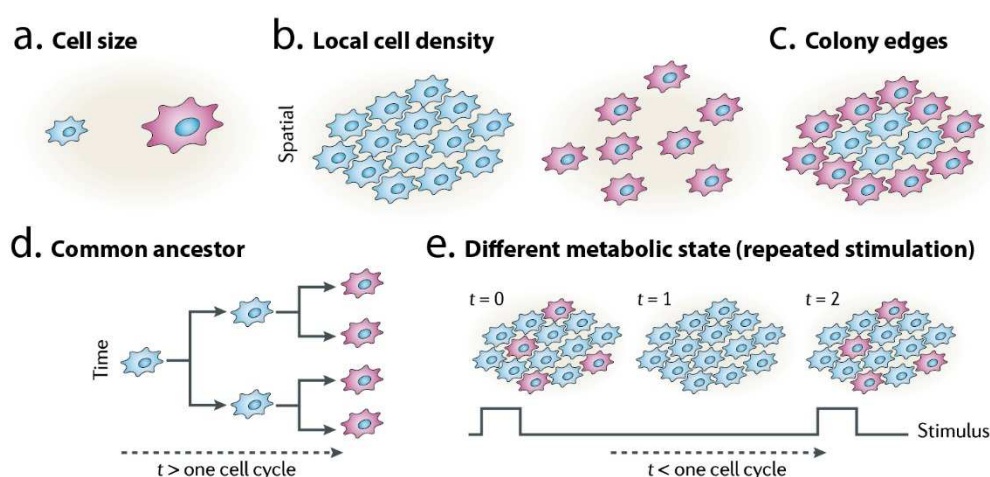


Fig.1.6. Examples of possible deterministic influence sources on cell-to-cell variability

The triggered or increased cell activity in given investigated aspect (red cells) can be triggered by several trackable factors such as: (a) differences in cell size, (b) local cell density, (c) the position within cell colony related to e.g. number of cell-cell contacts, (d) common ancestry of given cell subpopulation or (e) differences in other metabolic factors that can be tracked by e.g. repeated cell stimulation. Adapted with permission from Snijder et al.¹⁵¹ Copyright (2011) Springer Nature.

The non-genetic variability within cell populations might have a significant impact on the outcome of pharmacological treatment of complex diseases. For instance, the drug treatment of cancer cells resulted in highly variable phenotypic responses, giving hints how non-genetic variability may contribute to drug resistance in tumours.¹⁵² Moreover, the protein expression profiles and proliferation rates within solid tumours seem to be specific to the factors such cell density and location within the tumour mass.¹⁴¹ The drug-resistant states may also occur transiently as an effect of reversible epigenetic changes.¹⁵³ The cell-to-cell fluctuations in proteome make-up, either stochastic or deterministic in nature, are likely to significantly affect drug responsiveness in cells and may need to be accounted in designing the future treatment strategies.^{134, 154} Although, the measurement techniques used

in the diagnostics are facing genuine practical challenges in resolving the population heterogeneities,¹⁵⁵ stressing the need for novel analytical approaches.

1.6. Time-lapse microscopy as a tool to investigate single-cell behaviour.

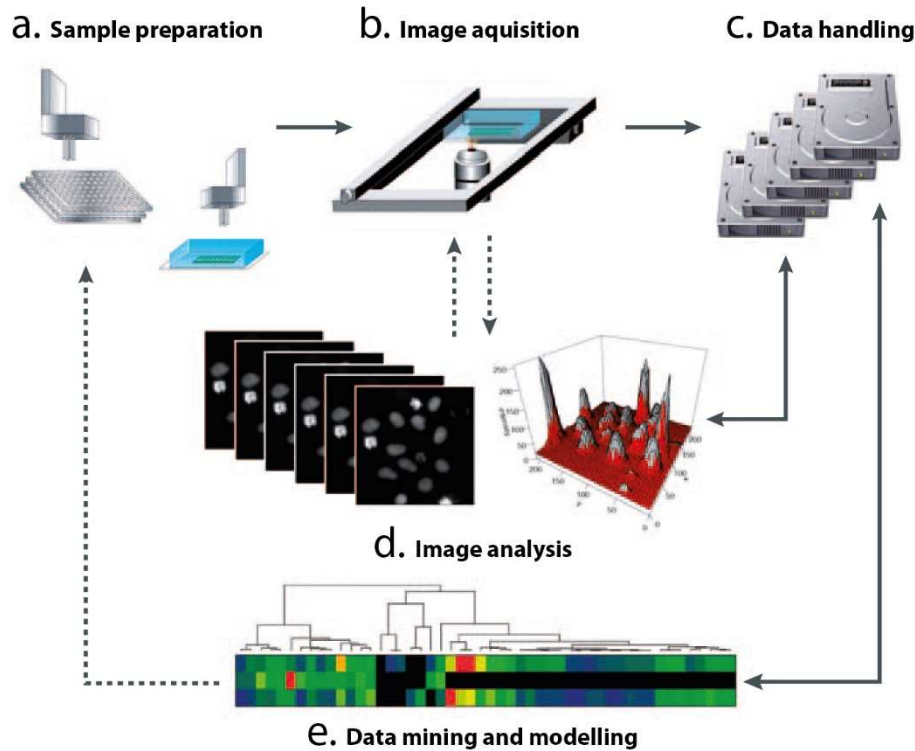


Fig.1.7. Generic pipeline of quantitative time-lapse fluorescence microscopy experiment

a) The sample handling is mostly done prior the imaging. It includes the cell treatment with chemicals, transfection, fluorescent labelling with low-molecular-weight dyes or fluorescent antibodies etc. and, in case of high-throughput methods, is often done using pipetting robots on micro-array. b) The image acquisition is performed using automated microscopes. The imaging might be done using various techniques e.g. epifluorescence, total internal reflection fluorescence (TIRF), confocal microscopy etc. c) The imaging data usually can exceed several gigabytes and require efficient software and hardware solutions, d) To acquire a single-cell information at the population-wide scale the automated image analysis needs to be perform. It includes efficient and careful background correction methods, image clustering, cell shape analysis etc. and depends strongly on performed assay. Currently, this step occurs to be a bottleneck in development of real time methods as it is time consuming and demands high computation power computers. e) Finally, the single-cell data can be integrated to gain the knowledge on investigated processes using data mining techniques. It allows to formulate models of the investigated system, gain the knowledge on the system dynamics and cell-to-cell variations in biological responses. The image acquisition and processing might need multiple iterations to optimize the analysis. Similarly, gained information might reflect the need of additional experiments (dashed lines). Adapted with permission from Pepperkok et al.¹⁵⁷ Copyright (2006) Springer Nature.

The microscopy-based assays to investigate the single cell behaviour are capable of providing morphological and spatial information on cells under investigation extending the analysis on their population context and phenotypic variations.^{143, 152, 156} The live-cell time-lapse assays also allows for revisiting the same individual cells over time providing the temporal resolution that outreaches the capabilities of most other methods like *e.g.* flow cytometry, plate-reader-based assays or fixed-cell microscopy assays. Time-lapse fluorescence microscopy is capable of assessing the molecular activity *in situ*, in the context of natural environment of living cells due to the extended palette of fluorescent protein reporters that when carefully incorporated within the molecular pathways, can provide quantitative information on investigated processes and their dynamics.^{157–159} The extended temporal resolution and capability to track individual cells opens the possibilities to investigate the dynamic responses of molecular networks within the single cells on the population-wide scale.^{158, 160, 161} Importantly, the kinetic single-cell response might lose its characteristic time profile as the averaging over population might obscure the kinetics of the process (*i.e.* the stepwise processes might occur as smooth continuous changes).^{160, 161} In the context of RNAi, live-cell time-lapse imaging was shown to be instrumental in performing large-scale RNAi screens¹⁶² and to study the activation and kinetics of miRNA-mediated RNAi.¹⁶³

Although, the microscopy-based methods provide high-content information on single-cell behaviour, a proper execution of those assays demands highly reproducible cell handling and labelling techniques to maintain the quality of high-throughput analysis.^{157, 164} For instance, the quantitative fluorescence readout demands precise detection methods combined with accurate image processing and analysis.^{158, 160, 165} Similarly, the cell identification and tracking or phenotype analysis requires robust and reliable image segmentation methods often combined with machine learning to access desirable results.^{166, 167} The complexity of computational post-processing can be reduced experimentally by use of single-cell arrays that simplify the spatial identification of particular cells. For instance, approaches such as microfluidic-based hydrodynamic cell isolation arrays,⁸¹ single-cell micro-well arrays¹⁶⁸ or functional micro-structured cell cultivation surfaces^{169, 170} have been successfully introduced to investigate *e.g.* the kinetics of enzyme activity in single cells,¹⁰² DNA damage,¹⁷¹ nanoparticle-induced apoptosis¹⁷² or kinetics of gene expression after mRNA transfection.¹⁶⁵ Particularly, micro-wells and surface micro-patterning also allows control particular aspects of the micro-environment of

individual cells or cell-cell interactions (e.g. surface area available for cell adhesion, volume of cell micro-environment or cell-cell contacts)^{55, 173, 174} and, potentially, more complex analysis of cellular responses in comparative studies of cells within colonies.

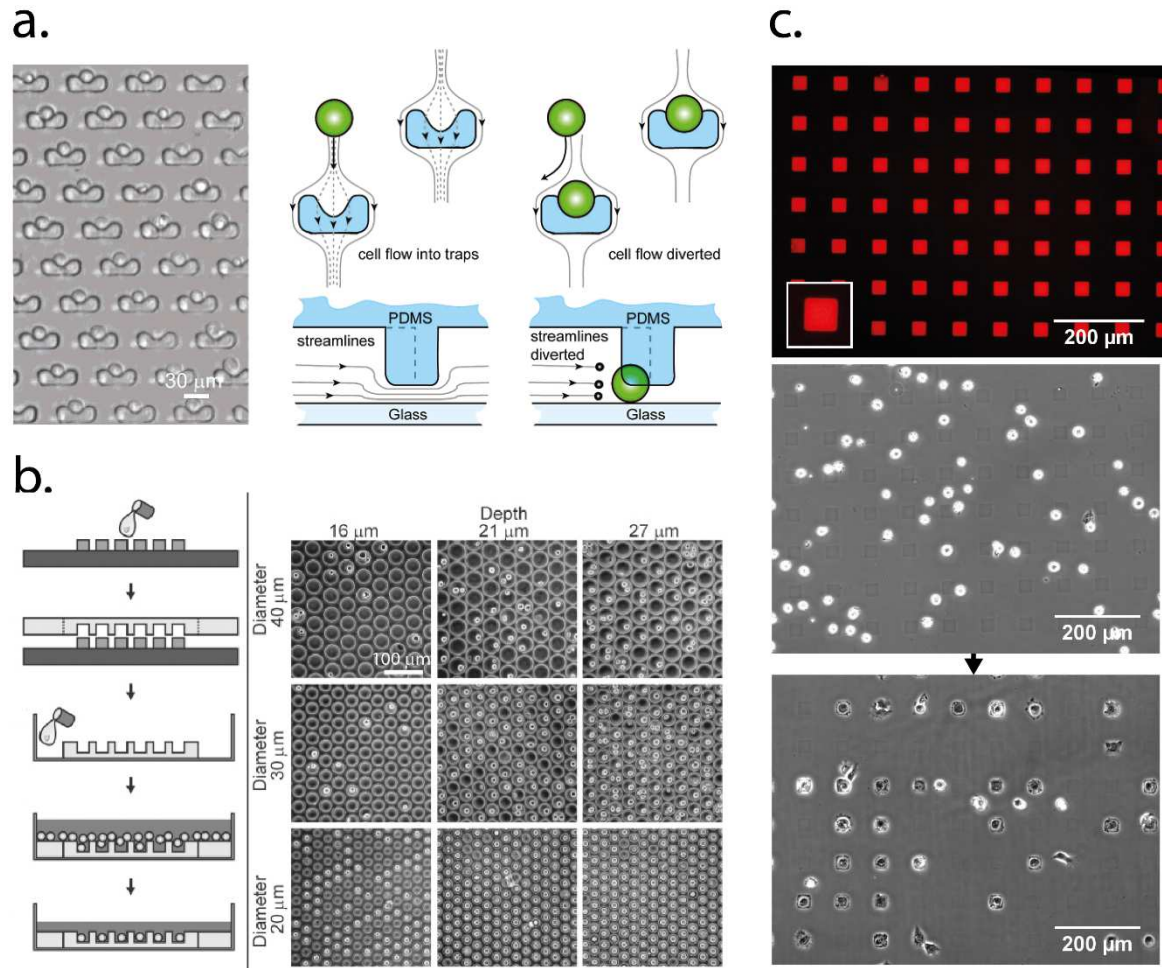


Fig.1.8. Strategies for organizing single cells into spatial arrays

a) The microfluidic chips consisting of arrays of hydrodynamic cell isolation traps (left panel) and the mechanism of cell trapping (left and middle panels). b) The PDMS-based micro-wells can be prepared by molding on the master structures (left panel). The cells occupy the position in micro-wells after seeding on structured surface and the fraction of occupied wells depends on the geometry of the wells (right panel). c) Similarly, adherent cells after seeding on micro-pattern (top panel) migrate on the PLL-PEG(2000)-passivated surfaces (middle panel) and attach onto square areas functionalized with fibronectin (top and bottom panel). By optimizing the amount of seeded cells, the high fraction of occupied adhesion sides is achieved and in the same time the double occupations minimized (bottom panel). Adapted with permission from: a) Di Carlo et al.¹⁰² Copyright (2006) American Chemical Society., b) Rettig et al.¹⁶⁸ Copyright (2005) American Chemical Society. and c) Reiser et al.¹⁷⁰ Copyright (2018) Springer Nature.

1.7. Scope of presented work

In this work, we aim at two general goals. Firstly, we develop the synthesis method for size-limited lipid-based delivery system for siRNA. In particular, we use microfluidic platform for controlled and scalable synthesis of monomolecular nucleic acid/lipid nanoparticles (mNALPs) that have been rationally designed to encapsulate a single molecule of siRNA in a highly curved, PEG-grafted, lipid bilayer. We present the benefits of the method, investigate the stability of formed nanoparticles and their biological performance in *in vitro* cell experiments. Secondly, we explore the utility of epifluorescence microscopy based single-cell assays to resolve the kinetics of RNA interference. We utilize the method to investigate the delivery of nucleic acids into the cultured cancer cells by commercial transfection system and the single-cell-level silencing efficiency on the scale of the whole cell population. The aim of the method is to provide fast, time-independent and sensitive assay for accessing the biological activity of siRNA delivery systems.

2. Experimental methods and approaches

2.1. Microfluidic chip devices

Two microfluidic chip devices were designed for the purpose of mNALP synthesis and conversion of fluorescence intensities to the number of expressed fluorescent proteins in single-cell time-lapse experiments. The details on microfluidic chip manufacture are given in protocols section.

2.1.1. Hydrodynamic focusing micro-mixing chip device

The chip design is based on previously published geometries.^{66,176} In general, the design consists of one main channel and two side channels meeting in the junction point in the 45° angle in respect to the direction of the main channel. Here the central 50% (v/v) isopropanol/water stream is clutched by two water side streams flowing from the side channels to the narrow jet. Due to the low Reynolds number regime the flow in the junction point and outlet channel remains laminar. The microscopic width of the focused jet ensures the rapid diffusive exchange of the solvent and fast equilibration in nearly aqueous conditions (5% (v/v) isopropanol/water).

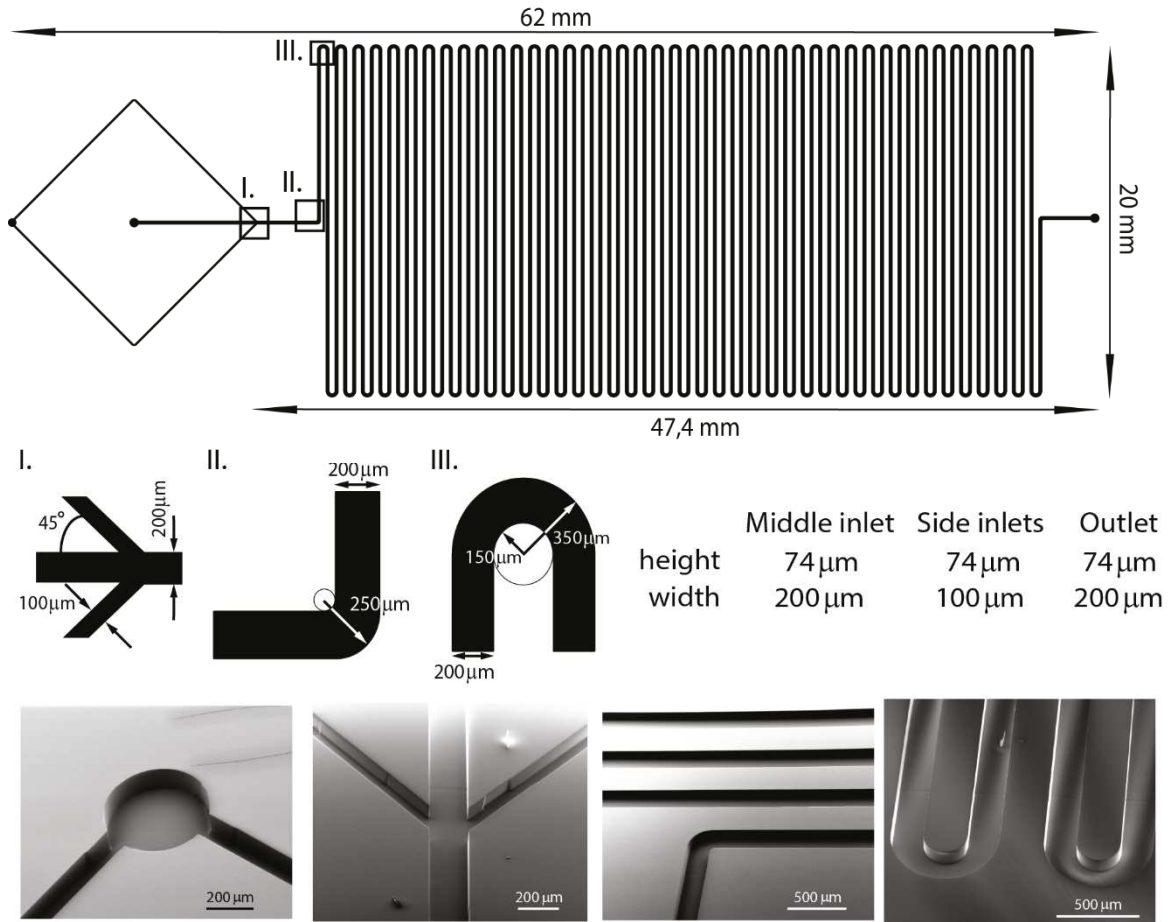


Fig.2.1. Hydrodynamic focusing chip design

The scheme of hydrodynamic focusing chip design and the scanning electron microscopy (SEM) images of PDMS micro-channels in selected chip regions. The inserts I, II and III present the details of the regions marked on the top overview image. Reprinted from Krzysztoń *et al.*¹⁷⁵

The detailed design of the micro-chip is presented on Fig.2.1. The channels have rectangular cross section with height $h = 74 \mu\text{m}$ and width $w = 200 \mu\text{m}$ or $w = 100 \mu\text{m}$ for middle and side channels respectively. During the synthesis, the total flow in the outlet channel is equal $Q = 1 \text{ ml h}^{-1}$ and the flow rate ratios between central and side flows is equal 1:9. In those conditions the mixing time can be estimated using two-dimensional model, presented by Karnik *et al.*⁶⁶ The Poiseuille flow profile in the outlet channel is described by eq.2.1.

$$u(y) = \frac{1}{8\mu} \frac{dP}{dx} (w^2 - 4y^2) \quad (\text{eq.2.1.})$$

where: w – width of the channel, μ – fluid viscosity, dP/dx – pressure gradient along the channel length, y – the lateral distance from the center of the channel. Given that the profile

is not significantly disrupted by the viscosity of isopropanol/water mixture in the central stream, the average velocity of the flow in the outlet channel can be approximated by

$$u_{f,ave} \approx u(0) = \frac{1}{8\mu} \frac{dP}{dx} W^2 \quad (\text{eq.2.2.})$$

This relation holds when:

$$\frac{w_f^2}{\mu_f} \ll \frac{W^2}{\mu} \quad (\text{eq.2.3.})$$

where the width of focused stream w_f is given by

$$W_f \approx \frac{2W}{3(1+\frac{1}{R})} \quad (\text{eq.2.4.})$$

μ_f – viscosity of focused fluid, R – flow ratio between focused and adjacent streams.

The relation eq.2.2. is satisfied for focused stream of 50% (v/v) isopropanol/water ($\mu_f \sim 3,62$ cP) by two adjacent water flows ($\mu \sim 0,9$ cP). With accordance to Fickian diffusion theory, the mixing time can be determined according to the relation:

$$\tau_{mix} \sim \frac{w_f^2}{4D} \approx \frac{W^2}{9D} \frac{1}{(1+1/R)^2} \quad (\text{eq.2.5.})$$

The 200 μm wide outlet channel in presented design results in the width of focused stream $w_f = 13$ μm and corresponding mixing time $\tau_{mix} \sim 34$ ms, assuming the isopropanol diffusivity $D \sim 10^{-9}$ $\text{m}^2 \text{s}^{-1}$ and flow rate ratio $R = 1/9$. However, this time corresponds to that taken for the change in solvent environment and does not take the dynamics of nanoparticle formation into account. To avoid possible negative effects of mass transport on particle formation, the outlet channel is extended to the length $L = 164$ cm, allowing for full diffusive equilibration of the sample inside the channel. In presented calculations we assume that the effects of particle-forming molecules dissolved in 50% (v/v) isopropanol/water in central focused stream can be neglected.

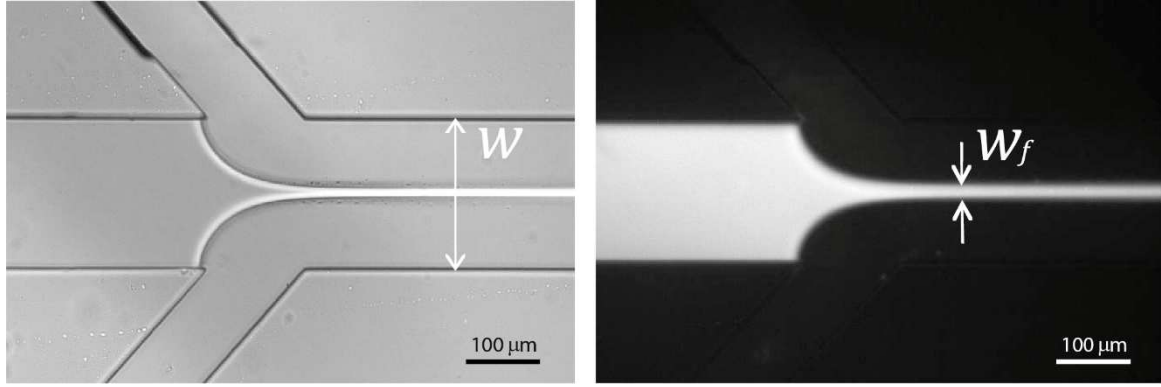


Fig.2.2. Bright-field and fluorescence images of the T-junction during mixing

The two side streams of water constrain the middle stream of 400 nM dsDNA-Cy3 and all lipid components in 50% (v/v) iso- propanol/water to a narrow jet due to low Reynolds number of the flow. Total flow 1 mL h⁻¹; flow rate ratio 1 : 9. w – outlet channel width, w_f – width of the focused stream. Adapted from Krzysztoń et al.¹⁷⁵

Furthermore, the parameters of flow in the micro-channels needs to be taken into consideration to verify the laminar flow regime. For the rectangular geometry systems described by low Reynolds numbers the relation between backpressure (ΔP) and the flow rate is given by:

$$\Delta P = R_{\Omega} Q = \frac{a\mu QL}{wh^2} \quad (\text{eq.2.6.})$$

and

$$a = \frac{12}{1-0,63\left(\frac{h}{w}\right)} \quad (\text{eq. 2.7.})$$

where: R_{Ω} – the flow resistance of the channel, L – the length of the channel, h – height of the channel, w – width of the channel, Q – flow rate through the channel. For displacement driven flow with the rate of $Q = 1 \text{ ml h}^{-1}$, flown inside the channel of height, $h = 74 \text{ }\mu\text{m}$, width, $w = 200 \text{ }\mu\text{m}$ and length, $L = 164 \text{ cm}$ (channel flow resistance $R_{\Omega} = 296,33 \cdot 10^9 \text{ kg m}^{-4} \text{ s}^{-1}$) the backpressure equals $\Delta P = 822,91 \text{ mbar}$. Calculated pressure together with given outlet channel length results in the average liquid velocity of $u_{f, ave} \approx 0.019 \text{ m s}^{-1}$ according to eq.2.2. Finally, knowing the average fluid velocity and assuming that the characteristic length scale of the system (L_h) is equal to the outlet channel with $L_h = w = 200 \text{ }\mu\text{m}$, the flow in the outlet channel corresponds to the Reynolds number $Re \approx 2$, according to the equation eq.1.1. The effects of different viscosity and density between 50% v/v isopropanol/water mixture and pure water ($\mu \sim 0.9 \text{ cP}$, $\rho = 1 \text{ g cm}^{-3}$) are considered negligible.

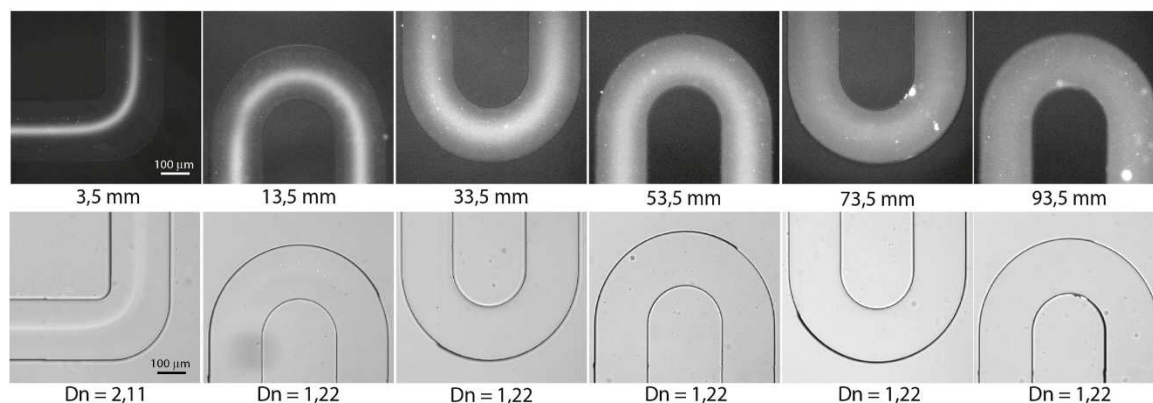


Fig.2.3. Bright-field and fluorescence images of first 6 turns of meandering outlet channel

Two adjacent water streams squeeze the middle stream of $1 \mu\text{M}$ Cy3 in 50 % (v/v) isopropanol/water into a narrow jet seen at the most left images (Total flow 1 mL h^{-1} ; flow rate ratio 1:9). The numbers on the bottom of images represent the downstream distances from the T-junction and the Dean numbers for given flow rate and channel geometry. The cross sectional flow profiles in curved regions of the channel are not disrupted by the inertia effects. Reprinted from Krzysztoń *et al.*¹⁷⁵.

Additionally, for curved channel the centrifugal inertia effects need to be taken into account. The relative contribution of centrifugal forces in relation to viscous forces for curved geometries is described by Dean number (Dn).

$$Dn = \sqrt{\frac{d}{2r}} Re \quad (\text{eq.2.7.})$$

where: r – the channel curvature radius, d – the hydraulic diameter of the channel. For rectangular channel cross section d is given by:

$$d = \frac{2hw}{h+w} \quad (\text{eq.2.8.})$$

In described geometry the first and last half turns ($r = 50 \mu\text{m}$, $d = 108 \mu\text{m}$) results in Dean numbers, $Dn = 2,11$. The full turns ($r = 150 \mu\text{m}$, $d = 108 \mu\text{m}$) results in $Dn = 1,22$.

In conclusion, we have presented that the mixing within the microfluidic chip occurs solely due to diffusion and the flow is free from chaotic turbulences that might contribute to uncontrolled formation of undesired clusters during particle synthesis. The statement holds, since the Reynolds number inside the outlet channel remains significantly below the critical values of transition (~ 1000) and turbulent flow regime (~ 2000) for selected flow rate.¹⁷⁷ Also the Dean number in the curved parts of the channel remains below the critical value for first-order Dean vortex flow (~ 36).¹⁷⁸ The values of the Reynolds and Dean numbers, suggest that the flow remains purely laminar. Observation of the flow in the

junction position (Fig.2.2.) and up to ~90 mm downstream in the outlet channel (Fig.2.3.) promotes this finding as no signs of instabilities and other disruptions in laminar flow profile due to presence of alcohol and channel curvatures is seen.

2.1.2. Microfluidic chip device for calibrating fluorescence intensities

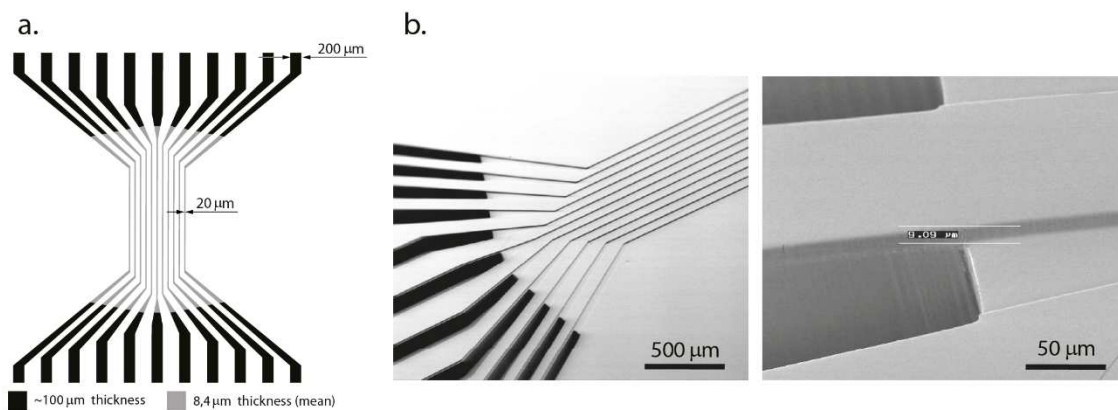


Fig.2.4. Fluorescence calibration chip design

a) The scheme of fluorescence calibration chip design. Black and grey areas represent the SU8 thickness of ~100 μm and ~8,4 μm respectively. Domains of different thickness were exposed in two separate exposition cycles and aligned using LPKF ProtoLaser LDI stage options. b) SEM images of PDMS micro-channels in central chip region.

The chip is constructed of 11 parallel and non-connected micro-channels narrowing down in the middle of the chip structure (Fig.2.4.). The channel reaches the size (20 μm width and ~8 μm height, determined using Scanning Electron Microscopy (SEM)) with the cross section comparable with the cross section of the cell. The channels were filled with the solution of the fluorescent proteins of varying concentrations and used in the conversion procedure between fluorescence intensities determined from image analysis and the numbers of expressed proteins per cell in single-cell microscopy experiments. The details are described in protocols section.

2.2. Fluorescence Correlation Spectroscopy (FCS) and confocal microscopy

The Fluorescence Correlation Spectroscopy (FCS) is an experimental technique based on analysis of fluorescence intensity fluctuations detected from diffraction-limited volume of a liquid sample. The fluctuations originate from temporal variations in number and brightness of fluorescent entities in the detection volume. Those variations may result from multiple physical and chemical processes *e.g.* as an effect of transport (diffusion, flow, active transport), photophysical processes, chemical and photochemical reactions. The

method became the wide-spread biochemistry method to investigate *e.g.* molecular interactions, protein binding, aggregation *etc.* and is also used in high-throughput screens for drug discovery.

2.2.1. Basic theoretical background

The information on investigated processes (*e.g.* diffusion kinetics) can be accessed through the analysis the fluorescence intensity fluctuations $F(t) = \langle F \rangle + \delta F(t)$ in the domain of time.¹⁷⁹ The important assumption made in presented analytical approach is that the sample is in thermodynamic equilibrium and the ergodic principle holds for the system under investigation.

The information on the processes causing the observed fluorescence intensity fluctuation can be gained through the analysis of the self-similarities of the signal and its delayed copy. The analysis of repeated patterns of such kind can be conveniently done using the correlation functions.^{180,181} The expression describing second order correlation function is given by:

$$g_{ij}^{(2)}(\tau) = \frac{\langle F_i(t)F_j(t+\tau) \rangle}{\langle F_i \rangle \langle F_j \rangle}, \quad \tau \geq 0, \quad (\text{eq. 2.9.})$$

where: $F_{i,j}$ – the functions undergoing correlation (*i.e.* fluorescence intensities detected), τ – the delay time (correlation time). The angular brackets denote the ensemble average that under the assumption of ergodicity is replaced by time average. If both F_i and F_j represent the same signal recorded by one detector the relation eq. 2.9. is referred as autocorrelation function (ACF). Autocorrelation functions can be considered the measure of mentioned self-similarities between the signal and its delayed copy as a function of the delay time.

The autocorrelation of time-dependent fluorescence intensity fluctuations is directly related to the expression eq. 2.9. and is expressed as:

$$G_{ii}(\tau) = g_{ii}^{(2)}(\tau) - 1 = \frac{\langle \delta F_i(t)\delta F_i(t+\tau) \rangle}{\langle F_i \rangle^2} \quad (\text{eq. 2.10.})$$

Since, the fluorescence excitation and emission of a single dye are uncorrelated processes, the time between those events is random. This induces incoherence between the fluorescence signals emitted by different molecules residing the detection volume. Hence, the measured fluorescence intensity detected at a particular time point from the detection volume depends only on the photophysical properties of the dye, the parameters of

detection system, the sample illumination and the concentration of the dye. The expression describing the detected intensity is given as:

$$F(t) = \int W(\mathbf{r}) qc(\mathbf{r}, t) dV \quad (\text{eq. 2.11.})$$

and:

$$W(\mathbf{r}) = \frac{S(\mathbf{r})I(\mathbf{r})}{I_0}, \quad (\text{eq. 2.12.})$$

$$I_0 = \max(I(\mathbf{r})) \quad (\text{eq. 2.13.})$$

$$q = I_0 \kappa \sigma_{exc} \varphi \quad (\text{eq. 2.14.})$$

where: $W(\mathbf{r})$ – function describing effective shape of the detection volume, q – molecular brightness of the dye, \mathbf{r} – vector describing position of volume unit within detection region, $I(\mathbf{r})$ - position dependent excitation intensity, σ_{exc} – excitation cross section of the dye, φ – fluorescence quantum yield of the dye, κ – total fluorescence detection efficiency, $S(\mathbf{r})$ – normalized fluorescence collection efficiency and $c(\mathbf{r}, t)$ – position and time dependent concentration of the dye/particle.

The ideal solution of point like particles in open volume is considered. In those conditions, the number fluctuations of particles in detection volume are described by Poisson statistics:

$$P(n, \langle N \rangle) = \frac{\langle N \rangle^n}{n!} \exp(-\langle N \rangle) \quad (\text{eq. 2.15.})$$

where $P(n, \langle N \rangle)$ is the probability to detect given number of particles n inside the detection volume at any given time point.

The assumption implies also that the fluctuation in concentration of different fluorescent entities in multiple component system are independent at every given time point:

$$\langle \delta c_i(\mathbf{r}, 0) \delta c_j(\mathbf{r}', 0) \rangle = \bar{c}_i \delta_{ij} \delta(\mathbf{r} - \mathbf{r}') \quad (\text{eq. 2.16.})$$

where: \bar{c}_i - the mean concentration of the i -th fluorescent component, δ_{ij} - the Kronecker delta and δ – Dirac delta function. The correlation function of i -th component is given by:

$$\langle \delta c_i(\mathbf{r}, t) \delta c_i(\mathbf{r}', 0) \rangle = \bar{c}_i \Phi_i(\mathbf{r}, \mathbf{r}', t) \quad (\text{eq. 2.17.})$$

and $\Phi_i(\mathbf{r}, \mathbf{r}', t)$ is the Green's function characterizing particle motion.

In described case the relation describing the single component ACF is given by:

$$G(\tau) = \frac{\iint W(\mathbf{r})\Phi(\mathbf{r},\mathbf{r}',t)W(\mathbf{r}')dVdV'}{\bar{c}(\int W(\mathbf{r})dV)^2} \quad (\text{eq. 2.18.})$$

The zero boundary value of the ACF is given by the inverse of the average effective number of particles in confocal volume:

$$G(0) = \frac{1}{\langle N \rangle} \quad (\text{eq. 2.19.})$$

and is given by:

$$\langle N \rangle = \bar{c}V_{eff} \quad (\text{eq. 2.20.})$$

where:

$$V_{eff} = \frac{(\int W(\mathbf{r})dV)^2}{\int W(\mathbf{r})^2dV} \quad (\text{eq. 2.21.})$$

is the effective detection volume. For confocal detection geometry, described below in instrumentation section, the shape of the detection volume can be successfully approximated by 3D Gaussian ellipsoid:

$$W(x, y, z) = \exp \left[-\frac{2(x^2+y^2)}{r_0^2} - \frac{2z^2}{z_0^2} \right] \quad (\text{eq. 2.22.})$$

The shape elongation of the Gaussian ellipsoid can be characterized by structure parameter:

$$f = \frac{z_0}{r_0} \quad (\text{eq. 2.23.})$$

For the given Gaussian approximation the effective number of molecules in the detection volume is given by:

$$\langle N \rangle = \pi^{3/2} r_0^2 z_0 \bar{c} \quad (\text{eq. 2.24.})$$

According to this relation the concentration of the fluorescent entities can be determined knowing the dimensions of the detection volume. What is important, the background signal, resulting from the detector dark counts or scattering background, contributes to the reduction of the amplitude of ACF. Thus, the effect needs to be taken into account while estimating the concentration of fluorescent particles:

$$G(0) = \frac{1}{\langle N \rangle} \left[1 - \frac{\langle F_B \rangle}{\langle F \rangle + \langle F_B \rangle} \right]^2 \quad (\text{eq. 2.25.})$$

where $\langle F_B \rangle$ is the mean background intensity.

Additionally, knowing the effective number of particles the molecular brightness of the fluorescent entities can be estimated using the counts per molecule per second (CPM), defined as:

$$\text{CPM} = \frac{\langle F \rangle}{\langle N \rangle} \quad (\text{eq. 2.26.})$$

2.2.2. Autocorrelation function in systems characterized by pure diffusion

In most cases of biochemical and colloidal science research FCS is used to address questions related with transport phenomena, colloidal properties of the sample *e.g.* sizes of diffusing particles or kinetic coefficients of reactions occurring in investigated systems. The fluctuations in concentration of particles in an n -component system consisting of active transport, diffusion and chemical reaction dynamics are termed by the reaction-diffusion equation:

$$\partial_t c_i(\mathbf{r}, t) = D_i \nabla^2 c_i(\mathbf{r}, t) + \sum_{j=1}^n K_{ij} c_j(\mathbf{r}, t) - \mathbf{v}_j(\mathbf{r}) \cdot \nabla c_i(\mathbf{r}, t) \quad (\text{eq. 2.27.})$$

that in the case of a system characterised by pure Fickian diffusion dynamics is reduced to:

$$\partial_t c_i(\mathbf{r}, t) = D_i \nabla^2 c_i(\mathbf{r}, t) \quad (\text{eq. 2.28.})$$

where: D_i - diffusion coefficient of i -th system component, \mathbf{v}_j - flow velocity of i -th system component, K_{ij} - the elements of kinetic rate coefficients matrix describing reaction kinetics.

The Green's function characterizing the free diffusion of the i -th component of the system in d dimensions is given by:

$$\Phi_i(\mathbf{r}, \mathbf{r}', t) = \frac{1}{(4\pi D_i t)^{d/2}} \exp\left[-\frac{(\mathbf{r}-\mathbf{r}')^2}{4D_i t}\right] \quad (\text{eq. 2.29.})$$

For the case of a one component system the ACF function is represented as:

$$G(\tau) = \frac{1}{\langle N \rangle} G_D(\tau) \quad (\text{eq. 2.30.})$$

and the normalized ACF for free normal diffusion in 3 dimensions $G_D(\tau)$ can be derived from eq. 2.18., eq. 2.22. and eq. 2.30. as:

$$G_D(\tau) = \frac{1}{(1+\tau/\tau_D)\sqrt{1+f^{-2}\tau/\tau_D}} \quad (\text{eq. 2.31.})$$

where f – the structure parameter of detection volume given in eq.2.23. and τ_D - the diffusion time being the characteristic time of the decay of fluorescence correlations given by:

$$\tau_D = \frac{r_0^2}{4D} \quad (\text{eq. 2.32})$$

The effective size of the detection volume can be determined using a standard sample of particles of known diffusion coefficient. Then the determination of the diffusion times of sample under investigation is possible.

With accordance to the kinetic theory, at the low Reynolds number regime diffusive movement of spherical particles without external potential field, the diffusion coefficient D is given by Stokes-Einstein equation:

$$D = \frac{k_B T}{6\pi\mu R_h} \quad (\text{eq. 2.33.})$$

that links the diffusion kinetics with the particle sizes through the hydrodynamic radius R_h . Here: k_B – Boltzmann constant, μ – solvent viscosity, T – temperature in Kelvins.

The case of n -component system of non-interacting particles the autocorrelation function is represented by:

$$G(\tau) = \frac{\sum_{i=1}^n q_i^2 Y_i G_{Di}(\tau)}{\langle N_{\text{tot}} \rangle (\sum_{i=1}^n q_i Y_i)^2} \quad (\text{eq. 2.34.})$$

and

$$Y_i = \frac{\bar{c}_i}{\sum_{i=1}^n \bar{c}_i} \quad (\text{eq. 2.35.})$$

$$\langle N_{\text{tot}} \rangle = V_{\text{eff}} \sum_{i=1}^n \bar{c}_i \quad (\text{eq. 2.36.})$$

where Y_i - the molar fraction of i -th component, $\langle N_{\text{tot}} \rangle$ - total effective number of particles in the detection volume, q_i - the molecular brightness of i -th component. Importantly, in this case the amplitude of correlation function is determined by apparent number of molecules in detection volume $\langle N_{\text{app}} \rangle$ -that can significantly differ from $\langle N_{\text{tot}} \rangle$.

$$\langle N_{\text{app}} \rangle = \frac{1}{G(0)} = \langle N_{\text{tot}} \rangle \frac{(\sum_{i=1}^n q_i Y_i)^2}{\sum_{i=1}^n q_i^2 Y_i} \quad (\text{eq. 2.37.})$$

2.2.3. Triplet blinking kinetics

Given the quantum nature of fluorescence emission the kinetics of photophysical processes related photon emission are generally affecting the autocorrelation functions. In particular, the intersystem crossing kinetics between electronic singlet and triplet state is generally observed. Given the prolonged kinetics of phosphorescence the molecules residing in long-lived triplet state are not emission-active and thus not detected in the detection volume. When the kinetics of the dyes entering the triplet state is taken into account the ACF of single component system have a form:

$$G(\tau) = \frac{1}{\langle N \rangle} \left[1 + \frac{T}{1-T} \exp\left(-\frac{\tau}{\tau_T}\right) \right] G_D(\tau) \quad (\text{eq. 2.38.})$$

when the multicomponent equivalent is given by:

$$G(\tau) = \frac{1}{\langle N_{\text{tot}} \rangle} \left[1 + \frac{T}{1-T} \exp\left(-\frac{\tau}{\tau_T}\right) \right] \frac{\sum_{i=1}^n q_i^2 Y_i G_{Di}(\tau)}{(\sum_{i=1}^n q_i Y_i)^2} \quad (\text{eq. 2.39.})$$

where: T – the fraction of molecules present in detection volume that entered the triplet state and τ_T – the triplet blinking time.

For practical reasons the expression describing two component diffusion kinetics with triplet state used during evaluation of experimental data had form:

$$G(\tau) = A_0 + \frac{1}{n(F+\alpha(1-F))} \left[1 + \frac{T}{1-T} \exp\left(-\frac{\tau}{\tau_T}\right) \right] \left[\frac{1}{(1+\tau/\tau_1)} \frac{1}{\sqrt{1+\tau/(f^2\tau_1)}} + \alpha^2 \frac{1-F}{(1+\tau/\tau_2)} \frac{1}{\sqrt{1+\tau/(f^2\tau_2)}} \right] \quad (\text{eq. 2.40.})$$

where: A_0 - offset, $n = \langle N_{\text{tot}} \rangle = n_1 + n_2$ – effective number of particles in confocal volume, τ_1 - diffusion time of particles 1, τ_2 - diffusion time of particles 2, F – fraction of molecules of species 1 ($F = Y_1 = n_1/(n_1 + n_2)$), α – relative brightness of particles 2 in relation to particles 1 ($\alpha = q_2/q_1$).

2.2.4. FCS and Confocal microscopy instrumentation

The FCS acquisition demands the setup providing tightly focused laser beam and highly efficient collection of photons emitted from the detection volume. Commonly, the confocal microscopy setups are adopted for this purpose, where the confocal volume serves as the detection area.

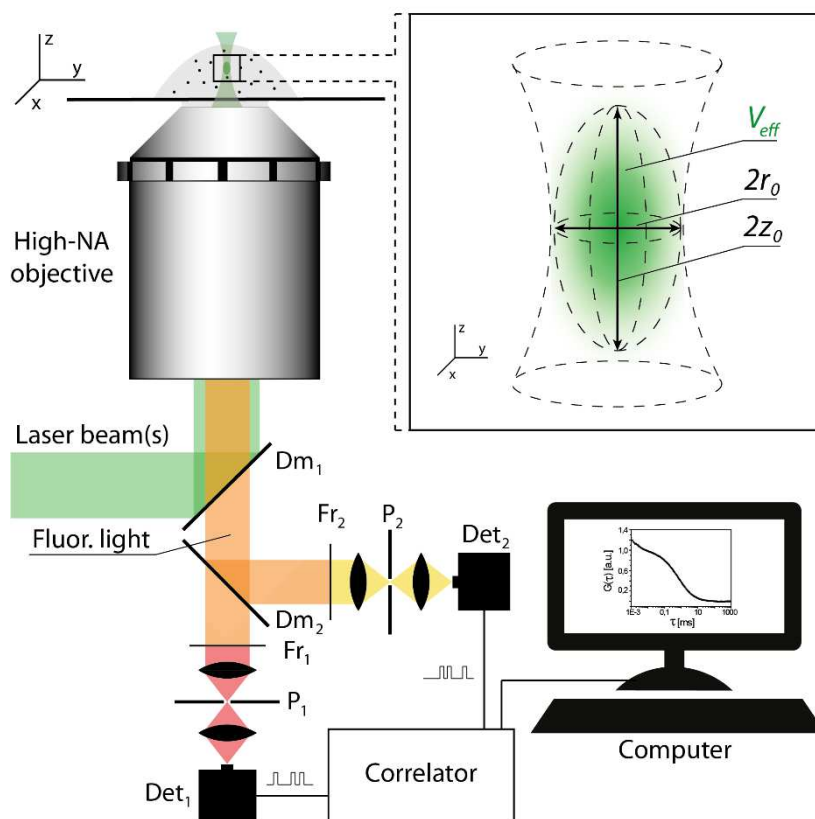


Fig.2.5. Typical confocal-microscopy-based setup for fluorescence (cross-)correlation spectroscopy

The detection and excitation happens through high-numerical-aperture, water-immersion objective. The dichroic mirrors, Dm₁ and Dm₂, 1) separate the fluorescence signal from laser excitation(s) and 2) spectrally disjoin the fluorescence signals into related detection channels, respectively. The split fluorescence light is subsequently filtered (Fr₁ and Fr₂). The detection of fluorescence signal emitted from effective detection volume (shown in the insert on the right, r_0 and z_0 represents the radiuses of short and long axes of 3D Gaussian ellipsoid) is possible due to two properly aligned pinholes (P₁ and P₂) and is done through fluorescence filters within two detectors (Det₁ and Det₂). Detected signal is correlated using the hardware correlator and processed data are stored.

In presented work, we use the Zeiss LSM 510 ConfoCor2 experimental system equipped with a C-Apochromat 40x/1,2 high-numerical-aperture, water-immersion objective. Objective is capable of refractive index correction important during measurements in 50% v/v isopropanol/water solutions. We have done the measurements using 543 nm HeNe or 488 nm argon laser excitation and BP 560–615 nm or BP 500–530 nm emission filters for Cy3/CayRFP and ATTO488/eGFP respectively. Measured fluorescence signals are correlated using hardware correlator. Samples are measured in 8-well LabTek II chamber slides (170 μm bottom glass thickness, Nunc, Thermo Scientific). The detection volume calibration is performed using Rhodamine 6G, Alexa 546 and Alexa488.^{182,183} The sample temperature is controlled by equilibration to the ambient

temperature of air conditioned room (25°C). The data evaluation is done using PyCorrFit software, developed by Thomas Weidemann (Max Planck Institute of Biochemistry, Martinsried, Germany) and Paul Müller (Biotechnology Center of the TU Dresden, Germany). The schematic representation of the setup is given on the Fig.2.5.

The same optical setup in imaging working mode was used to acquire confocal images during particle binding and uptake evaluation in *in vitro* cell experiments. The temperature control was carried out using Ibidi Heating System (Ibidi GmbH). The acquisition was done using two detection channels - green: ATTO 488, 488 nm argon laser excitation, BP 500–530 nm emission; and red: LysoTracker, 545 nm HeNe laser excitation, LP 560 nm emission. Z-Stacks consisting of 11 slices at increments of 0,5 µm were obtained. Image processing was done using ImageJ software.

2.3. Flow cytometry (FC)

Flow Cytometry (FC) is a laser-based, single-cell method to investigate the cell morphology and physiology. The method has found an established position in clinical diagnostics¹⁸⁴ and biomedical research.¹⁸⁵ It is also highly accurate preparative method allowing for separation of cells of different kind, physiological state *etc.*¹⁸⁶

FC relies on analysis of fluorescence and scattered laser light emitted/scattered by the single cells passing through the laser beam. The single-cell flow is assured by using hydrodynamic focusing flow geometry, where the stream of cell suspension is squeezed inside the column of flowing sheath fluid. Due to small size of focusing junction and the outlet channel the low Reynolds number regime is sustained and the flow remains laminar. The spatial constrains on core flow causes the separation of suspended cells flowing through the outlet channel. The cell flow and the laser beam are crossing each other orthogonally in the detection point upstream from the junction. The scattered and/or fluorescence light is filtered and detected through the optical detection units in direction orthogonal to both, laser beam and flow, and in direction parallel to the laser beam (Fig.2.6.).

The angular profile of the scattered laser light holds the information on cell morphology and underlying physiological state of the cell. The angular dependence of scattered light intensity relates strongly with the sizes of scattering particles. Due to that relation, the intensity of light scattered in small angles (forward scattering) carries the information on cell sizes. The cell granularity, morphological state of the organelles *etc.*

brings a dominant contribution to the light scattered in higher angles (side scattering) as the internal cell structures are much smaller and the angular intensity profile of the light scattered from small objects is more evenly distributed than from big particles.¹⁸⁷

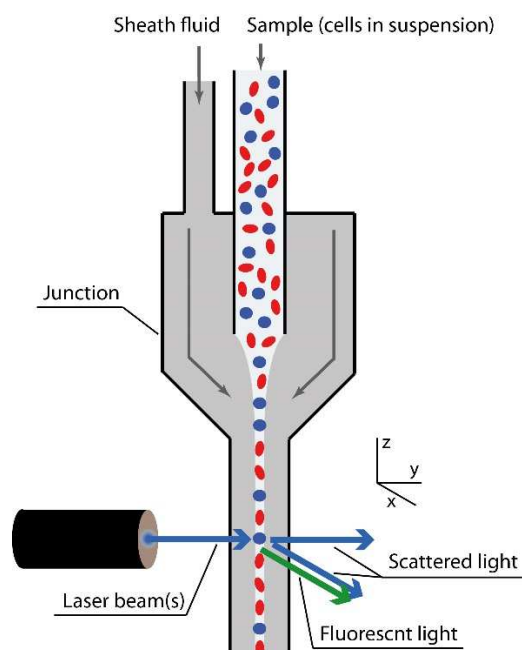


Fig.2.6. Simplified representation of the flow cytometry setup

The sheath fluid squeezes the central flow of cell suspension into a narrow stream, causing single-cells to pass the orthogonal laser beam, one cell at a time. Side and forward scattered light are detected in a direction orthogonal to each other and to the cell stream. Fluorescence signal is detected in the direction parallel to side scattered light.

More specific information on cell state can be accessed using fluorescent reporter proteins, that when efficiently designed, give quantitative and qualitative information on molecular processes within the cell, gene expression *etc.*^{188–190} Similarly, the fluorescent biomarkers activated or accumulated inside cells presenting particular metabolic state or activity *e.g.* apoptosis^{191,192} or increased or decreased mitochondrial activity,¹⁹³ can be used. Commonly, fluorescent antibodies are used also to access the expression of cell membrane proteins or binding affinities.^{194, 195}

The cell identification and quantitative assessment of cellular activity can be done using analysis of fluorescence and scatter light intensities or correlation analysis of those parameters. The different cell types or cells presenting different metabolic state most show characteristic patterns of scattered values allowing for precise identification and quantitative analysis. Additionally, acquired information can be used for real-time

differentiation between cells and subsequent automatic sorting of live cells using sorting units.

2.3.1. Flow cytometry instrumentation

In presented work, we use the flow cytometry to quantify the specific binding and uptake of folate-functionalized mNALPs. The CyFlow Space flow cytometer (Sysmex Partec GmbH, Görlitz, Germany) was used. The scattered 488 laser light was detected in directions orthogonal and parallel to the laser beam using BP 488/10 filters. The fluorescent light of ATTO488-labelled mNALPs bounded/up-taken by cells was detected in direction orthogonal to the laser beam using BP 536/40 filter. The cell counts were gated basing on forward *vs.* side scatter intensity correlation plots and equal number of cells are analyzed for each sample. The detailed description of binding/uptake experiment protocol and cell handling is given in protocols section.

2.4. Live – cell Imaging of Single-Cell Arrays (LISCA)

The combination of micro-patterned surfaces with live-cell time-lapse epifluorescence microscopy provides a versatile platform (Live-cell Imaging of Single-Cell Arrays; LISCA), that enables fast and robust quantitative readout of single-cell fluorescence intensities from spatially organized cells and cell-specific changes in those intensities in time (Fig.2.7.). In particular, the method has presented its utility in single-cell kinetic analysis of molecular processes underlying gene expression^{165,170} and correlations of cellular events related with apoptosis¹⁷² on the population-wide scale. The method relies on precise image processing, mathematical modelling and analysis of numerical data. We obtain the single-cell fluorescence intensities from image time series of cells separated on a structured cultivation surface. Single-cell fluorescence intensity time-courses can be converted into the number of fluorescent proteins expressed per cell and fitted using analytical formulas derived from a model of expression. Fitting results in distributions of kinetic parameters of molecular processes related with gene expression given in absolute values.

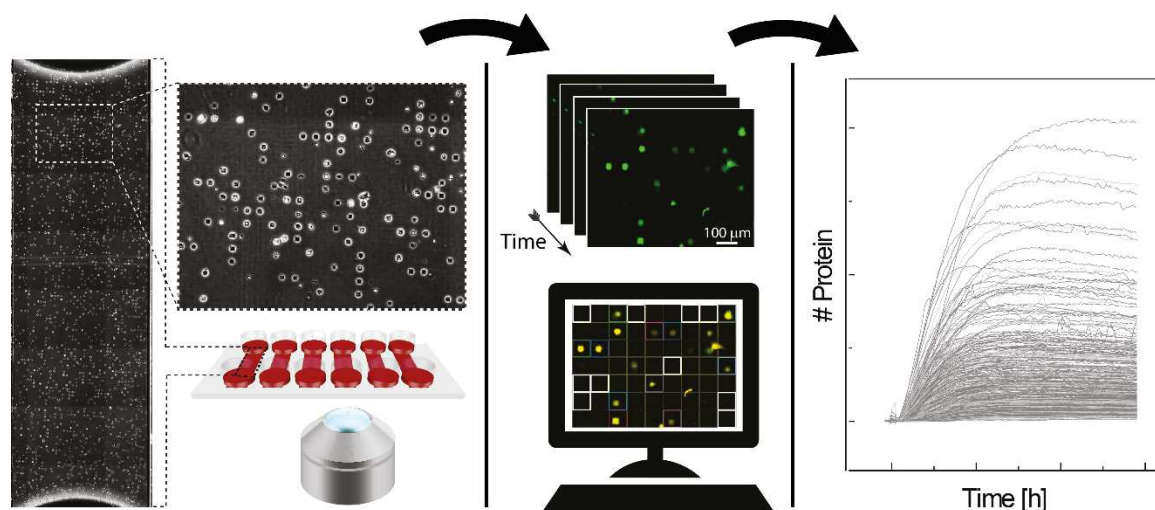


Fig.2.7. Experimental workflow of live-cell imaging of single-cell arrays (LISCA)

The cells seeded on micro-patterned cultivation surfaces occupy the arrayed adhesion sides, one cell per side. The temporal changes in fluorescence signals of each cell are detected during time-lapse imaging. Acquired images are firstly corrected for the background signal and then processed using customized ImageJ plugin. The spatial separation of cells on the micro-patterns facilitates the single-cell readout of fluorescence intensities. Yielded numerical data can be further analysed using mathematical modelling.

2.4.1. Micro-patterned surfaces for cell cultivation

The surface micro-patterns provide spatial confinement of the cell and significantly reduce the experimental noise related to cell movement during the time of experiment.^{170,196} The pattern consists of $30 \times 30 \mu\text{m}$ squared adhesion sites arrayed in square 2D lattice ($90 \mu\text{m}$ lattice distance) and is prepared by plasma-induced micro-patterning technique (preparation procedure is schematically presented in Fig.2.8). Fibronectin-coated adhesion sides are embedded in cell-repellent surface functionalized with PLL(20k)-g(3,5)-PEG(2k). Cells seeded on the micro-pattern migrate on the polymer-functionalized surface and upon encountering one of the adhesion sides, they attach and spread on the fibronectin-coated area (Fig.2.7). Due to the adjusted seeding concentration, on average only one cell occupies each adhesion side. Details regarding micro-pattern preparation are given in protocols section.

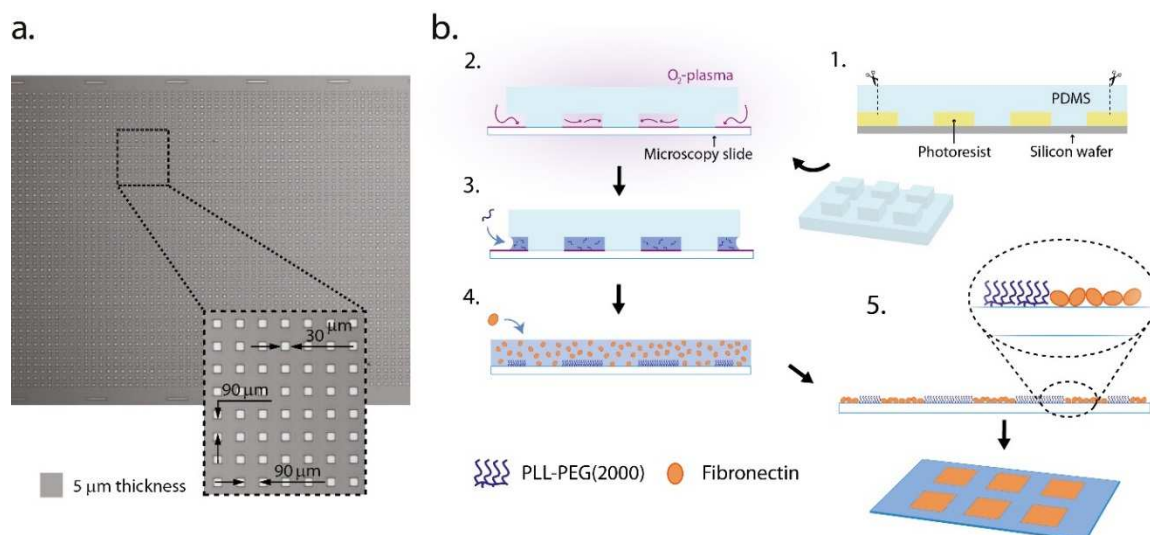


Fig.2.8. Micro-pattern production – master structure and workflow

a) The image of master structure used to prepare the micro-patterns. The insert presents the close-up of selected area of the pattern, dimensions of the grid and side length of square elementary grid unit. b) The schematic representation of steps of micro-pattern preparation. (1) The cured PDMS stamp is cut out from top of master structure and then brought into direct contact with the microscopy slide. (2) The slide surface that is unprotected by the stamp are exposed to oxygen plasma. (3) The plasma-exposed areas are passivated by exposing them to PLL(20k)-g(3,5)-PEG(2k) solution. (4) The remaining, square areas are rendered cell-adherent by incubating them with fibronectin solution that results in (5) protein absorption on non-passivated surfaces.

2.4.2. Time-lapse microscopy instrumentation

The time-lapse imaging was performed using inverted Nikon Ti-Eclipse epifluorescence microscope equipped with CFI Plan Fluor DL 10X objective, Andor Clara-E camera, and Lumencor SOLA LED lamp and motorized stage. The excitation and detection of eGFP and CayRFP fluorescence was done using BP 450-490/BP 500-550 and BP 530-560/ BP 590-650 filter sets respectively. Images were collected every 15 min within 30h – long experiments at multiple selected positions of the microscopy slide. During experiments cells were incubated at 37 °C. The temperature control was done using Ibidi heating system (Ibidi GmbH).

2.4.3. Fluorescence background correction algorithm and image analysis

To reduce the influence of background signal on the quality of quantified cell fluorescence intensity a background correction was performed. The procedure is based on the algorithm described by Schwarzfischer et al.¹⁹⁷ The method is based on statistical analysis of acquired images, identification of background-related fragments of the image,

intensity interpolation to remaining cell-related regions and subsequent subtraction of created background matrix from original image.

Firstly, the cell-related regions are identified based on statistical analysis of pixel greyscale values and clustering. In detail, the acquired 16-bit TIFF greyscale images are divided into non-overlapping, square, 16x16 pixels segments. Four statistical moments (mean, variance, skewness and kurtosis) of pixel intensity values are determined for each of segments and scattered on the four-dimensional space defined by statistical moments. The cell-related segments are identified using DBSCAN clustering algorithm (Density-Based Spatial Clustering of Applications with Noise) using statistical data from the segments.¹⁹⁸ Two parameters of the algorithm are predefined. The minimum number of cluster core point “neighbours” is defined by rounded logarithm of the number of image segments and maximum distance between two “neighbour points” is defined by half the four-dimensional interquartile range. Since the segments of a background have features that are the most similar to each other the algorithm calibrated as described before finds one cluster cloud associated with the segments of background. All other segments not assigned to this cluster is defined as cell-containing pixels.

Secondly, the intensity of background fluorescence is interpolated into the cell-related segments. The mean intensity of each cell-associated segment is calculated as mean of segment intensities within its square-shaped surrounding in iterative manner. Interpolated intensities are added to the pool of background-defining segments and accounted for in further steps. The size of the surrounding is defined by the side length of the square (e) given in number of segments per side:

$$e = 2 * \text{round}(2,5 * \sqrt{n_{seg_cell}/\pi}) + 1 \quad (\text{eq. 2.41.})$$

where: n_{seg_cell} - the number of segments that belong to given cell region. If the square-shaped surrounding has less than e^2 background segments defined (*e.g.* due to other cell with undefined yet background in the near proximity), the segment under evaluation is skipped and re-evaluated in following iterations. The iteration is held until the background has been interpolated for the whole image.

Finally, the mean greyscale values of each segment comprising the completed background are subtracted from pixel values of the original image. Pixel intensities are restricted to non-negative greyscale values.

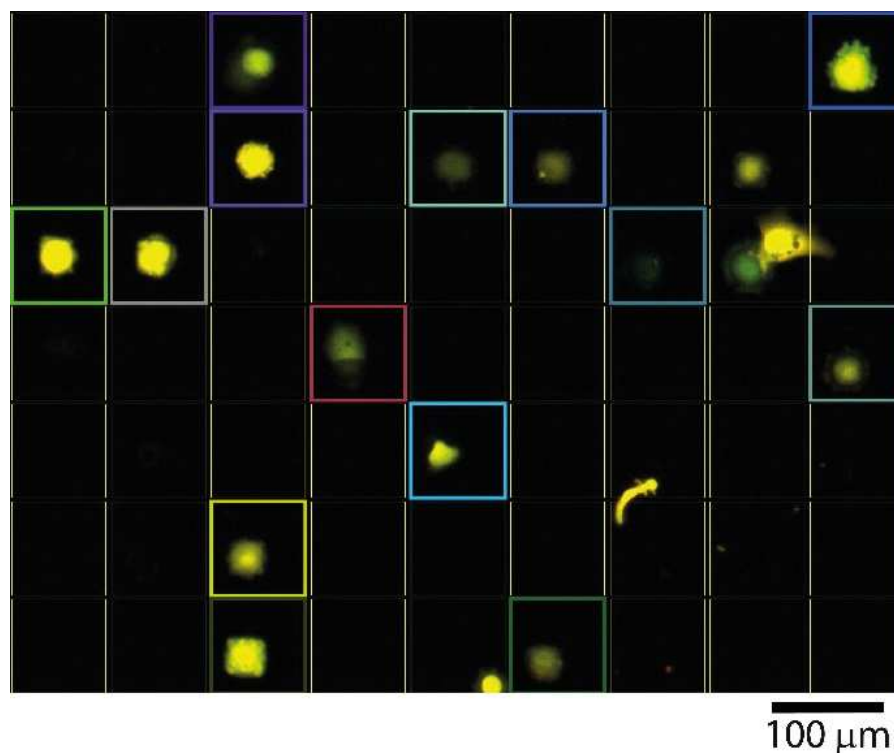


Fig.2.9. ImageJ plugin used for quantitative image analysis

ImageJ plugin used for quantitative image analysis facilitates quick readout of single-cell fluorescence intensities. The grid of square regions of interest (ROIs) is predefined in a way that it matches the spacing of micro-pattern (thin yellow lines). The ROIs associated with single cells are selected manually (thick coloured lines) and the mean pixel intensity is calculated from each of them.

The background-corrected images were used to form stacks of time-resolved images from each imaged position within the microscopy slide. The mean fluorescence intensities were determined as mean greyscale value of pixels within each cell-containing, square ROI (Fig.2.9.). The grid of defined sized ROIs was generated using an in-house written ImageJ plugin. The grid was chosen in a way that each predefined square region is overlapping with the micro-patterned adhesion sides and the grid is fitting the spacing of the micro-pattern.

2.4.4. Fluorescence calibration to protein numbers

To obtain the absolute numbers of parameters describing protein expression kinetics the number of expressed protein per cell needs to be obtained. The conversion of measured fluorescence intensities into the number of proteins expressed in each cell requires calibration procedure. For this purpose, specially designed microfluidic chip was used (see Microfluidic chip design section). Prior to the experiment, the micro-channels were incubated with 3 mg mL^{-1} Pluronic F127 water solution at $4 \text{ }^{\circ}\text{C}$ for 24h to passivate the

channel surface. Subsequently, channels are washed with PBS pH 7,4 and filled with solutions of decreasing concentrations of fluorescent proteins - enhanced green fluorescent protein (eGFP) and and Cayenne red fluorescent protein (CayRFP). Proteins were expressed and purified according to the procedure described in protocols section. Filled channels were imaged using the exposition parameters and filters used during the time-lapse experiment (Fig.2.10. bottom row). The mean fluorescence intensities of each channel are evaluated using in-house written ImageJ plugin described in image analysis section. The average of 11 measurements in different positions inside the channels is used and the standard deviation was taken as measurement error. Measurements were corrected for the background signal measured outside the channel.

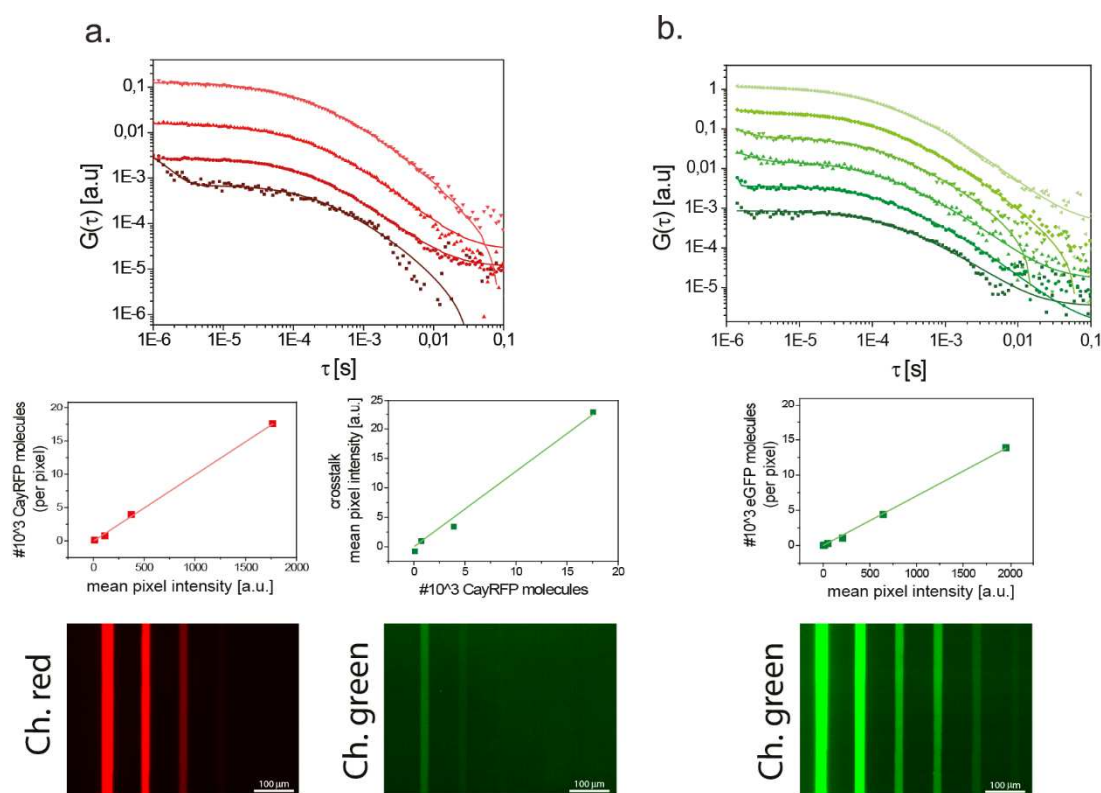


Fig.2.10. Fluorescence calibration for conversion of single-cell fluorescence intensities into the numbers of expressed proteins

Micro-channels of a height comparable with the cell thickness ($\sim 8,4 \mu\text{m}$ as determined during SEM imaging) are filled with a) eGFP or b) CayRFP solutions of varying concentrations and imaged using the same exposure parameters and filters used for time-lapse experiments (top). The fluorescence intensity was quantified as the average pixel intensity using customized ImageJ plugin. The concentration of proteins is determined using fluorescence correlation spectroscopy (bottom). The linear fit was used to calibrate the exact numbers of molecules in each cell (middle). The cross talk between red and green channel in case of CayRFP was taken into account.

The concentration of fluorescent proteins was determined using Fluorescence Correlation Spectroscopy (Fig.2.10. top row). The model accounting for single 3D diffusion component and triplet state dynamics was used (eq. 2.38.). The size of confocal volume was calibrated using Alexa 488 or Alexa 546 during the measurements of eGFP and CayRFP solutions respectively. The effective number of particles in confocal volume was determined by fitting of model function to the experimental data. The correction for detector dark counts and scattering background was performed according to eq. 2.25. Knowing the effective number of particles and the size of confocal volume the concentration of evaluated solutions was determined.

Tab.1. Fit parameters obtained during fluorescence calibration and used in fluorescence conversion into numbers of proteins.

$y = a \cdot x$	a [#10 ³ molecules]	Error a [#10 ³ molecules]	Adj. r^2
eGFP	$7,03 \cdot 10^{-3}$	$0,10 \cdot 10^{-3}$	0,9988
CayRFP	$9,95 \cdot 10^{-3}$	$0,14 \cdot 10^{-3}$	0,9992
	a [(#10 ³ molecules) ⁻¹]	Error a [(#10 ³ molecules) ⁻¹]	Adj. r^2
CayRFP (crosstalk)	1,28	0,06	0,9914

The number of fluorescent proteins per pixel was calculated knowing the channel height (~8,6 μm as determined from SEM images of the channels), the surface area per pixel (0,65 $\mu\text{m} \times 0,65 \mu\text{m}$) and the concentration of protein solutions. The calculated protein numbers per pixel were plotted against mean pixel intensity and the linear fit to the data is done using orthogonal least squares method. The obtained fit parameters were used to recalculate the mean fluorescence intensities obtained during time-lapse experiment to the number of proteins per pixel. To obtain the total number of expressed proteins calculated values were multiplied by number of pixels in cell-containing square ROIs. The cross talk between red and green channel, observed in case of CayRFP, was taken into account (Fig.2.10., middle and bottom row). The error of the determined molecule number was calculated using an error propagation, taking into account all the fitting errors and the square root of the mean pixel intensities.

2.4.5. Data processing and analysis

The single-cell mRNA expression was evaluated using three-stage gene expression model detailed in the results section. The solution of ordinary differential equations eq.2.42, eq. 2.43. and eq. 2.44.

$$\frac{\partial mRNA^G(t)}{\partial t} = -\delta * mRNA^G(t) \quad (\text{eq. 2.42.})$$

$$\frac{\partial eGFP^*(t)}{\partial t} = -\beta^G * eGFP^*(t) - k_m^G * eGFP^*(t) + k_{TL} * mRNA^G(t) \quad (\text{eq. 2.43.})$$

$$\frac{\partial eGFP(t)}{\partial t} = -\beta^G * eGFP(t) + k_m^G * eGFP^*(t) \quad (\text{eq. 2.44.})$$

related to this model, is given by the relation (eGFP example):

$$eGFP(t) = m_0^G k_{tl} \left(\frac{1}{\beta^G - \delta^G + k_m^G} e^{-(\beta^G + k_m^G)(t-t_0^G)} - \frac{1}{\beta^G - \delta^G} e^{-\beta^G(t-t_0)} - \frac{k_m^G}{(\beta^G - \delta^G)(\beta^G - \delta^G + k_m^G)} e^{-\delta^G(t-t_0^G)} \right) \quad (\text{eq. 2.45.})$$

where: $eGFP(t)$ - the number of mature eGFP molecules, t - the time, m_0^G - the number of delivered mRNA^G molecules, k_{tl} - the translation rate constant, β^G - eGFP degradation rate constant, k_m^G - eGFP maturation rate constant and δ^G - mRNA^G degradation rate constants. The analytical solution was obtained using initial conditions of $mRNA^G(0)=mRNA_0^G=m_0^G$, $eGFP^*(0)=0$ and $eGFP(0)=0$. To decrease the number of free parameters the degradation β and maturation rates k_m are determined in translation block experiments. The three-stage model is here reduced to maturation and degradation kinetics of fluorescent proteins. The solution of ordinary differential equations eq. 2.46. and eq. 2.47. describing the model

$$\frac{\partial eGFP^*(t)}{\partial t} = -\beta^G * eGFP^*(t) - k_m^G * eGFP^*(t) \quad (\text{eq. 2.46.})$$

$$\frac{\partial eGFP(t)}{\partial t} = -\beta^G * eGFP(t) + k_m^G * eGFP^*(t) \quad (\text{eq. 2.47.})$$

is given by the relation (eGFP example):

$$eGFP(t) = eGFP_0 e^{-\beta^G t} + eGFP_0^* \left(e^{-\beta^G t} - e^{-(\beta^G + k_m^G)t} \right) \quad (\text{eq. 2.48.})$$

where the number of initial mature and immature eGFP proteins during translation block is given by $eGFP_0^*$ and $eGFP_0$ respectively. Expressions given by equations eq. 2.45. and eq. 2.48. are fitted to corresponding single-cell time-courses of expressed protein numbers using the least-squares method. While evaluating the remaining parameters of mRNA expression, the protein degradation and maturation times are kept fixed at values determined during translation block experiments. The initial number of mRNA molecules

and the translation rate constant are fitted jointly as one parameter, m_0k_{it} , since they are not separately identifiable in the model. The linear fits to scattered eGFP vs. CayRFP fit parameters (m_0k_{it} , t_0 , δ) were done using the orthogonal least squares method. Initial translation rates (m_0k_{it}) and mRNA degradation constants (δ) are fitted in log-log representation. The log-normal fits to population distributions of mRNA degradation constants (δ) are done using the Levenberg–Marquardt algorithm.

3. Results

In this chapter, the results of performed experiments are presented and discussed. The content is divided in two parts where we detail firstly, the microfluidic synthesis optimization of mNALPs, their stability in biological fluids, receptor-mediated uptake and silencing activity. Second part contain the description of double-reporter assay used to investigate single-cell siRNA-mediated silencing, followed by comparison of direct analysis of fluorescence intensities and kinetic analysis of mRNA expression in terms of quantification of silencing efficiency. Finally, we analyse the correlations observed between kinetic determinants that describe expression of targeted eGFP and reference CayRFP. Furthermore, in order to determine the kinetic constants related with protein expression in an unbiased manner the additional measurements of protein maturation and degradation rate constants were needed. The results are detailed in relevant sections. In addition, we include a brief discussion on observed interdependencies between single-cell degradation rates of eGFP- and CayRFP-mRNA. Our considerations take into account differences in codon usage between coding sequences of both mRNA constructs used during the experiments.

3.1. mNALP assembly and activity

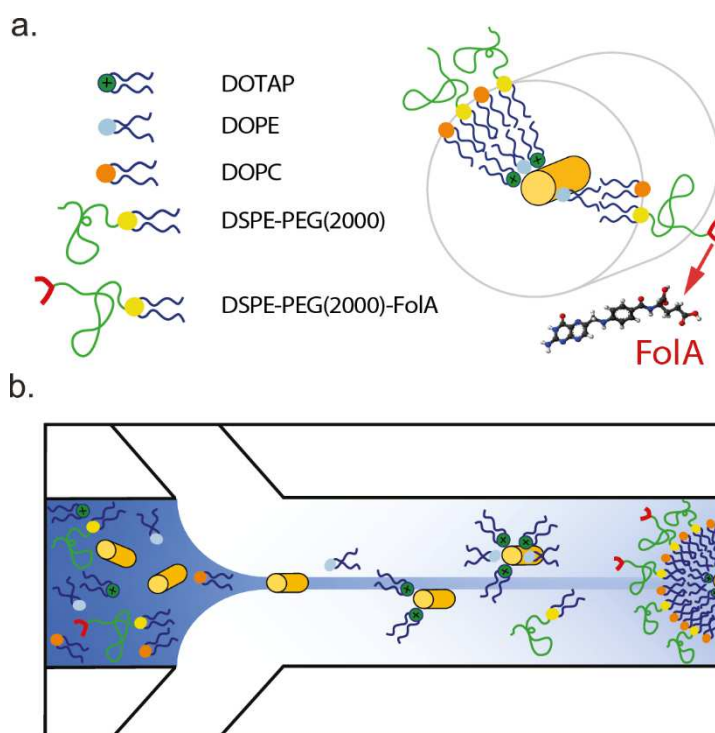


Fig.3.1. Structure and assembly of mNALPs in a hydrodynamic focussing chip device

a) The proposed structure mNALPs. The single 21 bp dsDNA/siRNA is tightly covered with highly curved, PEG-coated lipid bilayer. b) The assembly route of mNALPs in hydrodynamic focusing micro-chip. The rapid mixing at the nanoliter scale leads to changes in the solvent properties that triggers the particle formation. Adapted from Krzysztoń *et al.*¹⁷⁵

The mNALPs are composed of DOTAP, DOPE, DOPC and DSPE-PEG(2000) in the molar ratios (1:5:6:1,2). We rationally designed the lipid composition to efficiently encapsulate the single, short (~ 21 bp) double stranded oligonucleotides in a highly curved, PEG-coated lipid bilayer (Fig.3.1a.).¹⁹⁸ In previous studies it was shown that the DOTAP/DOPE/DNA systems are forming an inverted hexagonal phase when the DOTAP:DOPE molar ratios are between 1:3 and 1:5.⁴⁴ The structural unit cell of hexagonal phase comprises of a single DNA/RNA double helix tightly covered with highly curved lipid monolayer. In the rational design of mNALP structure, we chose the composition of lipids in a way that the formed DOTAP/DOPE monolayer is closed by additional outer, DOPC/DSPE-PEG(2000) monolayer. The PEG-shield causes the curvature of bilayer to be preserved and stabilizes the structure of mNALP due to the steric hindrance. It is assumed also, that the total density of DSPE-PEG(2000) accumulated on the outer layer reaches ~ 9 mol% that assures the optimal blood circulation times for comparable systems *i.e.* stealth liposomes.¹⁹⁹

As an assembly route for forming mNALPs we chose the solvent exchange. In this method, the solution of particle-forming molecules (*e.g.* lipids, polymers) is typically dissolved in a nonpolar solvent *i.e.* alcohol and then rapidly diluted in excess of nucleic-acid-containing water or buffer. The rapid change in solvent quality triggers the formation of particles. The method gives a high control on the particle nucleation and self-assembly.¹¹³ Although, the kinetics of particle formation couples with the mixing process. Thus, the additional control over mixing kinetics using microfluidics brings the modality in the particle synthesis (Fig.3.1b).^{66, 116}

Here, we investigate the size, encapsulation efficiency and homogeneity of mNALPs produced in two mixing modes - by microfluidic mixing on hydrodynamic focusing chip and by dropwise addition and vortexing. Further, in *in vitro* experiments, we test the target-specific uptake of folate-functionalized mNALPs by folate-receptor-overexpressing KB cells, their abilities to release the encapsulated nucleic acids and silencing efficiency. We also probe the unspecific interaction of mNALPs with blood serum and plasma components and their general stability in those biological fluids. To overcome the problem of increased chemical and biological instability of RNA we use the 21 bp double stranded DNA in all experiments excluding the silencing efficiency test. It was proven previously that siRNA and DNA duplexes of the same length result in mNALP samples of the same quality.¹⁹⁸

3.1.1. Evaluation of starting solvent conditions

Formation of particles is triggered by the decrease of the non-polar solvent content (isopropanol) in the solution by mixing with water. In order to minimize the diffusive distance between the particle-forming molecules we modify the standard solvent exchange protocol in a way that all of used lipids and nucleic acids are dissolved in 50% (v/v) isopropanol/water mixture prior to particle formation. Although, the increased content of isopropanol might cause the precipitation of nucleic acids from the solution due to decreased electric permittivity of the environment and the premature electrostatic interactions between positively charged DOTAP and negatively charged nucleic acids. This unwanted interaction might cause the altered self-assembly process and lead to formation of clusters or other unwanted structures.

To validate the starting conditions one need to confirm that the 50% (v/v) isopropanol content is sufficient to prevent lipids from aggregation. In the same time, the

electrostatic interactions between DOTAP and nucleic acids need to be screened sufficiently in order to prevent micro-precipitation. We assess this issue using Fluorescence Correlation spectroscopy (FCS). We perform the measurements using Cy3-labelled 21bp DNA (Cy3-dsDNA) dissolved in 50% (v/v) isopropanol/water together with all lipid components in concentrations varying within the range used during synthesis optimization. We normalize the obtained diffusion times (τ) by the value measured for naked DNA in the same solvent conditions (τ_{DNA}). No significant differences are found between the diffusion times of naked DNA and lipid/DNA mixtures in all used concentrations indicating that no precipitation or aggregation is present (Fig.3.2c.).

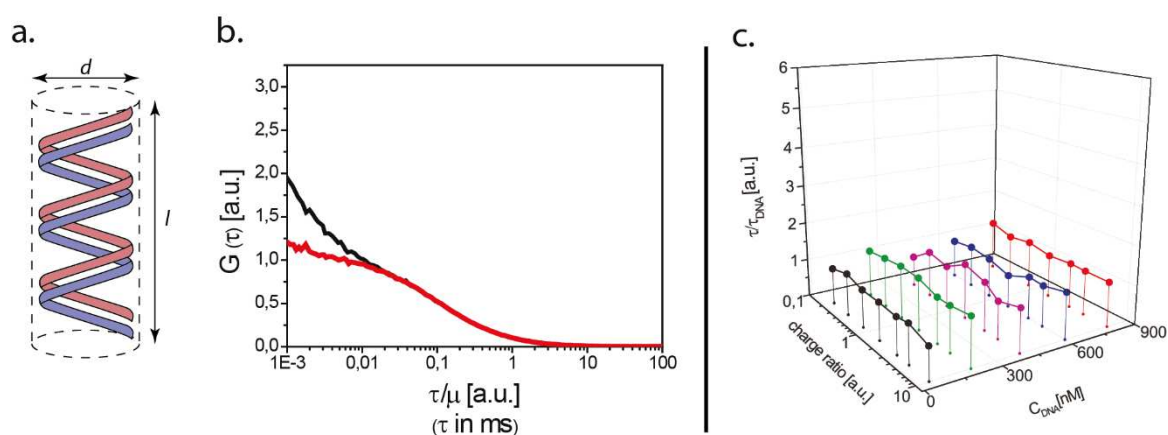


Fig.3.2. Evaluation of starting solvent conditions

a) The cylindrical model of 21 bp dsDNA. The length of the DNA and its diameter are denoted l and d respectively. b) The viscosity-normalized ACFs of naked DNA in 50 % (v/v) isopropanol/water (red) and pure water (black). The curves overlap well indicating that the viscosity changes are the dominant factor in changes in DNA diffusion times between both conditions. DNA concentration, $C_{DNA} = 50$ nM. c) The relative diffusion time of DNA in the presence of lipids (DOTAP:DOPE:DOPC:DSPE- PEG(2000) in molar ratios 1:5:6:1,2 in 50% (v/v) isopropanol/H₂O) for different total DNA concentrations. Lipid concentration is expressed as the charge ratio of the cationic DOTAP to the polyanionic DNA. No significant change in relative diffusion times is seen. Adapted from Krzysztoń et al.¹⁷⁵

Additionally, we test the influence of isopropanol on the diffusion of naked DNA. By applying the parameters of B-form of DNA double helix we calculate the diffusion coefficients of 21 bp double stranded DNA for both solvent conditions. To this end, we use the cylindrical approximation of DNA double helix (Fig.3.2a.) and the calculate related values of diffusion constants (D) using modified Stokes-Einstein equation (201):

$$D = \frac{Ak_B T}{3\pi\mu l} \quad (\text{eq. 3.1.})$$

and

$$A = \ln\left(\frac{l}{d}\right) + 0,312 + 0,565 \frac{d}{l} - 0,1 \frac{d^2}{l^2} \quad (\text{eq. 3.2.})$$

where: l – the length of the cylinder ($l = 6,8$ nm), d – the cylinder diameter ($d = 1,9$ nm), k_B – Boltzmann constant, μ – solvent viscosity (water, $\mu \sim 0,9$ cP; 50% v/v isopropanol/water, $\mu \sim 3,62$ cP), T – temperature in degrees Kelvin ($T = 298\text{K}$). We obtain the experimental values of DNA diffusion coefficients using Rhodamine 6G as a reference ($D_{R6G} = (4,14 \pm 0,05) \cdot 10^{-6} \text{ cm}^2 \text{ s}^{-1}$).¹⁸² The calculated and experimental values are in good agreement (Tab.2) indicating that no precipitation or significant changes in diffusive behaviour of DNA other than viscosity effects occur. Additionally, the viscosity normalized ACFs obtained in both solvent conditions overlap further confirming this finding (Fig.3.2b.). We calculate the apparent hydrodynamic radius (R_h^{DNA}) of free dsDNA from experimentally obtained diffusion coefficient ($R_h^{DNA} = 2,37$ nm, water). In further experiments, naked DNA serves as size reference. We calculate the hydrodynamic radii of formed nanoparticles by multiplying R_h^{DNA} by the relative diffusion times (τ_{part}/τ_{DNA}).

Tab.2. Experimental and theoretical diffusion coefficients of naked 21-bp ds DNA.

Predictions are made in accordance with the cylindrical model.

	cylindrical model predictions	experimental data
	$D_{DNA} [\text{cm}^2 \text{s}^{-1}]$	$D_{DNA} [\text{cm}^2 \text{s}^{-1}]$
Water	$9,02 \cdot 10^{-7}$	$(1,10 \pm 0,19) \cdot 10^{-6}$
50% (v/v) Isopropanol/water	$2,50 \cdot 10^{-7}$	$(2,81 \pm 0,22) \cdot 10^{-7}$

3.1.2. Influence of mixing modes and synthesis optimization

We investigate the impact of mixing mode on the quality of produced mNALP sample using FCS. In particular, we assess the sizes of produced particles, encapsulation efficiency of nucleic acids and sample homogeneity. We vary the Cy3-dsDNA (c_{DNA}) and lipid concentrations (on Fig.3.3. represented as charge ratio (ρ) between positively charged DOTAP and negatively charged Cy3-dsDNA) between 4 and 80 nM ($55 \text{ ng mL}^{-1} - 1,1 \mu\text{g mL}^{-1}$) and between 0,42 and 420 $\mu\text{g mL}^{-1}$ (charge ratio ρ ; 0,2 - 10) respectively. During

variations of lipid concentration, the DNA concentration and the molar ratios between different lipids are preserved.

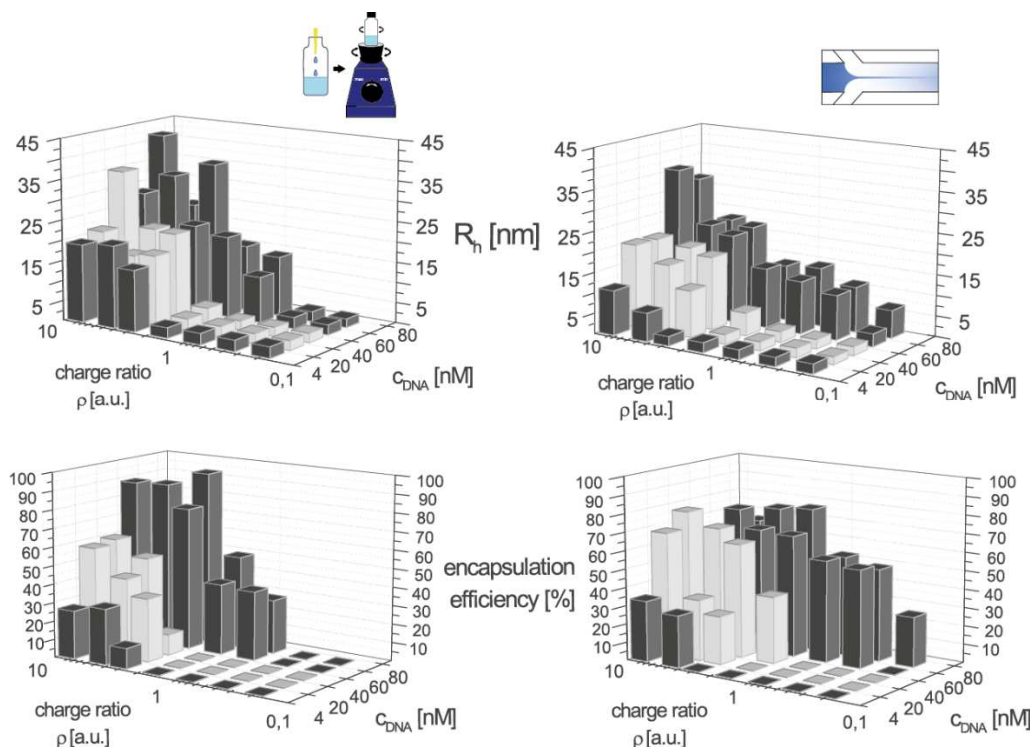


Fig.3.3. Effects of mixing mode – optimal charge ratio and DNA concentration

Influence of the DNA concentration and the charge ratio between cationic DOTAP and Cy3-dsDNA on the hydrodynamic radius of formed particles and the DNA encapsulation efficiency. The data obtained with hand-mixed (left) and microfluidic-mixed (right) samples are presented. The grey bars present trends obtained at optimal DNA concentrations (20–40 nM). Adapted from Krzysztoń et al.¹⁷⁵

We prepare the hand mixed samples by dropwise addition of lipid/DNA solutions in 50% (v/v) isopropanol/water into deionized water and vortexing. The starting solutions are diluted 10-fold leading to the final isopropanol content of approximately 5% (v/v). Similarly, we keep the flow rate ratios of 1:9 during microfluidic synthesis resulting in the same dilution factor. We evaluate the acquired autocorrelation functions (ACFs) using two-component diffusion model with triplet state dynamics (eq. 2.40.). Equivalent model with single-component diffusion is not capable of reproducing the experimental data efficiently. We use free, non-complexed Cy3-dsDNA and Rhodamine 6G¹⁸² as particle size reference and for calibration of confocal volume size, respectively. We keep fixed the diffusion time of free Cy3-dsDNA and structure parameter f (eq. 2.23.) determined from Rhodamine 6G autocorrelation function during fitting. No changes in water viscosity are detected due to residual isopropanol content.

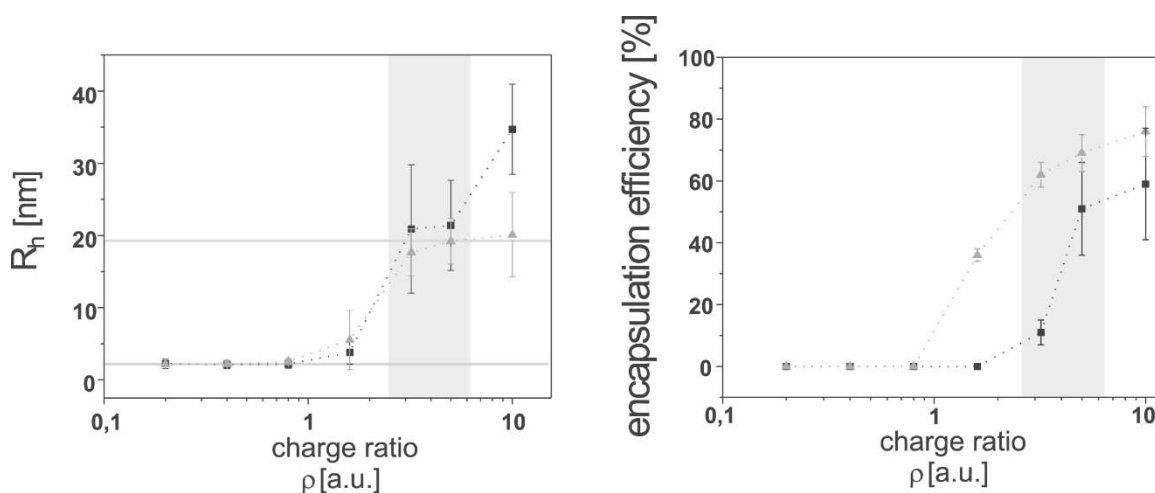


Fig.3.4. Detailed view of particle formation at optimal DNA concentration ($c_{DNA} = 40$ nM)

The hydrodynamic radius of particles and encapsulation efficiency are presented as a function of the DOTAP/Cy3-dsDNA charge ratio. Triangles (\blacktriangle) indicate the data obtained with the microfluidic mixing method, squares (\blacksquare) denote the results for vortex mixing by hand. Adapted from Krzysztoń et al.¹⁷⁵

We estimate the hydrodynamic radius (R_h) of formed particles using measured diffusion times and apparent hydrodynamic radius of free Cy3-dsDNA according to equations eq. 2.40. and eq. 2.38., respectively. Additionally, we estimate the encapsulation efficiency by fraction of diffusing complexes obtained directly from the fits. The formation of lipid/DNA complexes occur above isoelectric point ($\rho = 1$) for all Cy3-dsDNA concentrations in both mixing modes. Although, the high concentrations of Cy3-dsDNA ($c_{DNA} > 40$ nM) associates with the aggregate-related high intensity spikes present already above charge ratio $\rho = 0,4$, as seen in the time-dependent fluorescence traces (Fig.3.5.). Contrary, the low concentrations of Cy3-dsDNA ($c_{DNA} < 20$ nM) leads to low, maximal encapsulation rates of 30%. Sudden stepwise assembly of particles of 19,2 nm in radius is a result of an increasing charge ratio at the optimal Cy3-dsDNA concentrations (c_{DNA} between 20 and 40 nM).

Due to microfluidic synthesis the particle size reaches a steady level and is not exceeded even at high charge ratios (Fig.3.4.). Moreover, we observe the significant 20% increase in encapsulation efficiency when compared to samples obtained by dropwise addition and vortexing. Additionally, the microfluidic-synthesized samples presents significantly narrower size distributions that is reflected in experimental variance in measure particle size between individual measurements (represented as error bars on Fig.3.4.). Inspection of fluorescence time-traces and the ACFs obtained for samples prepared by both mixing methods are supporting those findings (Fig.3.5.). Fluorescence

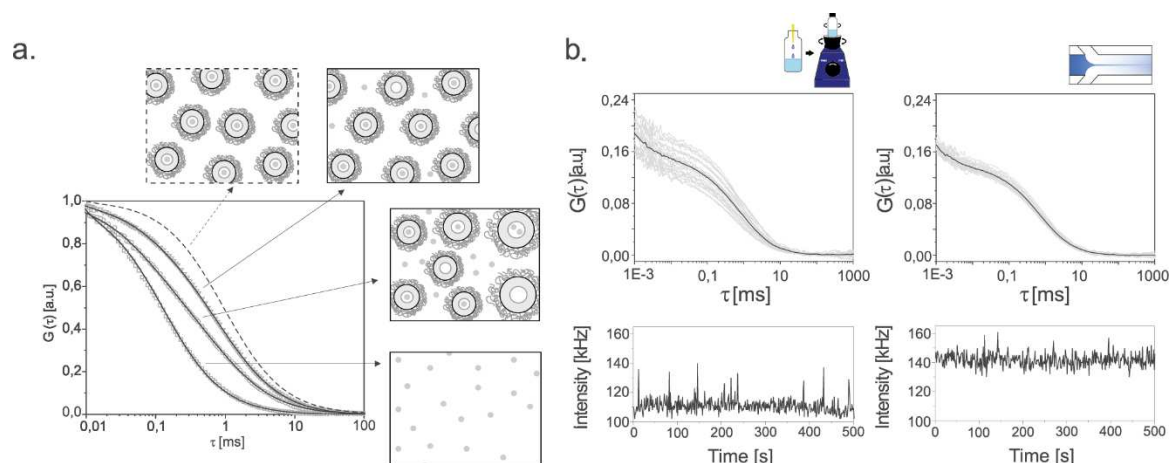


Fig.3.5. Effects of mixing mode on – encapsulation efficiency and sample homogeneity

a) The normalized ACFs of samples prepared by vortexing (\circ) and microfluidic mixing (\blacktriangledown) at optimal conditions ($c_{DNA} = 40$ nM, $\rho = 5$) and of Cy3-DNA (\square). The dashed line shows the ACF calculated for a single component mNALP system (particles with hydrodynamic radius $R_h = 19,2$ nm) representing the 100% encapsulation efficiency. The solid lines represents fits to experimental data. b) Top: The ACFs obtained by the single 15 s measurement runs of samples prepared by (I) vortex mixing by hand exhibit relatively high deviations in shape and amplitude when compared to the ones obtained for (II) microfluidic-mixed samples (average, black curve; single measurements, grey curves) Bottom: The corresponding fluorescence time-traces show frequent high-intensity sparks (I) in vortexed samples. Contrary, the time-traces obtained from microfluidic-mixed samples show sparse events of such kind. Adapted from Krzysztoń *et al.*¹⁷⁵

time-traces revealed frequent high intensity spikes indicating that large and bright aggregates are formed frequently during particle synthesis by hand mixing. Moreover, the ACFs from repeated single measurements of the same sample show decreased variation in shape and amplitude in case of microfluidic mixing when compared to vortexed samples (Fig.3.5b.). This finding reflects increase in sample homogeneity. Increase in encapsulation efficiency is further reflected in significant shift towards higher diffusion times between averaged ACFs obtained for samples prepared by both mixing modes (Fig.3.5a.). As a conclusion of presented analysis, we chose the Cy3-dsDNA concentration $c_{DNA} = 40$ nM and charge ratio $\rho = 5$ as optimal conditions of efficient mNALP synthesis.

Importantly, to achieve site-specific activity of mNALPs additional surface functionalization is required. We functionalized mNALPs by replacing 16,7% of the DSPE-PEG(2000) used in previously described lipid formulation with folate-conjugated DSPE-PEG(2000)-FolA. The presence of folate ligands in the distal end of PEG-tethered lipids did not change the assembly behaviour of formed particles (Fig.3.6.).

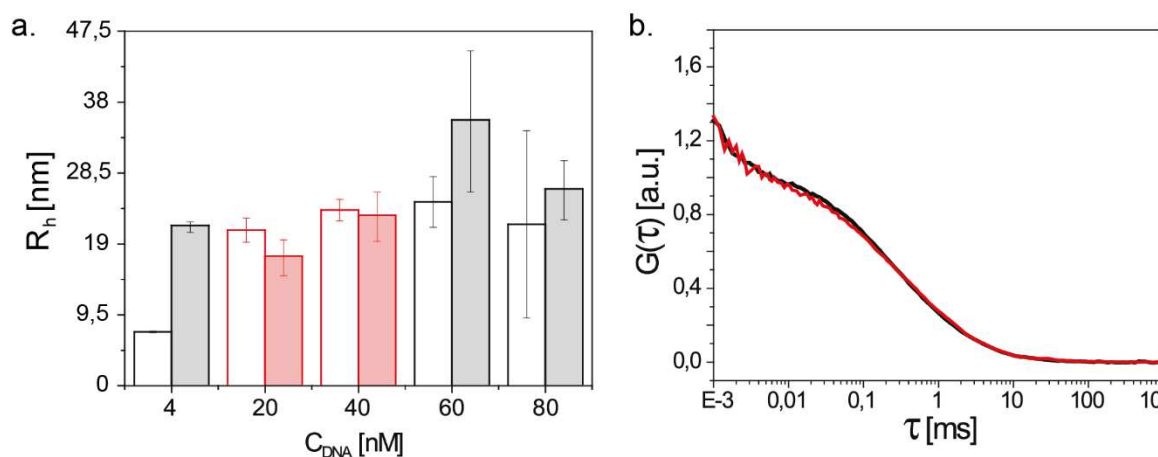


Fig.3.6. Effects of particle functionalization with Fola on mNALP formation

a) The comparison of hydrodynamic radii of Fola-functionalized (full bars) and non-functionalized mNALPs (empty bars). Particles are prepared at charge ratio $\rho = 5$ with varying Cy3-DNA concentrations. Red bars denote the optimal Cy3-DNA conditions for mNALP synthesis. b) The ACFs of Fola-functionalized and non-functionalized mNALPs prepared at optimal synthesis conditions ($C_{DNA} = 40$ nM, $\rho = 5$). The curves overlap well showing negligible deviations between each other. Adapted from Krzysztoń et al.¹⁷⁵

3.1.3. mNALP stability in blood serum and plasma

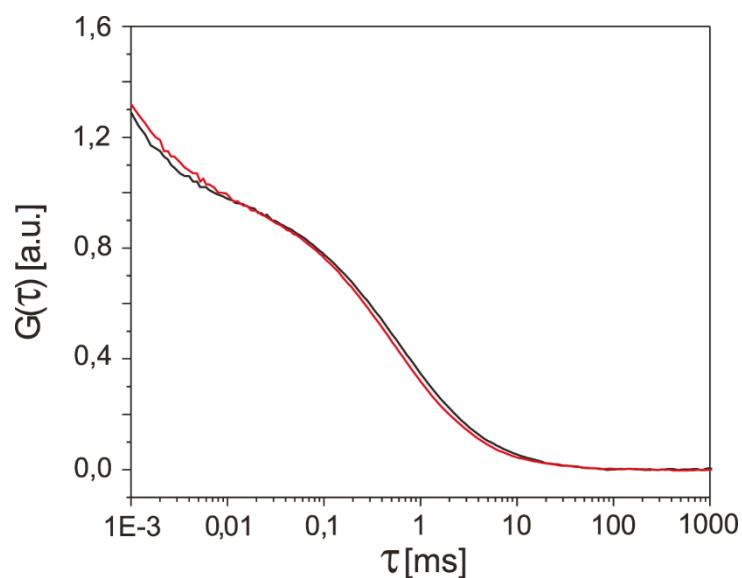


Fig.3.7. Effects of water evaporation on mNALP stability

The autocorrelation curves (ACFs) for Fola-mNALPs prepared by the microfluidic mixing method under optimal conditions; $C_{DNA} = 40$ nM, $\rho = 5$ (black), and after 35-fold sample concentration (water evaporation at 45 °C in high vacuum) and re-dilution. Curves show negligible deviation, revealing the stability of the particles after concentration up to 1,4 μ M. Adapted from Krzysztoń et al.¹⁷⁵

Next, we test the stability of folate-functionalized mNALPs and their affinity to interact with blood serum proteins. We perform the experiments in PBS buffer with increasing volume fraction of serum or plasma ranging between 10 to 80% (v/v) serum/PBS and 30 to 90% (v/v) plasma/PBS. Fola-mNALPs are concentrated 10 times and re-diluted to the Cy3-dsDNA starting concentration of 40nM in serum/PBS or plasma/PBS. Independent experiments show that the 35-fold concentration of mNALPs by solvent evaporation does not lead to aggregation or significant material losses during the process (Fig.3.7.).

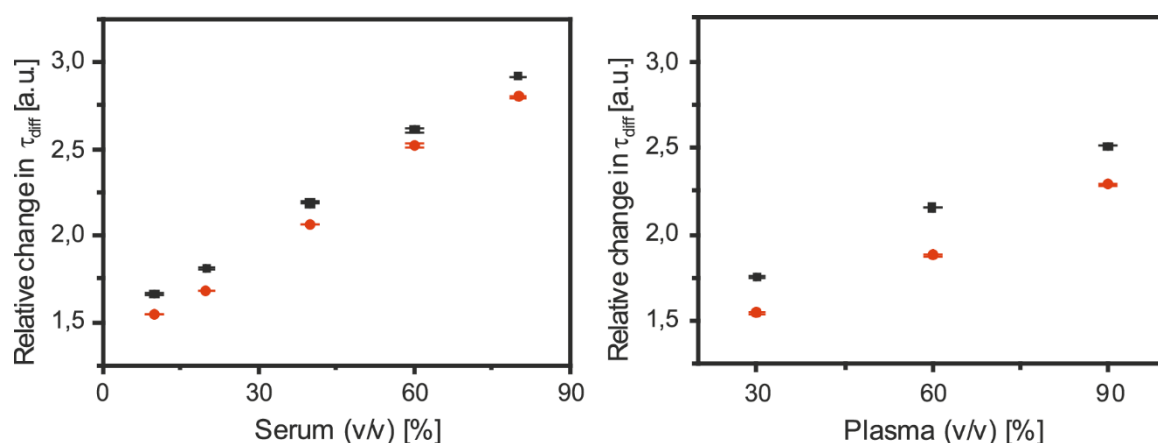


Fig.3.8. Effects of serum/plasma concentration on diffusive behaviour of Cy3 and Cy3-dsDNA

The relative changes in diffusion time (τ_{diff}) of Cy3 (black) and Cy3-DNA (red) in function of increased serum and plasma content (given as volume fraction, % (v/v)). The differences are tracked in reference to corresponding diffusion times in water. The similar linear changes suggest that increase in viscosity is the dominant factor in diffusive behaviour of both Cy3 and Cy3-DNA. Adapted from Krzysztoń et al.¹⁷⁵

We monitor the sizes of particles over 7 days using FCS in relation to the Cy3-dsDNA reference diluted in the same medium. Additionally, we validate the diffusive behaviour of Cy3-dsDNA in serum and plasma samples for proper evaluation of diffusive components present in investigated samples. Similar increases in relative diffusion times are present for Cy3 and Cy3-dsDNA samples suggesting that the changes are resulting from viscosity effects (Fig.3.8.).

We normalize the obtained values of hydrodynamic radiuses of particles by the value measured at the first day of experiment. The particle size did not change significantly over the time of entire experiment in both blood plasma and serum. Similarly, like in the case of synthesis optimization studies, the experimental variance of particle size determined in individual measurements is presented as error bars on the Fig.3.9. The measured particle fraction decreases over the time span of the experiment and reaches the lowest level

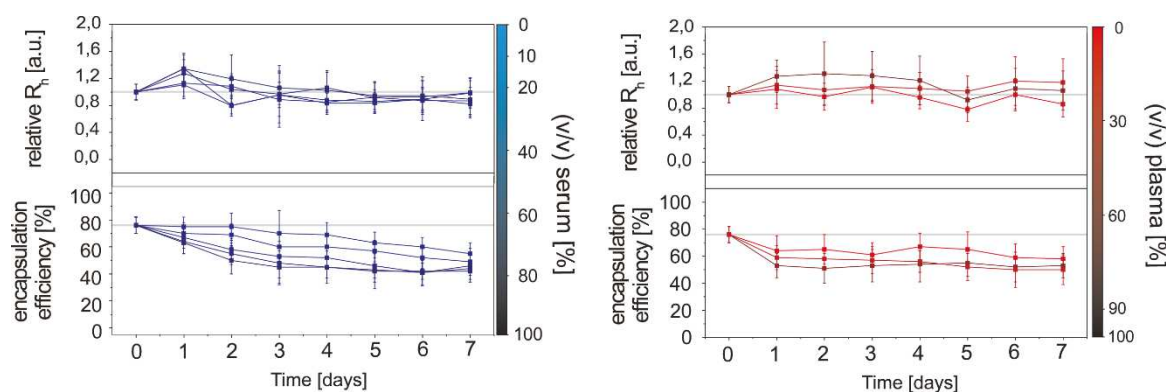


Fig.3.9. Stability of Fola-mNALPs in blood serum and plasma

The stability of Fola-mNALPs in blood serum (left) and plasma (right). The time dependent changes in relative hydrodynamic radius and encapsulation efficiency are given. The changes are related to values measured at day 1. Adapted from Krzysztoń *et al.*¹⁷⁵

of 50% in highest concentrations of serum/plasma after 3 and 1 day in blood serum and plasma respectively. Since the measurements significantly affected by high fluorescence intensity spikes are disregarded from the experiment, the decrease in particle fraction can be linked to increased aggregation. We observe the relatively fast degradation of particles and broadening of size distribution represented as increase in the size of error bars in blood plasma samples compared to serum. The effect can be associated with fibrinogen coagulation that is not present in blood serum.

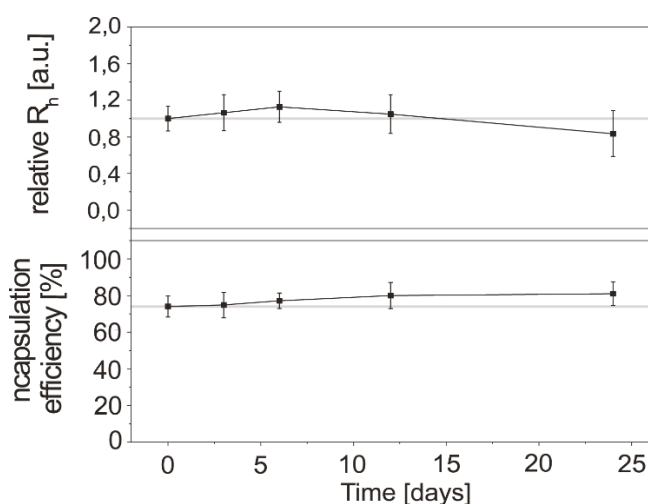


Fig.3.10. The shelf life time of Fola-mNALPs

The time dependent changes in relative hydrodynamic radius and encapsulation efficiency are given. Changes are related to values measured at day 1. Adapted from Krzysztoń *et al.*¹⁷⁵

Additionally, we investigate the colloidal stability of Fola-mNALPs that reveals the room temperature shelf life-time of at least 24 days. The data analysis are performed in the same way as the of plasma/serum stability experiments (Fig.3.10.).

3.1.4. Cell binding and uptake experiments

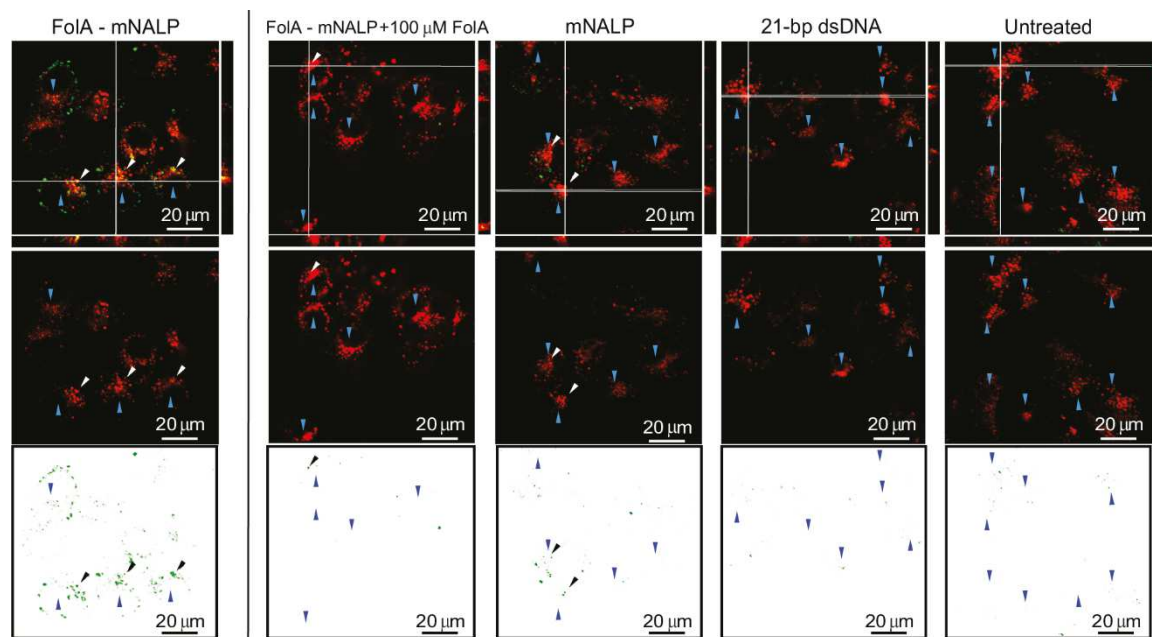


Fig.3.11. Specific binding and uptake of Folate-mNALPs - confocal microscopy

The confocal images of KB/WT cells showing co-localized late endosomes/lysosomes (stained with LysoTracker DND-99, red) and mNALPS (labelled ATTO488-dsDNA, green) - top row. The yellow regions indicate the co-localization of both red and green signals. The co-localization points are also marked with black tilted arrows. Blue vertical arrows indicate the perinuclear region as deduced from characteristic arch shape of late endosome distribution. The middle and bottom rows present the separated red and green channels respectively. To increase the contrast the background in the green channel is shown in white. From the left to right: data for Folate-mNALPs are compared to the controls (Folate-mNALPs in the presence of excess folate, non-targeted mNALPs, naked dsDNA and untreated cells). Reprinted from Krzysztoń et al.¹⁷⁵

Further, we verify the specific binding to folate receptors and uptake of folate-functionalized mNALPs in *in vitro* studies using wild-type epithelial carcinoma KB cells (WT/KB). The folate receptors are significantly overexpressed in many types of human cancers and the folate-mediated endocytosis is often utilized for specific cancer targeting of nanoparticles (61). To ensure high-levels of overexpressed folate receptors, WT/KB cells are cultivated in low-folate-content RPMI 1640 medium (~5 nM). We investigate the specificity and efficiency of uptake both qualitatively and quantitatively using confocal imaging and flow cytometry respectively. In both cases the 21 bp dsDNA used for mNALP synthesis are doubly labelled with ATTO488 (ATTO488-dsDNA).

We perform the confocal imaging on cells incubated in Folate-mNALP-containing folate-free RPMI1640 medium. We use the total ATTO488-dsDNA concentration of 50 nM and 50 min incubation time. Cells incubated with bare ATTO488-dsDNA, non-folated

mNALPs and untreated cells are taken as negative controls. Additional control of cells incubated with Fola-mNALPs and with folate receptors saturated with 100 μM of folate is used to verify the particle-receptor binding and receptor-mediated endocytic uptake. We analyse the intracellular distribution of mNALPs using lysosome/late endosome staining with LysoTracker Red DND-99. The number of cell-bounded/internalized particles is significant only in case of Fola-mNALP sample (Fig.3.11, green). Low number of cell-bounded particles are present in both mNALP controls, in the amounts comparable to the negligible unspecific bonding levels of bare ATTO488-dsDNA. Fluorescence signal of Fola-mNALPs co-localize significantly with the lysosomes/late endosomes (Fig.3.11, overlay), which accumulates mostly in the perinuclear region (Fig.3.11, red). Those findings suggest that Fola-mNALPs are internalized inside the cells mostly due folate-receptor-mediated endocytosis, since competitive inhibition of receptors and lack of folate targeting reduces the uptake/binding levels drastically. Moreover, the strong co-localization of lysosome/endosome and Fola-mNALP signals indicates that most of the internalized particles reside inside those organelles.

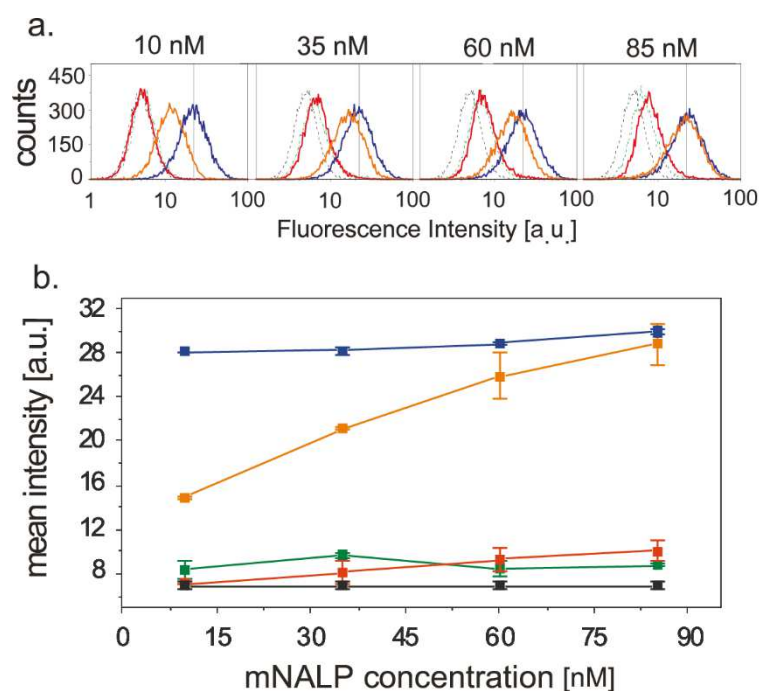


Fig.3.12. Studies of dose dependence on Fola-mNALP binding and uptake by folate-receptor-overexpressing KB/WT cells

a) The fluorescence intensity distributions of cells incubated with ATTO488-labelled mNALPs as a function of concentration. b) The corresponding mean fluorescence intensities. The colours represent as follows: blue, Fola-mNALPs; orange, Fola-mNALPs after a brief acidic washing step; red, non-targeted mNALPs; green, non-coated ATTO488-dsDNA; black, untreated cells. Adapted from Krzysztoń *et al.*¹⁷⁵

Further, we quantify the dose dependence and kinetics of Fola-mNALP binding and uptake using flow cytometry. Here, we use the same controls as in case of confocal imaging (excluding the competitive blocking of folate receptors). We distinguish between the internalized and surface-bound particles by detachment of mNALPs from the cell-surface receptors. Binding of folate to folate receptors is sensitive to environment acidification and folate is released from the receptors at low pH. In order to release the surface-bounded Fola-mNALPs cells are briefly exposed to acidic condition in two additional washing steps with ice-cold acidified saline pH 3,4 (~ 10 s each washing step).⁵⁷ Cell viability after low-pH treatment was verified with Trypan blue assay revealing 92,3% viable cells. During the experiments, we use two batches of Fola-mNALP-treated cells. Additional cell batch is briefly exposed to low-pH conditions. We use the difference in detected fluorescence intensities between those two batches as a measure for amount of surface-bound particles.

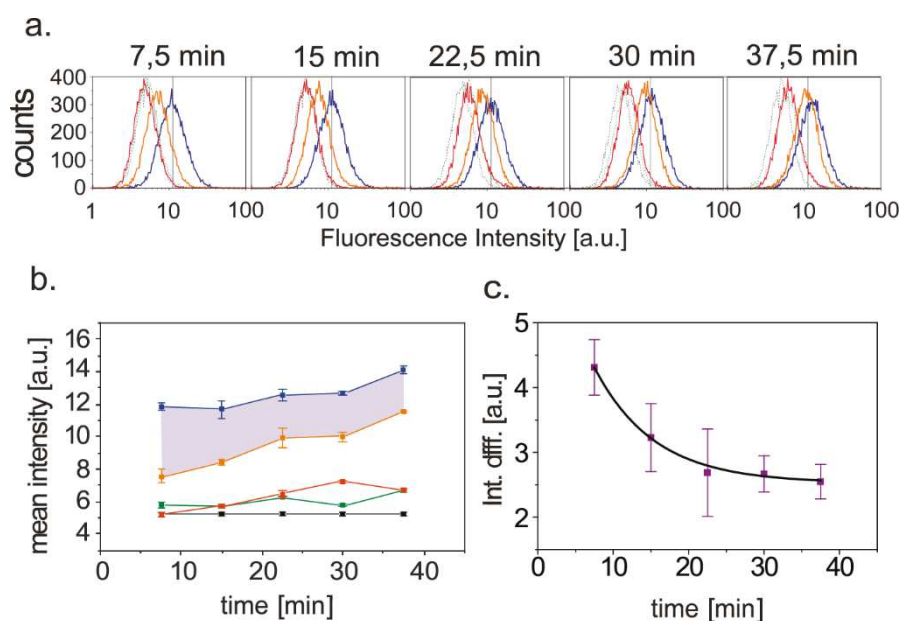


Fig.3.13. Studies of time dependence on Fola-mNALP binding and uptake by folate-receptor-overexpressing KB/WT cells

a) The fluorescence intensity distributions of cells incubated with 50 nM of ATTO488-labelled mNALPs as a function of incubation time. b) The corresponding mean fluorescence intensities. The colours represent as follows: blue, Fola-mNALPs; orange, Fola-mNALPs after a brief acidic washing step; red, non-targeted mNALPs; green, non-coated ATTO488-dsDNA; black, untreated cells. The purple areas in b) and trace in c) shows the difference between mean fluorescence intensities of acid-treated and acid-non-treated cells and represents the fraction of surface-bound Fola-mNALPs. The black line on c) shows the exponential fit to the data ($k = (0.13 \pm 0,02) \text{ min}^{-1}$, $r^2 = 0.993$). Adapted from Krzysztoń *et al.*¹⁷⁵

Firstly, we incubate the WT/KB cells for 50 min with increasing concentration of Fola-mNALPs ranging between 10 and 85 nM of ATTO488-dsDNA. The mean fluorescence intensity of cells not exposed to acidic conditions is almost constant between all used concentrations suggesting that the saturation of folate receptors even at lowest used concentration of particles is achieved (Fig.3.12.). Contrary, cells exposed to acidified saline show an increase in fluorescence intensity with increasing particle concentration revealing rise in particle uptake. Negative controls of bare ATTO488-dsDNA and non-folated mNALPs show only a minor increase (~20%) in fluorescence intensity, revealing low unspecific binding that is also in accordance with confocal microscopy findings.

Secondly, we investigate the kinetics of Fola-mNALP uptake. WT/KB cells are incubated with Fola-mNALPs containing 50 nM ATTO488-dsDNA in gradually increasing time periods ranging between 7,5 and 37,5 min. The increase in incubation time directly correlates with increase in cell fluorescence (Fig.3.13.). The difference between low-pH-treated and untreated batches decreases exponentially revealing the kinetic uptake rate of $k = (0,13 \pm 0,02) \text{ min}^{-1}$ and levels off after at longer incubation times. The finding suggests that balance between receptor binding and cell internalization is reached within first 20 min of incubation. The negative controls of bare ATTO488-dsDNA and non-folated mNALPs show only minor increase in fluorescence intensity over time reaching levels observed in previous studies of concentration dependent binding/uptake.

3.1.5. Silencing experiments

We evaluate the silencing activity of siRNA-loaded Fola-mNALPs using a luciferase assay. We use the KB cells stably expressing enhanced Green Fluorescent Protein / Luciferase fusion protein (eGFPLuc/KB). Cells are incubated with Fola-mNALPs containing 50 nM of siRNA in Folate-free RPMI 1640 medium. Two siRNA sequences are used: siGFP sequence, that targets the mRNA encoding eGFPLuc fusion protein and siCtrl control sequence to monitor potential false positive unspecific effects. The cells incubated with the non-folated mNALPs are taken as negative control. Moreover, the increased release of particles is facilitated in an additional batch of cells incubated in medium supplemented with 100 μM chloroquine - endosomolytic agent. After 48h of cell incubation, we assess the silencing activity by monitoring luciferase activity in a luminometric assay using a plate reader. The amounts of luciferase reaction product, luciferin, is quantified by the detected fluorescence intensity levels. We monitor the relative

changes in fluorescence intensities in comparison to untreated eGFPLuc/KB cells. The down-regulated luciferase activity is only observed in siGFP Fola-mNALP-treated cells in presence of chloroquine (Fig.3.14.). No unspecific gene silencing mediated by siCtrl sequence under all tested conditions can be seen. Presented results together with endosome co-localization studies suggest that particles are not capable of efficient escape from endosomes. Although, when released from endosomal environment by additional means, mNALPs are capable of releasing encapsulated siRNA into the cytoplasm.

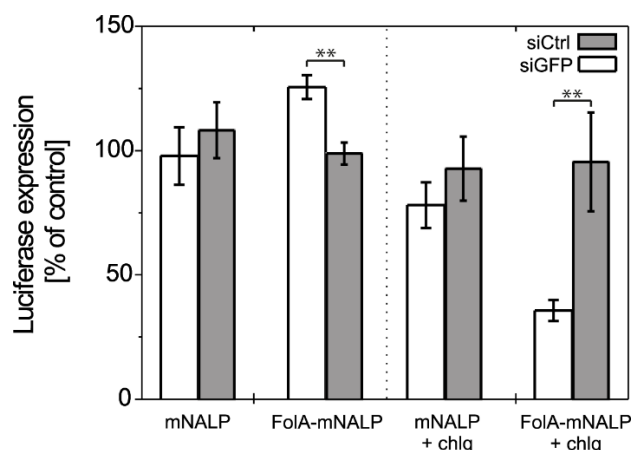


Fig.3.14. Quantification of silencing efficiency of Fola-mNALPs in KB cells expressing the eGFPLuc fusion protein (KB/eGFPLuc cells)

Cells are incubated with siGFP-mNALPs (white) and Fola-mNALPs (grey) in the presence (right panel) and absence (left panel) of endosomolytic agent - chloroquine (chlq, 100 μ M). Luciferase expression changes are presented as relative changes compared with untreated control cells. Adapted from Krzysztoń *et al.*¹⁷⁵

3.2. siRNA mediated mRNA degradation kinetics

In this chapter, we analyse the kinetics of siRNA-mediated gene silencing on a single-cell level and use the determined kinetic parameters describing the process to quantify the silencing efficiency in a robust manner.

In standard flow cytometry or plate reader *in vitro* assays the quantitative assessment of siRNA silencing efficiency is carried out on the level of cell population, by indirect measurement of protein levels. Here, the fluorescence intensity of reporter proteins or the products of their enzymatic activity (as in case of fluorescent protein reporters or luciferase reporters respectively), serves as a measure for the silencing efficiency. Importantly, the outcome of discussed assays is sensitive to the selected time points of measurement. Although flow cytometry and plate reader can be also used for kinetic measurements of fluorescence, the single-cell context of measured kinetics is then lost.

In contrast, quantitative time-lapse microscopy can resolve the full dynamic range of single-cell fluorescence intensity changes. By careful calibration and conversion of fluorescence intensities the numbers of expressed fluorescent reporter proteins can be derived and subsequently the expression kinetics can be mathematically modelled. The presented analytical approach gives direct access to the kinetic parameters of expression processes extending the quantitative single-cell analysis to the dynamic context. In comparison to standard methods based on fluorescence intensity analysis, the determined kinetic constants are time independent and constitute the absolute measures describing gene expression kinetics. Moreover, the single-cell level of analysis offers access to features that are not available on the population-averaged level that includes cell-to-cell variability and behaviour of rare and otherwise poorly detectable cell subpopulations.

We use quantitative epifluorescence time-lapse microscopy combined with micro-patterned cell culture substrates (Live-cell Imaging of Single-Cell Arrays, LISCA) to investigate the siRNA-induced silencing activity on the single-cell level. We utilise the changes in expression of enhanced Green Fluorescent Protein (eGFP) to quantify the silencing efficiency of delivered siRNA. Firstly, we present the quantitative outcome of direct fluorescence analysis following pDNA/siRNA transfection, both on single-cell a population-averaged level and compare the obtained results. Secondly, we estimate the silencing efficiency as a relative fold-change in mRNA degradation rate constants caused by siRNA activity. The mRNA degradation rate constants are obtained by mathematical modelling of eGFP expression following eGFP-mRNA transfection. Second, eGFP-siRNA delivery is used to modulate mRNA expression time profiles and observed changes are thoughtfully analysed. The internal reference of second, non-homologous reporter protein (Cayenne Red Fluorescent Protein, CayRFP) is used as an expression reference. Additionally, the correlations between kinetic parameters describing expression of both eGFP and CayRFP are analysed giving detailed insights into the processes of mRNA delivery and siRNA-induced silencing.

3.2.1. Dual-reporter assays

Silencing efficiency of siRNA is quantified using two, pDNA- and mRNA-based dual-reporter assays. We investigate the relative changes in expression of siRNA-targeted eGFP in relation to CayRFP reference (Fig.3.15.). Use of two non-homologous fluorescent proteins expressed from two identically controlled genes helps to decouple the silencing

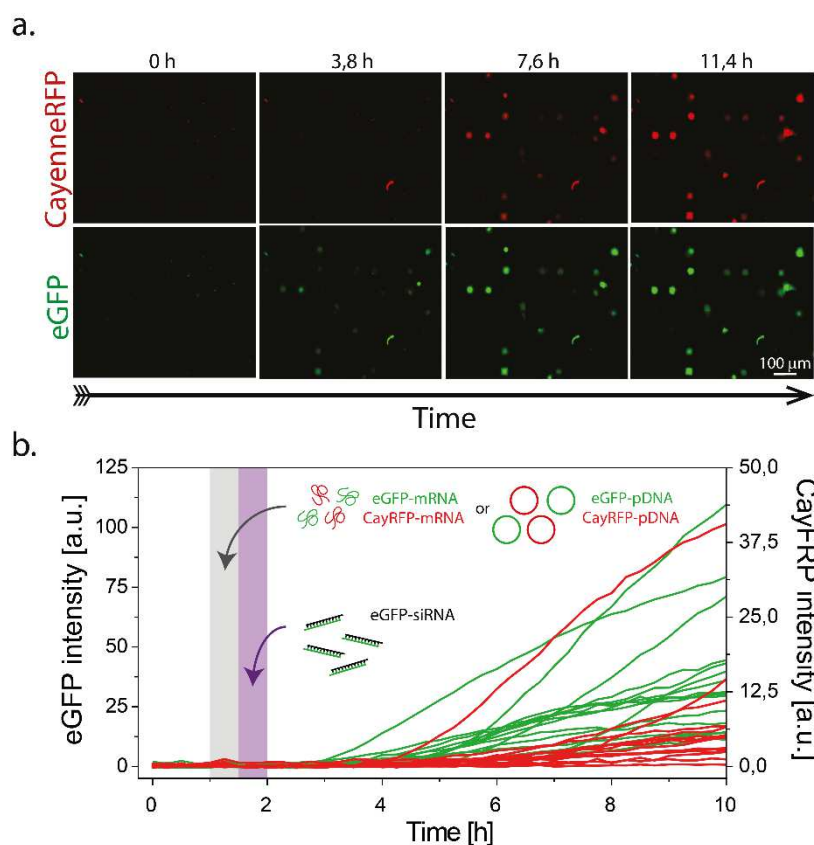


Fig.3.15. Dual-reporter assay in time-lapse fluorescence imaging experiments

The cells (as an example A549 cells) are seeded on the micro-pattern and spread on fibronectin-coated adhesion sites (b). After pDNA/mRNA and subsequent siRNA transfection the changes in single-cell fluorescence of CayRFP reference and eGFP target are monitored (a) and can be quantified (b) yielding in fluorescence intensity time-courses. The incubation times used for transfection of the indicated RNAs are indicated in grey and purple. The incubation periods of mRNAs and siRNA transfection are indicated in grey and purple respectively (b).

process from other, extrinsic factors that contributes to the fluctuations in protein expression levels. Both, eGFP- and CayRFP-encoding plasmids (pDNA^G and pDNA^R respectively) contain the same constitutive CMV promoter. Similarly, both eGFP- and CayRFP-mRNA (mRNA^G and mRNA^R respectively) constructs contain Kozak consensus sequence, initiation codon (AUG), anti-reverse CAP analog (ARCA) and poly-A tails of the same length (105 - 120 bases) to ensure the same efficiency of translation of both gene constructs (Fig.3.16.). In addition, both gene sequences have similar length, expressed proteins have similar size and undergo an oxygen-related maturation processes. pDNA^G and pDNA^R or mRNA^G and mRNA^R are premixed in an equimolar ratios prior to complexation with lipofectamine. In this way, the statistical variation between the numbers of eGFP- and CayRFP-encoding nucleic acids per transfection complex is minimised. Our

experimental assumption provides that on average the equimolar ratio remain preserved during the cellular uptake and release of complexes.

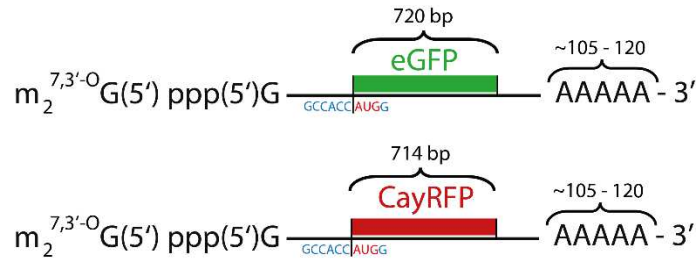


Fig.3.16. The schematic representations of eGFP- and CayRFP-mRNA sequence constructs

The schematic representations of eGFP- and CayRFP-mRNA sequence constructs used during experiments ($mRNA^G$ and $mRNA^R$ respectively). Both constructs bear a Kozak translation initiation sequence facilitating efficient initiation of translation, a poly-A tails of a length ranging between 105 and 120 bases and anti-reverse CAP analog ($m^2 7,3'-O G[5']ppp[5']G$, ARCA) at the 5' end for increased translation efficiency.

3.2.2. Comparison of single-cell and population-averaged fluorescence analysis

The pDNA-based dual-reporter assay is used to investigate the siRNA activity by the direct analysis of fluorescence intensities. We perform the analysis in analogy to standard flow cytometry or plate reader assays. The dual-reporter assay relies on two sequential transfections. Firstly, plasmid reporters are internalised by the cells during 1h incubation with pDNA/lipofectamine complexes. Secondly, the transfection medium is exchanged and eGFP-targeting siRNA is delivered during 30 min incubation with siRNA/lipofectamine complexes immediately after first incubation is finished. Following the second incubation the time-lapse imaging is started. We use the cells transfected only with pDNA as a control. Huh-7 cells are used.

The representative examples of single-cell fluorescence intensity time-courses obtained for control cells are shown in Fig.3.17.a. as grey lines. Single-cell time-courses show sigmoidal time dependence with the time of fluorescence onset that varies significantly between particular cells. Fluorescence intensities of the individual cells level up and reach significantly diverse values. Time-courses of siRNA-treated cells show reduced eGFP fluorescence intensity levels compared to the control. Population-averaged fluorescence intensity presents a gradual increase in both experimental conditions over the time of experiment and reveals the qualitative difference when compared to single-cell data. Population-averaged fluorescence intensities are also altered by the activity of siRNA revealing significant difference between eGFP expression time-course of siRNA-treated

and control cells (Fig.3.17b.). Small differences in CayRFP expression are present in the initial stages of protein expression between siRNA-treated and control cell populations both on single-cell and population level. This effect can be attributed to unspecific activity of siRNA or other side-effects.^{201, 202}

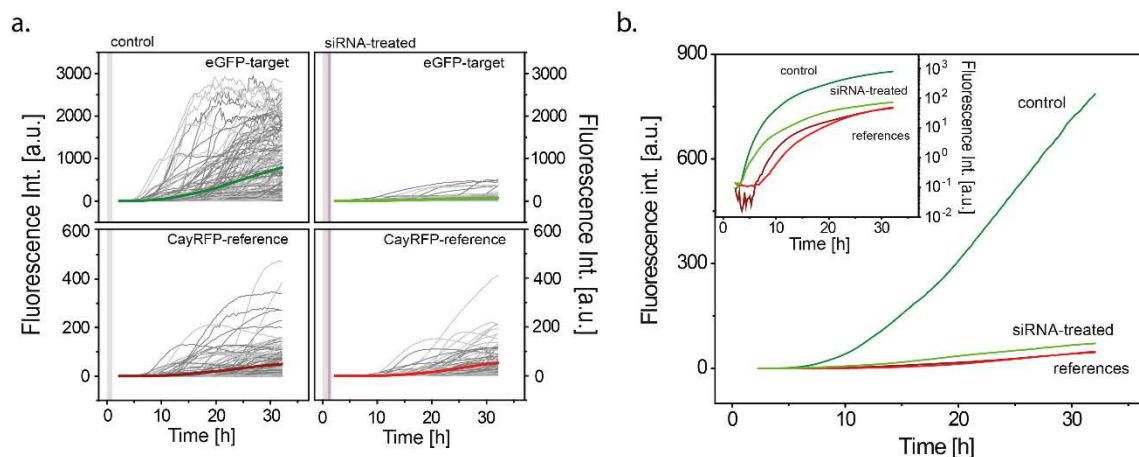


Fig.3.17. Single-cell pDNA expression dynamics

(a) Single-cell time-courses of eGFP and CayRFP fluorescence intensities (grey lines) following transfection with plasmid DNAs vary significantly between each other. On average, the maximum fluorescence intensities decrease following siRNA delivery (top row: siRNA-treated vs. control cells). Grey and purple areas denote the periods of cell incubation with pDNA and siRNA transfection complexes respectively. (b) Population-averaged eGFP and CayRFP time-courses shown as green and red lines (both in (a) and (b)). In the insert in (b), population-averaged data are plotted in a log scale.

Next, we evaluate the silencing efficiency and discuss the differences that arise when the analysis is carried out on population and single-cell level. In this experiment, we quantify the silencing efficiency by a change in the relative fluorescence that is defined as fluorescence intensity ratio eGFP/CayRFP of the targeted eGFP in relation to internal CayRFP reference. Fig.3.18.a presents the values of relative fluorescence calculated from the population-averaged $\langle \text{eGFP} \rangle$ and $\langle \text{CayRFP} \rangle$ fluorescence intensities at five selected time points. Presented analysis are analogous to plate-reader-based assays. In order to eliminate the effect of the different quantum yield of both fluorescent proteins the average of relative fluorescence values from selected time points obtained for the control cells is taken as reference point. Normalized data are presented in Fig.3.18a. on the right axis of the plot as a percent of the reference. Based on the normalization the relative fluorescence is found to decrease from 62,5% to 8% between 10 and 30 hours post transfection. In a second round of analysis, the population average of single-cell relative fluorescence values $\langle \text{eGFP}/\text{CayRFP} \rangle$ at five selected time points are considered. We select the reference time

point for normalisation in a way that is analogous to the procedure described for population-averaged data. Similar analysis might be performed using flow cytometry assays. The single-cell-level analysis revealed the decrease in relative fluorescence from 21,7% to 0,59% between 10 and 30 hours post transfection (Fig.3.18b.).

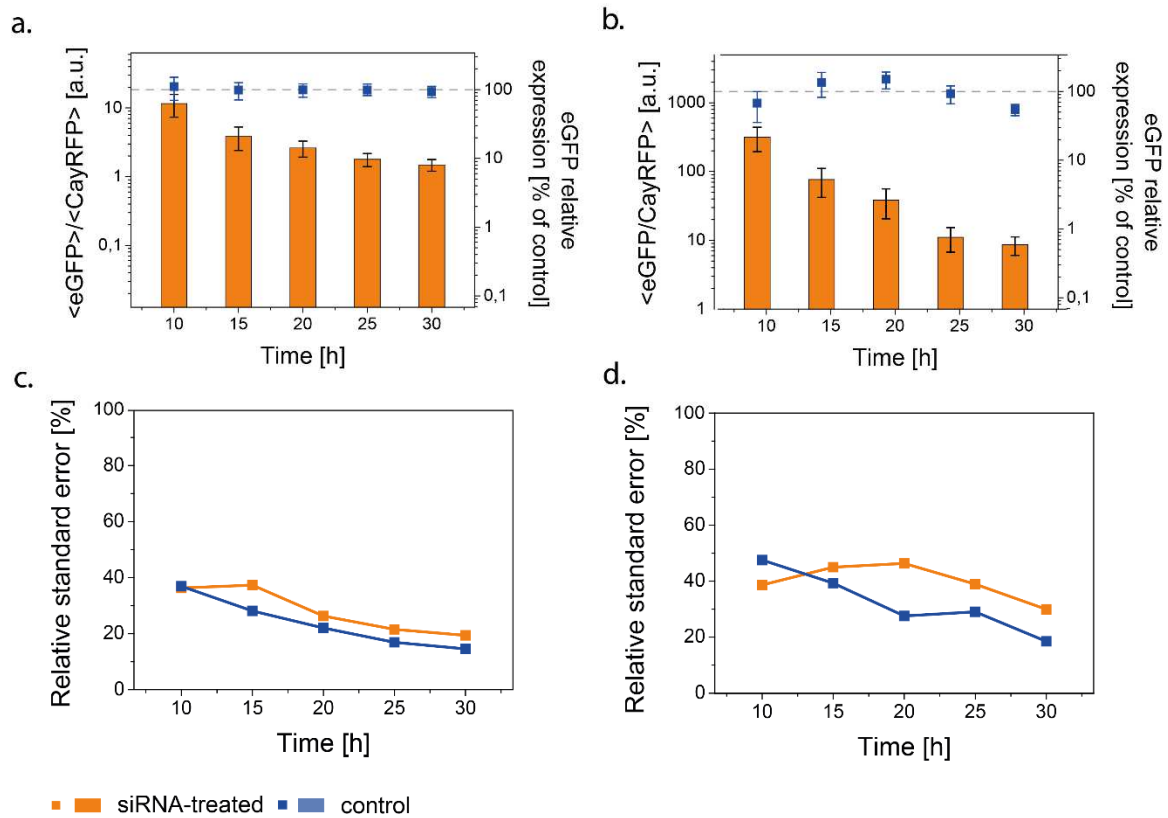


Fig.3.18. Single-cell vs. population-averaged fluorescence analysis – silencing efficiency

Population-averaged $eGFP/CayRFP$ relative fluorescence intensity (a) and average single-cell $eGFP/CayRFP$ relative fluorescence intensity (b) plotted as a function of time (blue: control cells; orange, siRNA-treated cells). Five selected time points are presented. The single-cell data of siRNA-treated cells shows a stronger decrease in relative fluorescence reflecting the silencing efficiency than does the population-averaged data. Relative error of the $eGFP/CayRFP$ relative fluorescence intensities obtained from (c) population-averaged and (d) single-cell data analysis.

Notably, the outcome of both analytical approaches varies significantly. The explanation can be found when the cellular noise in protein expression levels is considered (120). Fig.3.19a. shows the distributions of the relative fluorescence for both siRNA-treated (orange) and control cells (blue). Obtained single-cell distributions vary over two and three orders of magnitude in siRNA-treated and control cells respectively. Shift between mean values of those distributions reflects the silencing efficiency and is smaller than the widths of distributions in each of selected time points. In addition, scatter plots of $eGFP$ vs. $CayRFP$ fluorescence intensities reveal the correlations between single-cell

values (Fig.3.19b.). This observation suggest that the total cellular noise is significantly affected by the extrinsic contribution. Importantly, the extrinsic noise is significantly reduced when the expression control is referenced at the level of single-cells, which demonstrates the significant benefits of single-cell approach.

Yet, the major drawback of quantifying the siRNA silencing efficiency by comparative changes in reporter fluorescence intensities is the fact that the outcome is time dependent. Even when the CayRFP expression reference is in use, the changes in relative eGFP/CayRFP fluorescence intensity do not reach the steady value over the 30 h post transfection (Fig.3.18.a.b., orange). Additionally, the measurements performed at early time points are affected by significant standard error limiting the accuracy of the measurement (Fig.3.18c. and Fig.3.18d.). The described features limit the analytical utility of direct fluorescence analysis and introduce method-related biases. To overcome this problem, in further experiments we exploit the full kinetics of measured single-cell fluorescence time-courses and derive the mRNA degradation rate constants using a mathematical model of protein expression.

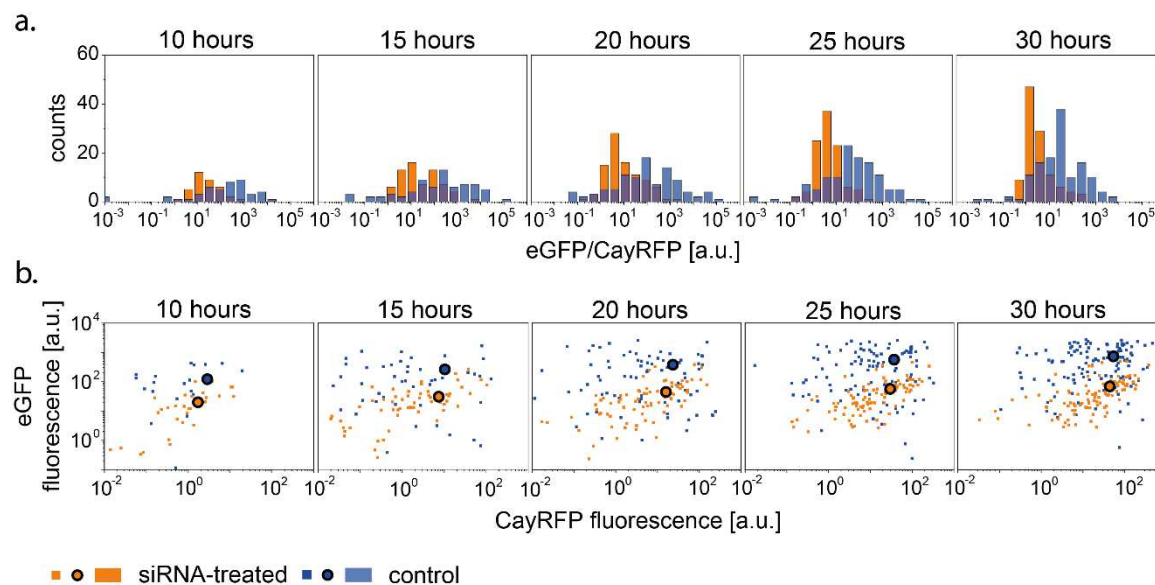


Fig.3.19. Single-cell fluorescence analysis – population distributions

(a) Distribution of single-cell eGFP/CayRFP relative fluorescence intensities (orange: siRNA-treated cells, blue: control cells). (b) Single-cell eGFP vs. CayRFP fluorescence intensity scatter plots for various time points. The distribution of clusters reveals both an extrinsic and intrinsic contribution to cellular noise. Black-bordered circles represent the population averages.

3.2.3. Kinetic analysis of mRNA expression time courses

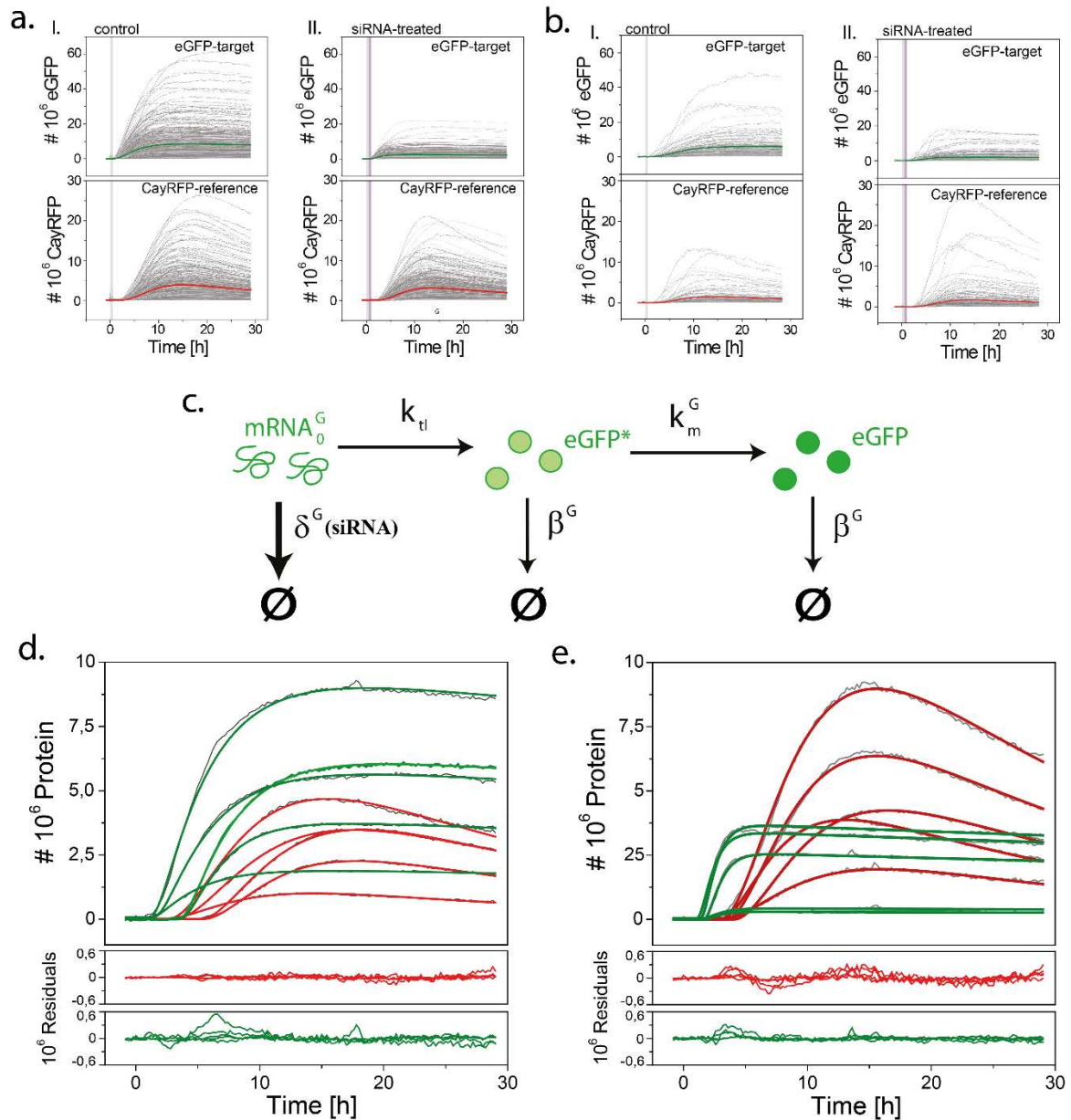


Fig.3.20. Single-cell mRNA expression kinetics in the presence of siRNA

Top panel: Single-cell time-courses of eGFP and CayRFP expression obtained using Huh-7 (a) and A549 cells (b) treated with eGFP- siRNA and control cells. Coloured lines represent the population averages. Grey and purple bars denote the incubation periods of mRNA and siRNA transfection respectively. Middle panel: Schematic drawing of the kinetic model used in the analysis (c). The model accounts for mRNA translation, fluorescence protein maturation, mRNA and protein degradation as first order mass action processes. Bottom panel: The representative time-courses of eGFP and CayRFP expression in siRNA-treated (e) and control cells (d) together with related fits of the mathematical model. Residuals indicate agreement of fits and data.

To obtain an unbiased, time-independent measure for siRNA silencing efficiency we derive the absolute values of mRNA degradation rate constants (δ) by kinetic analysis of single-cell fluorescence time-courses. To this end, the mathematical modelling of expression kinetics is required. For practical reasons it is convenient to reduce the complexity of the molecular network underlying the expression by exploiting the mRNA delivery instead of pDNA used in previous experiments. Contrary to pDNA, mRNA does not require nuclear entry for efficient expression of encoded genes and omits completely the steps of transcription, nuclear transport and maturation of produced mRNA. The mRNA-based dual-reporter assay comprise of two sequential transfections. Firstly, the synthetic mRNA^G and mRNA^R constructs are delivered during 30 min cell incubation with mRNA/lipofectamine complexes. Secondly, the transfection medium is exchanged and a second 30 min incubation with eGFP-siRNA/lipofectamine complexes is performed. Importantly, we convert the obtained single-cell fluorescence intensities into the numbers of expressed proteins during the calibration procedure using a microfluidic device. We use the cells transfected only with mRNA as a control. Experiments are performed on Huh-7 and A549 to confirm the generality of the findings.

The representative examples of single-cell time-courses are presented in the Fig.3.20a. and Fig.3.20b.. The transient expression of mRNA presents more homogenous time profiles of protein numbers expressed in each single cell within the population compared to pDNA expression. Notably, the distribution of onset times is visually narrower and the shape of individual time-courses are more similar to each other. There is a significant difference between the maximal number of expressed eGFP molecules between siRNA-treated and control cells, both on single-cell and population-averaged level, as in the case of pDNA transfection. The kinetic model of protein expression following mRNA delivery comprises four processes (Fig.3.20c.). The same model applies for both reporter proteins. mRNA released into the cytoplasm of each cell ($mRNA^{G_0} = m^{G_0}$) serves as a template for protein translation. Translated, non-mature proteins ($eGFP^*$) undergo maturation into the fluorescent, mature state ($eGFP$). Both, mRNA and proteins also undergo a degradation process. We assume that the degradation kinetics of mature and non-mature proteins is described by the same parameters. All processes are modelled using first order mass action kinetics. The related set of differential equations (ODEs, eq. 2.42-2.44.) is given in experimental section. Mathematical expression describing the time-dependent changes in the fluorescent protein numbers (eq. 2.45.) is obtained by solving given equation

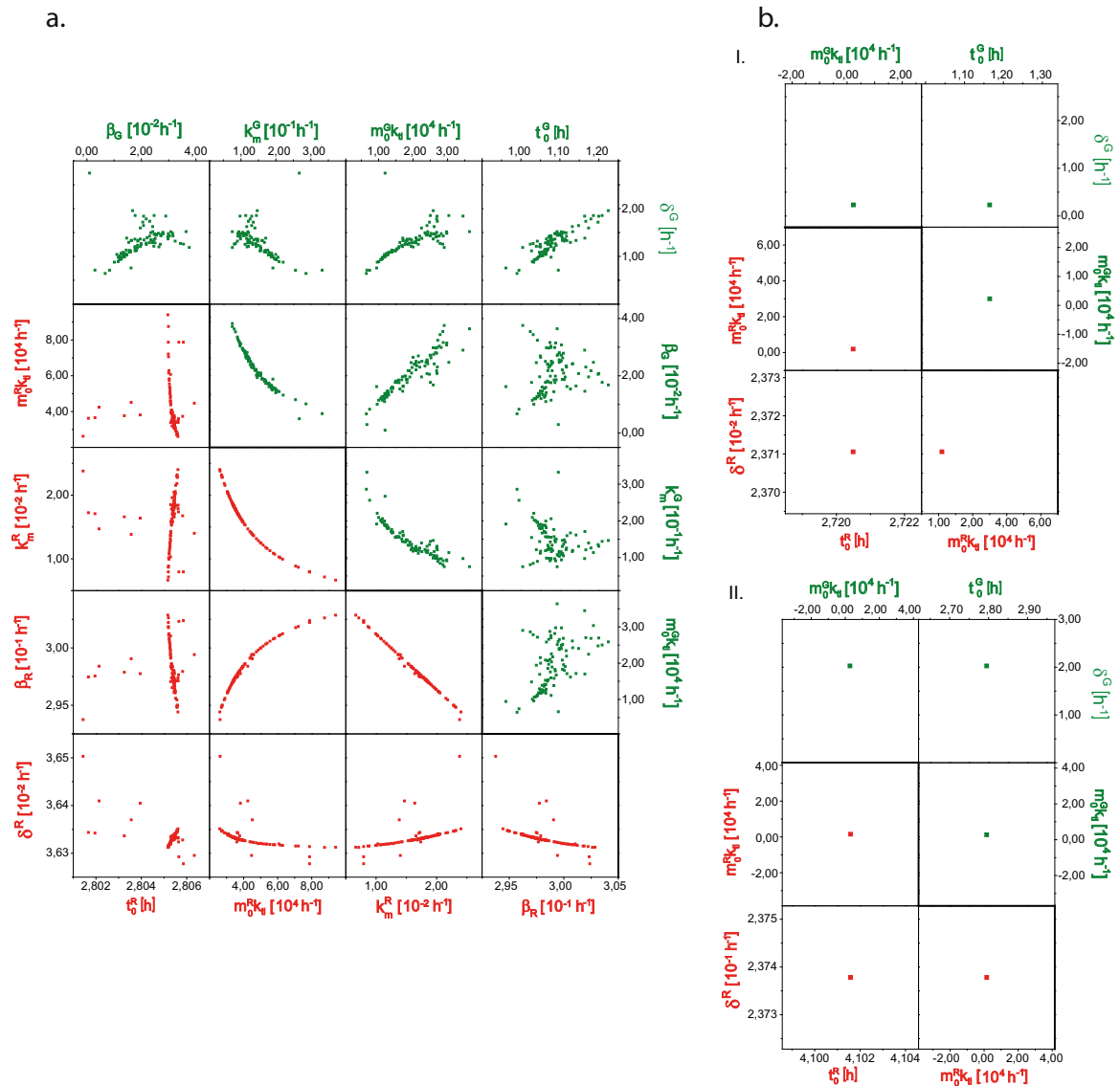


Fig.3.21. Identifiability of fit parameters

a) The repeated, independent fits to the same experimental time - course yielded varying interdependent parameter values when all free parameters underwent optimization. Plots present the correlations between pairs of parameters obtained in one hundred iterative fits of a two, eGFP and CayRFP, expression time-courses derived from single Huh-7 cell from control population. The initial values of parameters are varied between each fitting run. b) The parameter correlations are no longer visible (parameters have converged to a single point) when the protein maturation and degradation rate constants are fixed at the values determined during translation inhibition experiments. The parameter values of iterative fits are converging towards single, particular value. The effect is seen for both siRNA –treated (II) and control (I) cells.

set and used while fitting the experimental data. Fitting of CayRFP and eGFP expression time-courses is done independently. This procedure resulted in four independent kinetic rate constants related to each of described kinetic processes and, additionally, the expression onset time as free parameters. Importantly, the initial number of mRNA molecules and the translation rate constant are fitted jointly as they are not separately

identifiable by the model. The jointed parameter mok_{tl} formally represents the initial translation rate. In case of siRNA-treated cells, both the unspecific and siRNA-related mRNA degradation are modelled by first order mass action kinetics. It implies that the effective mRNA degradation rate constants determined during the experiments are the sums of the rate constants describing both processes ($\delta^G(\text{siRNA}) = \delta^G + \delta^{G-\text{siRNA}}$).

The chosen model agrees with the data in case of both siRNA-treated and control cells as demonstrated by the residuals in Fig.3.20d. and Fig.3.20e.. Although, the repeated, independent fits to the same experimental time-course result in varying and interdependent parameter values when all free parameters have undergone optimization (Fig.3.21a.). This indicates that the parameter estimates are not unique. Such behaviour is commonly referred to as a structural identifiability problem.²⁰³ To eliminate described ambiguities, we further simplify the model by eliminating the maturation and degradation rate constants (k_m and β) from the pool of free parameters (Fig.3.21b.). Both values are determined in following independent translation inhibition experiments and fixed during analysis of mRNA expression time-courses.

3.2.4. Translation inhibition experiments

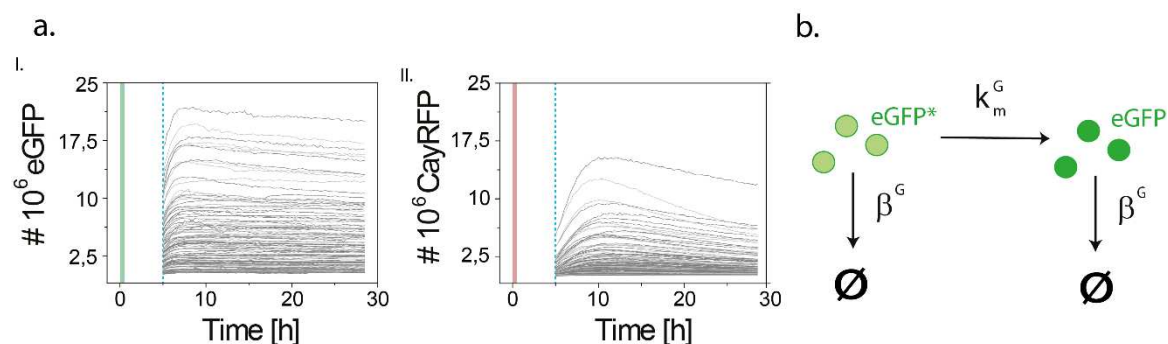


Fig.3.22. Translation block experiments – single-cell time-courses and mathematical model

(a) Single-cell time-courses of eGFP and CayRFP fluorescence following the blockage of translation. The green and red bars indicate the time of mRNA transfection. The onset of translation blockade is taken as time 0 and is represented as dashed line. (b) The reduced kinetic model used for data evaluation. Model accounts for protein maturation and degradation only.

We determine the maturation and degradation constants of both proteins in single-cell translation inhibition experiments. The translation blockade is induced following initial mRNA transfection by cell incubation in media containing cycloheximide, the translation blocking agent. Media exchange is done during the first hours of protein expression. As a result, the following changes in fluorescent protein numbers reflects the kinetics of the

protein maturation and degradation. The number of mature fluorescent proteins initially increases due to excess of translated, non-mature proteins that mature over time and enter

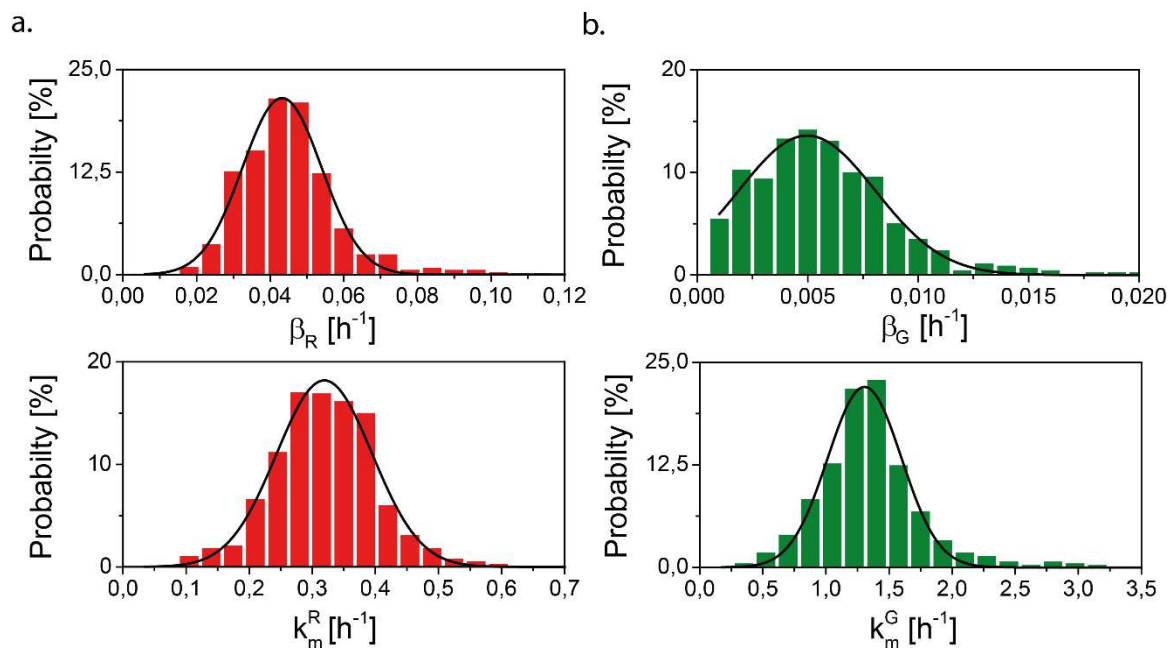


Fig.3.23. Population distributions of the maturation (k_m) and degradation (β) rate constants for CayRFP and eGFP

Population distributions of the maturation (k_m) and degradation (β) rate constants for CayRFP (a) and eGFP (b). Black lines are given to guide the eye.

the fluorescent state (Fig.3.22.). Subsequent decrease is associated with protein degradation that dominates the kinetics at late time scales. Described changes are following the kinetics described by reduced set of differential equations eq. 2.46-2.47. that are presented together with the analytical solution (eq. 2.48.) in the experimental section. The same model is used in the case of both proteins. Fig.3.23. shows obtained distributions of protein maturation (k_m) and degradation (β) rate constants. The corresponding mean values and related standard deviations are presented in table Tab.3. Data converted into the maturation and degradation half-times are also given. eGFP and CayRFP show significant differences in both maturation and degradation kinetics. eGFP shows faster maturation (4-fold higher compared to CayRFP) and slower degradation (8-fold lower than CayRFP) compared to CayRFP. The measured mean values of both maturation and degradation kinetic rate constants are fixed during the analysis of single-cell mRNA expression time-courses.

Tab.3. Mean degradation (β) and maturation kinetic constants (k_m) (and related half-times τ_β and τ_m)

The mean degradation (β) and maturation kinetic constants (k_m) (and related half-times, τ_β and τ_m respectively), together with related standard deviations ($\sigma_{\bar{x}}$), determined from single-cell analysis.

	$\beta \pm \sigma_{\bar{\beta}} [h^{-1}]$	$\tau_\beta \pm \sigma_{\bar{\tau}_\beta} [h]$	$k_m \pm \sigma_{\bar{k}_m} [h^{-1}]$	$\tau_m \pm \sigma_{\bar{\tau}_m} [h]$
<i>eGFP</i>	$(5,22 \pm 3,27) \cdot 10^{-3}$	$132,8 \pm 92,2$	$1,26 \pm 0,48$	$0,54 \pm 0,21$
<i>CayRFP</i>	$(4,21 \pm 1,32) \cdot 10^{-2}$	$16,45 \pm 0,18$	$0,30 \pm 0,08$	$2,29 \pm 0,63$

3.2.5. Correlation analysis

By fixing the protein maturation (k_m) and degradation (β) rate constants, we can determine the remaining kinetic parameters in a robust, unbiased manner. The analysis yielded the population distributions of I) initial translation rates, expressed as a product of initial mRNA molecule numbers and translation rate constant II) times of expression onset and III) the mRNA degradation rate constants. The parameters describing single-cell eGFP and CayRFP expression kinetics are obtained from both, siRNA-treated and control cells. Scatter plots (Fig.3.24 and 3.25) present values of parameters obtained from single-cell fits. Each point corresponds to the values obtained from one cell. In the following, we analyse the correlations observed between the expression parameters of both proteins. We demonstrate that, of the fitted parameters, the initial translation rates (mok_{it}) and expression onset times (t_0) are only moderately affected by siRNA activity, while the mRNA degradation rate constants exhibit a clear siRNA-mediated increase.

For both the initial translation rates mok_{it} and the expression onset times t_0 we expect strong correlation between eGFP and CayRFP reporters. This is because, according to our hypothesis, both mRNA^G and mRNA^R constructs are co-delivered in equimolar ratio and should have the same fate in each individual cell. The values of initial translation rates (mok_{it}) and expression onset times (t_0) are indeed strongly correlated between eGFP and CayRFP reporters (Fig.3.24.). The slopes of the main axis of the t_0 clusters for control cells were determined by linear fits. In contrast, the log-transformed mok_{it} values of control cells were fitted to a linear function with slope 1 and intercept a. Since a log-log linear fit is equivalent to a power-law fit, we interpreted the logarithm of the intercept as the linear slope of mok_{it} . In both cases the slopes in the eGFP vs. CayRFP plots are close to 1 ($0,98 \pm$

0,01 for Huh-7 and $1,05 \pm 0,01$ for A549 in case of t_0 ; $1,15 \pm 0,02$ for Huh-7 and $1,13 \pm 0,07$ for A549 in case of m_0k_{tl} . The corresponding Pearson correlation coefficients (PCC) values of the log-transformed m_0k_{tl} correlations are 0,89 ($p < 0,0001$) and 0,71 ($p < 0,0001$) for Huh-7 and A549 control cells respectively. Similarly, correlations between t_0 (eGFP vs. CayRFP) are described by PCCs of 0,9 ($p < 0,0001$) and 0,85 ($p < 0,0001$) for Huh-7 and A549 control cells respectively. Provided, that both mRNA and mRNA constructs are co-delivered in equimolar amounts, the translation rate constant is found to be in average 15% and 13% higher than CayRFP for Huh-7 and A549 control cells respectively.

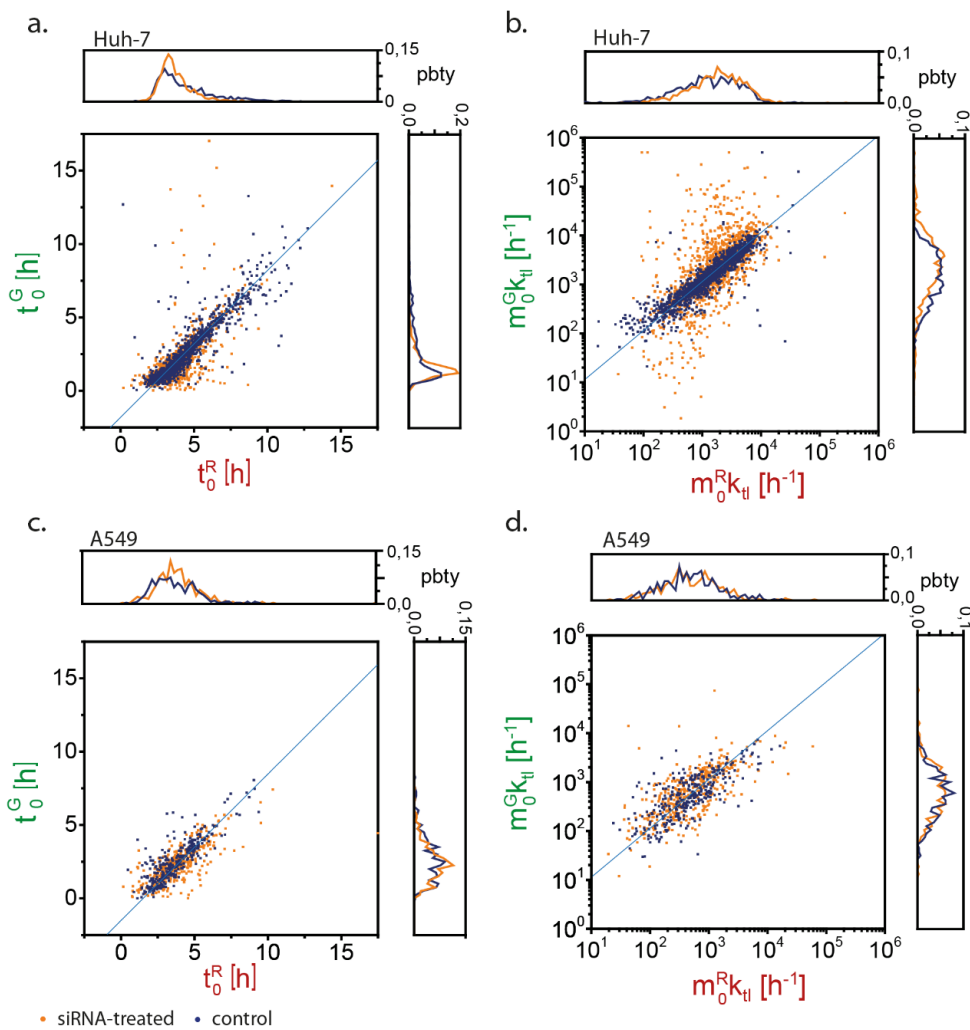


Fig.3.24. Single-cell correlations between parameters obtained from eGFP and CayRFP time-courses (m_0k_{tl} and t_0)

(a) The expression onset times (t_0) and (b) initial translation rate (m_0k_{tl}) obtained with Huh-7 cells. (c) and (d) show the corresponding data obtained with A549 cells (Orange: siRNA-treated cells, blue: control). The light blue lines represent linear fits to the control data. Fits to the scattered m_0k_{tl} data are performed after logarithmic transformation of determined values. The fits revealed the correlation slopes of approximately 1 in case of both t_0 and m_0k_{tl} . The average onset time of CayRFP is delayed in reference to eGFP.

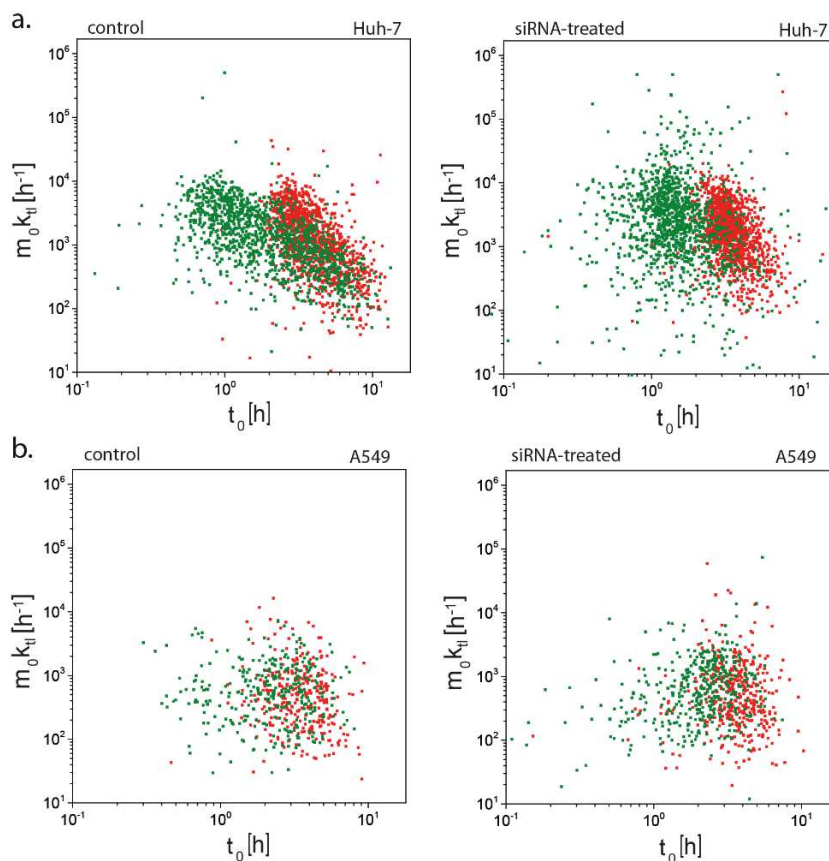


Fig.3.25. Correlation dot-plots of expression onset times t_0 and initial translation rate $m_0 k_{tl}$ ($m_0 k_{tl}$ vs. t_0)

The correlation dot-plots of expression onset times t_0 and initial translation rate $m_0 k_{tl}$ obtained of the same protein for (a) Huh-7 and (b) A549 cells with both siRNA-treated and control cell populations (green – eGFP, red – CayRFP). The particularly strong negative correlation is seen for control population of Huh-7 cells (a). (The Pearson correlation coefficients revealed values of $PCC = -0,34$ ($p < 0,0001$) and $PCC = -0,13$ ($p < 0,0001$) for CayRFP and eGFP respectively in Huh-7 siRNA-treated; $PCC = -0,47$ ($p < 0,0001$) and $PCC = -0,63$ ($p < 0,0001$) for CayRFP and eGFP respectively in Huh-7 control; $PCC = -0,18$ ($p = 0,0008$) and $PCC = -0,003$ ($p = 0,48$) for CayRFP and eGFP respectively in Huh-7 siRNA-treated; $PCC = -0,03$ ($p = 0,27$) and $PCC = -0,29$ ($p < 0,0001$) for CayRFP and eGFP respectively in Huh-7 control).

Both, The $m_0 k_{tl}$ and t_0 correlations are weakened upon siRNA treatment of cells ($PCC = 0,56$ ($p < 0,0001$) and $0,64$ ($p < 0,0001$) for Huh-7 and A549 cells respectively in case of $m_0 k_{tl}$ and $PCC = 0,58$ ($p < 0,0001$) and $0,75$ ($p < 0,0001$) for Huh-7 and A549 in case of t_0). siRNA treatment results also in a shift towards higher $m_0 k_{tl}$ values and shortening of the expression onset times t_0 of both proteins when values are compared to control cell results. Weakening of $m_0 k_{tl}$ correlation might be associated with the ribosome blocking activity of RISC complex.^{204–206} The shift towards shorter onset times might reflect the long-term effects of RISC activity. Here, the small amounts of late-released mRNA molecules are quickly degraded preventing the transfected cells from expressing

the targeted proteins. This claim is strengthened by the negative correlations observed between the number of released mRNA molecules (estimated using $m_{ok_{it}}$) and the expression onset times t_0 obtained for the same protein (Fig.3.25.). This observation indicates the existence of "temporal window of opportunity" for endosomal escape, the effect in which the efficient protein expression is achieved only when the transported nucleic acids are released from transfection complexes before being degraded in late endosomes.^{207,208} Additionally, we find a significant delay between the average onset times of eGFP (t_0^G) and CayRFP (t_0^R) expression (delay of 1,81 h and 1,53 h for Huh-7 and A549 control cells respectively and 1,83 h and 1,2 h for siRNA-treated Huh-7 and A549 cells respectively, quantified using the difference between population averages of both parameters). The delay is in accordance with observed difference in maturation time and translation rate constants between both proteins discussed previously.

Next, we discuss the mRNA degradation rate constants (δ), which exhibit the most profound changes upon siRNA treatment. The control cell data show significant correlation (PCC = 0,53 (p < 0,0001) for Huh-7 and PCC = 0,56 (p < 0,0001) for A549) between single-cell values describing eGFP- and CayRFP-mRNA degradation (δ^R and δ^G respectively). Data represented in double-logarithmic scale are presented in Fig.3.26. in orange and blue for siRNA-treated and control cells respectively. The degradation rate constants obtained for control cells are distributed over one order of magnitude in the case of both eGFP- and CayRFP-mRNA degradation constants. Here, the slope of the main axis of scattered distributions is given by the values of 0,46 and 0,36 for Huh-7 and A549 cells. We determine the slope by linear fit to log-transformed data. Notably, a slope of less than one indicates that the relation between δ^R and δ^G falls beyond linear proportionality and cannot be explained by assuming that a single enzyme is acting on both mRNA constructs with different affinities. Although, a simple model that incorporates two independent decay pathways, *i.e.* a minimum of two enzymes contributing, suffices to reproduce the observed slope as presented in further sections. We suspect that the differences between δ^R and δ^G might reflect the differences in codon usage in the eGFP and CayRFP coding sequences (Fig.3.27.).²⁰⁹⁻²¹²

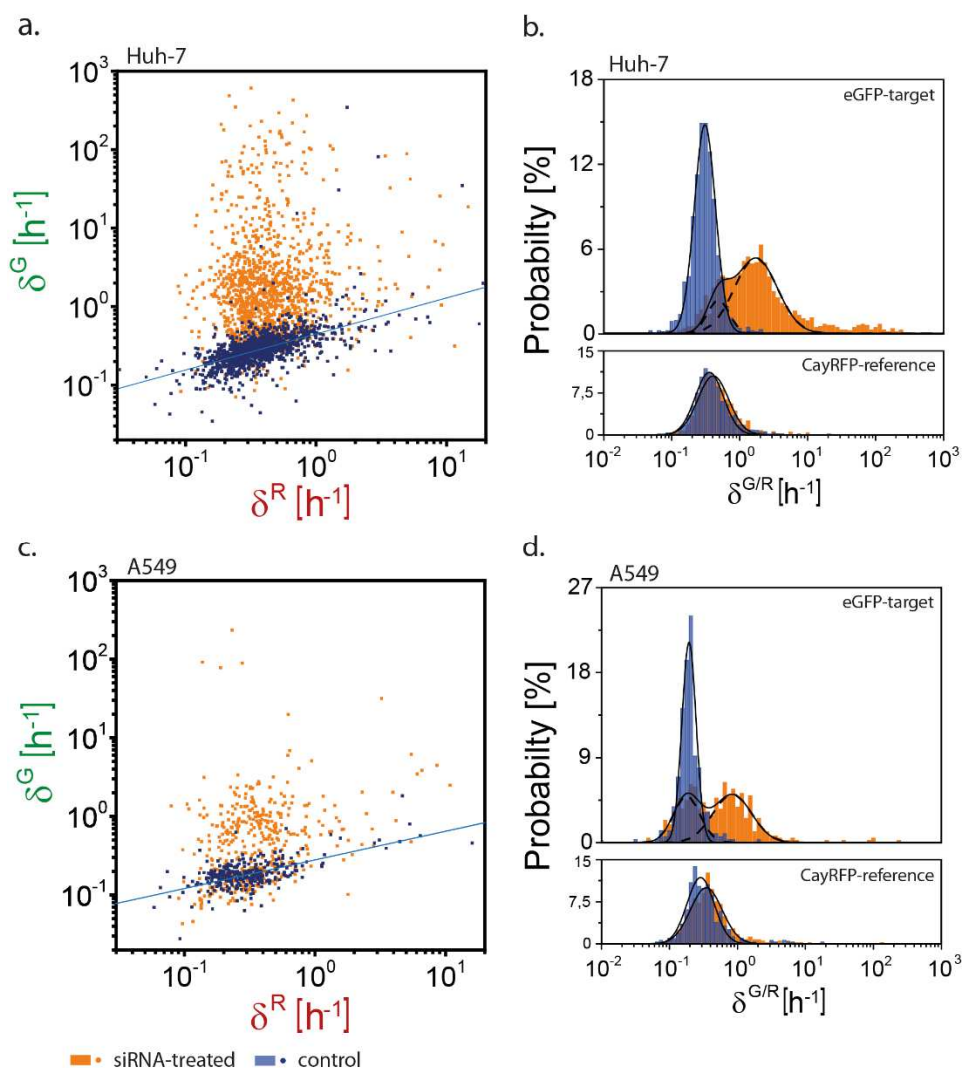


Fig.3.26. Correlation analysis of mRNA degradation constants (δ)

Values of single-cell degradation constants of $mRNA^G$ and $mRNA^R$ are plotted (a, Huh-7 cells; c, A549 cells). The slopes of correlations of control cell data reflect non-linear relationship between $mRNA^G$ and $mRNA^R$ degradation constants (slope determined by linear fit to log-transformed data, $\log(\delta^G) = 0.46 \cdot \log(\delta^R) - 0.35$ for Huh-7 cells, $\log(\delta^G) = 0.36 \cdot \log(\delta^R) - 0.55$). The scattered clusters of values obtained with siRNA-treated cells of both cell lines (a and c) reveal significant shifts towards higher δ^G values. δ^G values range over three orders of magnitude. The same distributions reveal the existence of two subpopulations characterized by high and low degradation constants (b and d, top). The subpopulation with low values shows a broad overlap with the distribution of control cells. A small shift towards higher degradation constants is also seen in δ^R (b and d, bottom). The positions of peaks related with two subpopulations present within siRNA-treated cell population are determined from log-normal fits (black, solid and dashed lines).

In the context of the goal of our work, however, the most important finding is that we observe a significant shift in eGFP-mRNA degradation rate constants (δ^G) towards higher values for siRNA-treated cells in both cell lines. A profound broadening of the corresponding δ^G distribution is observed. This spread of the values reaches three and two

orders of magnitude for Huh-7 and A549 cells respectively. Consequently, the distribution broadening results in weaker correlations between δ^G and δ^R (PCC = 0,09 ($p < 0,0001$) for Huh-7 and PCC = 0,27 ($p < 0,0001$) for A549). In addition, the δ^G distributions obtained from siRNA-treated cells reveals the existence of two cell subpopulations that present high and low values of mRNA degradation constants respectively. The latter subpopulation overlaps with the distribution derived from the control sample, and therefore might be attributed to the cells that either have not been successfully transfected with siRNA or do not respond to siRNA due to other factors. This effect is present in both cell lines, although it is more pronounced in A549 cells. Both the loss of correlation and the existence of cell subpopulations that have escaped siRNA transfection are most likely due to the stochastic nature of cellular uptake and endosomal release of siRNA complexes, which are independent of the mRNA degradation processes.

Tab.4. mRNA degradation rate constants δ (and related half-times τ_δ)

The medians of mRNA degradation rate constants δ (and related half-times τ_δ), together with standard errors ($\sigma_{\bar{x}}$), as determined from log-normal fits to single-cell distributions. Presented data are obtained with Huh-7 and A549 cells, for both target and reference mRNA constructs (eGFP and CayRFP respectively) and in both experimental conditions. ^a and ^b denote the values of the transfected and non-transfected subpopulations present among siRNA-treated cells respectively.

	Control		siRNA-treated		Relative change
	$\delta \pm \sigma_{\bar{\delta}} [h^{-1}]$	$\tau_\delta \pm \sigma_{\tau_\delta} [h]$	$\delta \pm \sigma_{\bar{\delta}} [h^{-1}]$	$\tau_\delta \pm \sigma_{\tau_\delta} [h]$	
Huh-7					
eGFP	$(34,5 \pm 0,2) \cdot 10^{-2}$	$2,01 \pm 0,01$	^a $(291,0 \pm 9,5) \cdot 10^{-2}$ ^b $(55,1 \pm 4,3) \cdot 10^{-2}$	$0,24 \pm 0,01$ $1,26 \pm 0,10$	$8,4 \pm 0,3$ - fold
CayRFP	$(45,1 \pm 0,6) \cdot 10^{-2}$	$1,54 \pm 0,02$	$(53,7 \pm 0,9) \cdot 10^{-2}$	$1,29 \pm 0,02$	$1,19 \pm 0,03$ - fold
A549					
eGFP	$(20,1 \pm 0,2) \cdot 10^{-2}$	$3,45 \pm 0,03$	^a $(128,5 \pm 7,6) \cdot 10^{-2}$ ^b $(22,0 \pm 1,8) \cdot 10^{-2}$	$0,54 \pm 0,03$ $3,16 \pm 0,26$	$6,4 \pm 0,4$ - fold
CayRFP	$(35,4 \pm 0,6) \cdot 10^{-2}$	$1,96 \pm 0,04$	$(46,5 \pm 1,0) \cdot 10^{-2}$	$1,49 \pm 0,03$	$1,31 \pm 0,04$ - fold

Finally, we determine the silencing efficiency as fold-change in mRNA degradation constants that arise upon siRNA activity. The distributions of siRNA-treated and control cell populations are analysed using log-normal fits to the experimental data. Two log-normal distributions are used to account for two subpopulations existing in siRNA-treated sample. Shifts between positions of the dominant subpopulation of siRNA-treated cells and the control cells serve as a measure of silencing efficiency. The corresponding relative changes in the median of the mRNA degradation constants between those two distributions reveal $8,4 \pm 0,3$ – fold for Huh-7 and $6,4 \pm 0,4$ – fold increase in δ^G for A549 cells. The accuracy of determined values reaches 3,3% and 6% as quantified using relative error for Huh-7 and A549 cells respectively. The method eliminates also the bias introduced by the presence of cells that have not been successfully transfected with siRNA in the siRNA-treated population. Additionally, a small shift towards higher values is also seen in case of δ^R ($1,19 \pm 0,03$ – fold and $1,31 \pm 0,04$ – fold increase for Huh-7 and A549 cells respectively) that might be related with the unspecific activity of siRNA or other side effects.^{201, 202} The degradation rate constants (δ) obtained from all log-normal fits and related mRNA half times ($\tau\delta$) are presented together with corresponding standard errors in Tab.4.

3.2.6. Codon optimality of eGFP- and CayRFP-mRNA constructs

We attribute the difference in degradation rates observed between CayRFP- and eGFP-mRNA to the significant differences in codon optimality within those two gene constructs (Fig.3.27.). Recently codon optimality has been found to be one of the determinants of mRNA stability. Although, up to now the underlying processes related with codon-optimality-dependent mRNA degradation are under dispute.^{209–211, 213} The relative abundance of the tRNA that recognizes given codons was causally linked with codon optimality defined by their translational efficiency. Codons related with the tRNAs of low abundance are translated less efficiently, which correlates with decreased mRNA stability. The causality of observed correlations was demonstrated by substitutions of optimal codons with synonymous codons of lower optimality in stable endogenous mRNA and *vice versa*. Described substitutions result respectively in a relative decrease and increase in mRNA stability.^{209–211, 213, 214} Arguably, the mRNA stability is affected, at least in part, by the speed of translation elongation since it was shown that the process of cognate tRNA recognition influences translation during elongation phase of the process.²¹⁵ Although, the tight link

with common mRNA surveillance pathways is not found and the deadenylation and decapping mRNA degradation processes might play a crucial role in the increase of decay rates.^{209, 211} Evidence of Dhh1 RNA-dependent ATPase activity in the context of ribosome movement and reduced mRNA stability related with decapping was recently found.²¹³

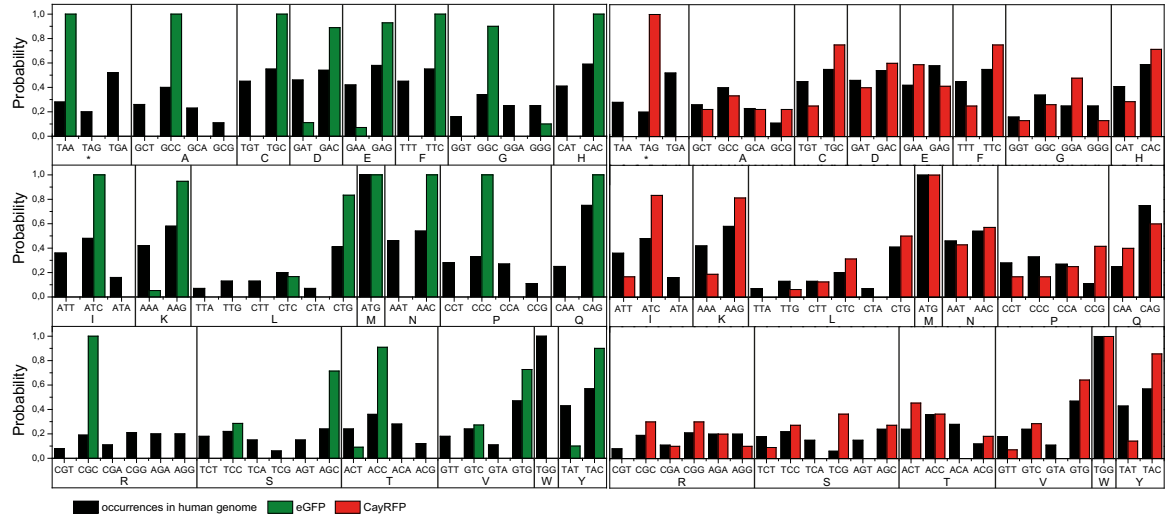


Fig.3.27. Occurrences of codons encoding different amino acids as found in used eGFP and CayRFP coding sequences

The occurrences of codons encoding different amino acids as found in used eGFP (green) and CayRFP (red) coding sequences compared to natural occurrence frequency in human genome (black) (represented as occurrence probability). CayRFP gene shows similar frequency of codon occurrences when compared with human genome. The eGFP coding sequence is optimized for maximizing expression efficiency in human cells as the most of silent base changes in the coding sequence favors the human codon-usage preferences.

We propose a simplistic enzymatic model, that qualitatively and quantitatively explains the distribution and inclination of scattered clusters of mRNA degradation rate constants (Fig.3.28.). Assuming, that at least two enzymes (RNaze “X” and RNaze “Y”) following Michaelis-Menten kinetics are degrading mRNA^G and mRNA^R, one can derive the effective degradation constants of both mRNA constructs as:

$$\delta = \frac{V_{max}^x}{K_m^x + [mRNA]} + \frac{V_{max}^y}{K_m^y + [mRNA]} \quad (\text{eq. 3.3.})$$

where: $[mRNA]$ denotes mRNA concentration, $V_{max}^{x/y}$ -maximum reaction rate of both enzymes, $K_m^{x/y}$ – Michaelis constant of both enzymes. Notably, the mRNA lipoplexes are formed with equimolar amounts of both CayRFP- and eGFP-mRNA. In this case, the concentration of both released mRNA constructs is roughly equal, $[mRNA^G] \approx [mRNA^R]$. Further assumption holds that only one enzyme (RNaze “Y”) shows increased catalytic activity while degrading CayRFP-mRNA. Since the details on the regulation mechanism

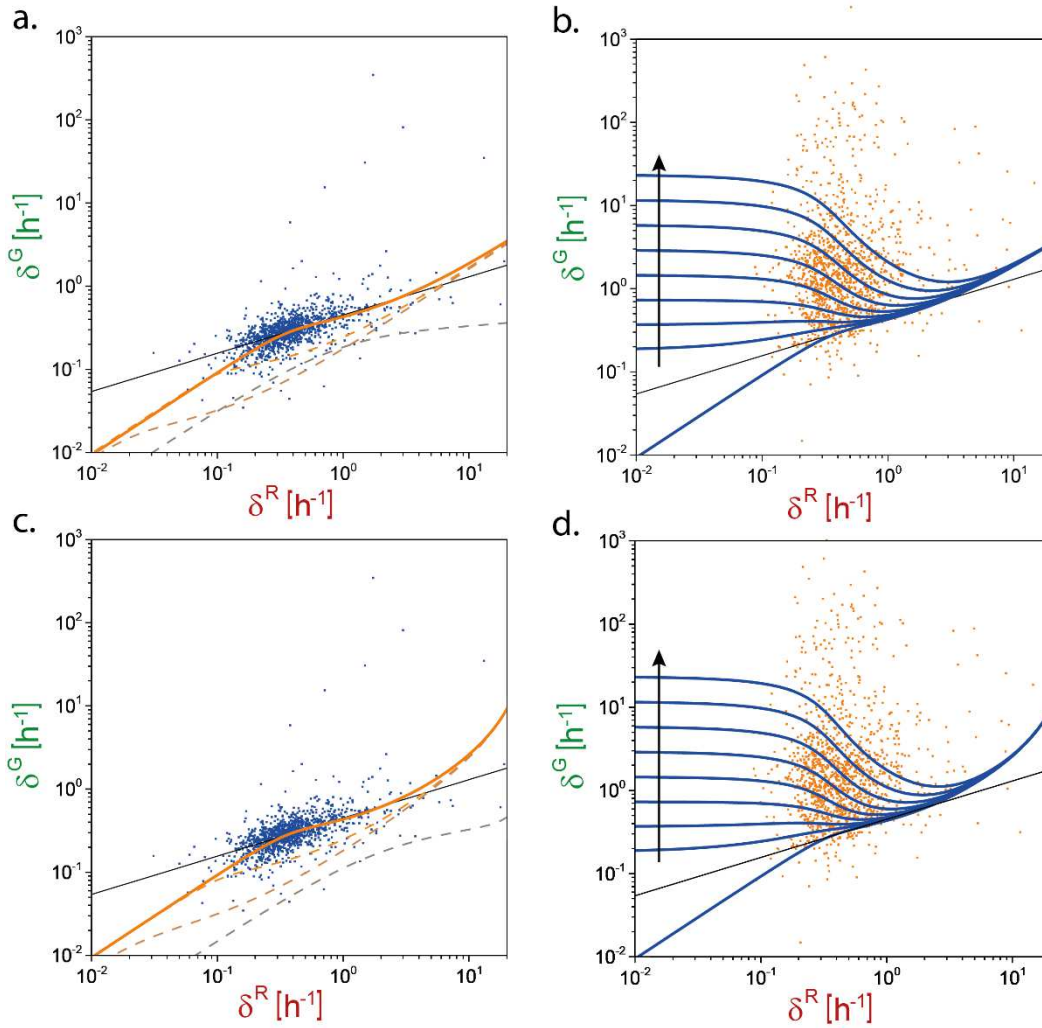


Fig.3.28. Calculated dependence between CayRFP- and eGFP-mRNA degradation constants (δ^G vs. δ^R) overlaid with experimental data

The non-competitive (a and b) and uncompetitive (c and d) allosteric regulation are considered. a,c) The calculations done for model of two enzymes degrading both mRNA constructs overlaid with scatter cloud of control Huh-7 cells (blue squares). Orange solid line shows the best agreement with the data and is obtained for $V_{max}^X = 5$ [nM h⁻¹], $K_m^X = 15$ [nM], $V_{max}^Y = 2,8 \cdot 10^{-2}$ [nM h⁻¹], $K_m^Y = 1 \cdot 10^{-3}$ [nM], $\alpha' = 12,5$. The dashed lines represent the traces obtained for following sets of parameters (from most grey to most orange):

$$V_{max}^X = 5$$
 [nM h⁻¹], $K_m^X = 15$ [nM], $V_{max}^Y = 2,8 \cdot 10^{-2}$ [nM h⁻¹], $K_m^Y = 1 \cdot 10^{-3}$ [nM], $\alpha' = 1000$;
 $V_{max}^X = 1$ [nM h⁻¹], $K_m^X = 50$ [nM], $V_{max}^Y = 2,8 \cdot 10^{-2}$ [nM h⁻¹], $K_m^Y = 1 \cdot 10^{-3}$ [nM], $\alpha' = 12,5$;
 $V_{max}^X = 5$ [nM h⁻¹], $K_m^X = 50$ [nM], $V_{max}^Y = 2,8 \cdot 10^{-2}$ [nM h⁻¹], $K_m^Y = 1 \cdot 10^{-3}$ [nM], $\alpha' = 12,5$.

B,d) The blue lines represent the traces obtained when additional mRNA^G degradation by RISC is taken into account ($k_{cat}^{RISC} = 25,56$ [h⁻¹], $K_m^{RISC} = 8,4$ [nM]). Change in shape of blue lines represents the increasing concentration of siRNA-loaded RISC proportional to the amount of mRNA taken up by cells (proportionality parameter equals 0; 0,05; 0,1; 0,2; 0,4; 0,8; 1,6; 3,2 and 6,4. Arrow indicates increase). Lines are overlying well with the experimental data obtained for siRNA-treated Huh-7 cells. Black line on a and b is determined as a linear regression to data obtained for control population of Huh-7 cells ($\log(\delta^G) = 0,46 \cdot \log(\delta^R) - 0,35$).

of codon-dependent mRNA degradation are still under dispute, the general scenarios of allosteric regulation are considered. The inhibitor/activator-related allosteric regulation might occur within two underlying scenarios. Firstly, the regulator can bind to the enzyme only when a substrate is incorporated within the enzymatic complex (*e.g.* uncompetitive inhibition). Secondly, the regulator can bind to the enzyme independently of substrate incorporation (*e.g.* non-competitive inhibition). Both scenarios relate to different changes in kinetic parameters of the modulated enzyme. The non-competitive inhibition affects only the maximal reaction rate V_{app}^{max} , which scales with the concentration of the modulator.

$$V_{max}^{y,CayRFP} = \alpha' V_{max}^{y,eGFP} = \alpha' V_{max}^y \quad (\text{eq. 3.4.})$$

where, α' is the proportionality parameter. On the other hand, uncompetitive inhibition leads to concurrent changes in the Michaelis constant (K_m^y) and maximal reaction rate (V_{max}^y), that keep the K_m^y/V_{max}^y ratio constant.

$$K_m^{y,CayRFP} = \frac{K_m^{y,eGFP}}{\alpha'} = \frac{K_m^y}{\alpha'}; V_{max}^{y,CayRFP} = \alpha' V_{max}^{y,eGFP} = \alpha' V_{max}^y \quad (\text{eq. 3.5.})$$

Depending on the choice of kinetic parameter values the relation eq. 3.4. and eq. 3.5. lead to the $\delta^G(\delta^R)$ dependence as shown on Fig.3.28a. and Fig.3.28c. respectively. The characteristic slope seen in case of control cell population could be reproduced as an effect of different enzyme activity in case of both regulation mechanisms considered.

Further, we introduce the RISC as additional enzymatic factor of siRNA-related degradation in case of eGFP-mRNA. Here, the amounts of siRNA taken up by each cell, thus the concentration of siRNA-loaded RISC, is assumed proportional to released mRNA and depends on endocytic activity of each cell. In this case, the eGFP-mRNA degradation constant is given by:

$$\delta^G = \frac{V_{max}^x}{K_m^x + [mRNA^G]} + \frac{V_{max}^y}{K_m^y + [mRNA^G]} + \frac{k_{cat}^{RISC} [RISC_{siRNA}]}{K_m^{RISC} + [mRNA^G]} \quad (\text{eq. 3.6.})$$

Here, $k_{cat}^{RISC} = 25,56 \text{ [h}^{-1}] = 7,1 * 10^{-3} \text{ [s}^{-1}]$ – RISC turnover number, $K_m^{RISC} = 8,4 \text{ [nM]}$ – RISC Michaelis constant [*in vitro* data]²⁰⁵, $[RISC_{siRNA}]$ – concentration of siRNA-loaded RISC. When one also considers the siRNA-dependent degradation the characteristic shape of scatter cloud density is reproduced (Fig.3.28).

The maximum reaction rates and Michaelis constants estimated here ($(V_{max}^X = 5 \text{ nM h}^{-1}$, $K_m^X = 15 \text{ nM}$, $V_{max}^Y = 2,8 * 10^{-3} \text{ nM h}^{-1}$, $K_m^Y = 1 * 10^{-3} \text{ nM}$) are varying significantly

(orders of magnitude) from the literature values obtained for most common RNases measured *in vitro*.^{216–219} This effect might relate with significantly different reaction conditions within the cells, associated with molecular crowding, low numbers of enzymes or extended network of regulatory pathways. Although, all numbers presented here need to be treated as rough estimations.

4. Conclusions.

In the first part of the work, we have presented a microfluidic-based method for the synthesis of monomolecular nucleic acid/lipid particles, mNALPs. We have demonstrated that by rational design of lipid composition, combined with microfluidic mixing by hydrodynamic focusing we have improved the control over particle assembly process. Gained control over mixing times allowed us to enhance the physicochemical properties of particles such that the majority contain on average a single 21 bp dsDNA or siRNA covered with single, highly curved and PEG-grafted lipid bilayer. The synthesis is robust, reproducible and yields particles of superior colloidal properties when compared to the product of standard macroscopic mixing by vortexing.

In particular, particles show narrower size distribution, minimized numbers of unwanted aggregates and a 20% higher efficiency of NA encapsulation. Further reduction of solvent mixing times using surface acoustic waves did not have a significant effect on particle properties.²²⁰ Importantly, the prospect of robust continuous-flow synthesis allows for automation and scaling up the production yield without losses in sample quality by parallelization of the process. It was shown in previous studies that the reduced size of delivery agents (below 50 nm in diameter) enhances the efficiency of *in vivo* delivery into solid tumours and improves the bio-distribution of nanoparticles in general.^{64, 65} In this context, small and monodisperse mNALPs, that reach the minimal size limit of lipid-bilayer-coated siRNA nanoparticles, could be an important system for possible medical applications in treatment of solid tumours.

The functionalization of mNALPs with folate (FolA-mNALPs) resulted in specific binding and uptake by folate-receptor-overexpressing KB cells. The differential confocal microscopy studies presented indicate that uptake is related with receptor-mediated endocytosis. Kinetic studies using flow cytometry indicated that particles are efficiently internalised within 20 min of cell incubation. In the same time, surface passivation by PEG-

grafting of particle surface minimises the receptor-unrelated uptake and results in high specificity of targeting. Moreover, Fola-mNALPs present high stability in biological fluids (blood serum and plasma) has the potential to increase the lifetime of particles following *in vivo* systemic administration. Fola-mNALPs do not lose their properties up to 24 days of storage at room temperature.

Despite the efficient cellular internalization, mNALPs are not capable of successful escape from endosomes as revealed by nanoparticle/endosome co-localization observed during confocal imaging. This effect might be related with thorough PEG-shielding that prevents particles from destabilisation of endosome membrane.²²¹ However, the efficient gene silencing was triggered when KB/eGFPLuc cells expressing eGFPLuc reporter protein were subjected for treatment with endosomolytic agent - chloroquine. The finding indicates that the particles are capable of releasing the functional siRNA into the cytoplasm after facilitated endosomal release. Thus, the further development of mNALP system would need to involve additional release mechanism *e.g.* pH-dependent particle destabilisation or endosome membrane disruption.

The small size, reproducible and efficient synthesis using a microfluidic platform, selective targeting and achieved silencing after facilitated endosomal release presents high promise for further development of mNALPs directed at potent *in vivo* siRNA delivery into solid tumours.

The second part of the work presents a method for quantifying silencing efficiency of siRNA by changes in absolute parameters describing the single-cell-level kinetics of mRNA degradation. Data were collected using live-cell imaging on single-cell arrays (LISCA). We determined the kinetic parameters of mRNA decay by the mathematical modelling of protein expression following mRNA transfection. The expression was modulated by additional siRNA delivery. Moreover, in analogous experiments based on pDNA delivery, we explored the limits of standard silencing efficiency analysis based on changes in fluorescence intensity of reporter proteins. Using a dual-reporter assays, we compared the changes observed between siRNA-targeted eGFP reporter and the internal reference of CayRFP.

Firstly, the outcome of commonly used fluorescence intensity analysis showed significant quantitative differences between single-cell-level and population-averaged data. The observed effect could be associated with cellular heterogeneity, effects of which are

averaged during population level analysis.^{122,159} The extrinsic noise contribution to heterogeneity in cellular responses, however, could be limited when the signal was normalized by internal expression reference. Additionally, the relative fluorescence used as a measure for silencing efficiency is strongly dependent on the selected time point of the measurement in the cases of both, single-cell- and population-level of analysis.

Secondly, we performed the analysis of full kinetic changes in expressed protein numbers following mRNA transfection to access the mRNA degradation rate constants. Importantly, the shift in those values can serve as a time-independent measure for silencing efficiency. Use of mRNA delivery reduces the complexity of the molecular network of protein expression. It allows for limiting of the mathematical model to ordinary differential equations describing translation, protein maturation and degradation of both mRNA and protein as first order mass action kinetics. To further reduce the number of free parameters within the model, and to improve the robustness of the fitting procedure, we determined the protein degradation (β) and maturation (k_m) rate constants independently. The remaining parameters describing protein expression, namely initial translation rates (mok_{it}), times of expression onset (t_0) and mRNA degradation rate constants (δ), were determined by least-squares fits of the mathematical model to experimental data yielding the population distributions of single-cell values.

Notably, the single-cell parameters disclosed correlations, which provided valuable insight into the mRNA delivery and siRNA-induced silencing. We observed a strong correlation between the eGFP and CayRFP initial translation rates (mok_{it}) as well as the expression onset times (t_0) suggesting that in average equimolar amounts of both mRNA constructs were released simultaneously into the cytoplasm of the cell. However, a systematic and yet unexplained shift between eGFP and CayRFP onset times was observed. This shift is in accordance with the observed longer maturation time of CayRFP compared to eGFP and with possibly higher translation rate of eGFP, yet none of those effects can explain it fully. Additionally, we observed that siRNA has a weak effect on translation, indicating that the RISC-associated blocking of ribosomes plays marginal role in the case of the investigated siRNA construct.

The most profound effect of siRNA treatment was observed as a clear increase in the mRNA degradation constants (δ) compared to control cells that was present in both Huh-7 and A549 cell lines. Here, the siRNA-related shift in the median of eGFP-mRNA

degradation constants distributions (\mathcal{G}) revealed $8,4 \pm 0,3$ – fold and $6,4 \pm 0,4$ – fold increase for both Huh-7 and A549 cells respectively. This relative increase represents a sensitive, time-independent measure of the silencing efficiency. In addition, small difference in the CayRFP-mRNA degradation constants (\mathcal{G}) was observed ($1,19 \pm 0.03$ -fold and $1,31 \pm 0.04$ -fold changes for Huh-7 and A549 cells respectively) reflecting weak nonspecific side effects of siRNA treatment.^{201, 202} Moreover, the distributions of eGFP-mRNA degradation constants revealed existence of two subpopulations of cells, related with high and low degradation rates. This feature served to identify subpopulations that are less susceptible to siRNA-based therapeutics under investigation and was accounted for during determination of relative changes in mRNA degradation constants. We also noted that codon optimality might explain the differences between degradation constants of eGFP- and CayRFP-mRNA constructs observed for control cells.

Taken together, the presented method LISCA provides direct access to the protein expression and mRNA delivery kinetics as well as efficiency of siRNA constructs. The assay is fast, accurate and provides the time independent measure for siRNA silencing efficiency. Moreover, the method gives access to absolute values of mRNA degradation rate constants that can, in general, be directly converted into single-cell mRNA half-lives. In particular, screening for functional optimality of siRNA sequences is one of the core determinants for improved silencing efficiency in siRNA-based therapy and RNAi screens.^{29,38} Moreover, in mRNA based therapy, the stability of artificial mRNAs and their translational efficiency are of high importance.^{165, 222, 223} As presented, LISCA method allows studies on single-cell gene expression and gene regulation kinetics, revealing insights beyond population-averaged analysis. The method may play important role in development of novel assays for molecular biology, pharmacy and systems biology.

Appendix.A1. Protocols

A1.1. Master micro-structures for stamp and micro-chip preparation

The stamp to prepare micro-patterns and micro-channels for the hydrodynamic focusing or fluorescence calibration micro-chip were created by curing PDMS on AZ 40XT and SU-8 master structure respectively. The master micro-structures themselves were prepared on a silicon wafer by UV-laser-based direct exposure using an AZ 40XT or SU-8 100 photoresist (MicroChem Corp., Westborough, MA, USA). AZ 40XT and SU-8 100

was processed in accordance with the manufacturer's instruction. The micro-structures were exposed using the LPKF ProtoLaser LDI. Pattern and channel designs were prepared using LPKF CAD/CAM software provided by LPKF Laser and Electronics. The master structures were silanized using trichloro(1H,1H,2H,2H-perfluorooctyl)silane in an evacuated exicator for 12 hours before further use. PDMS was cured on top of the master structures (crosslinker 10% (wt/wt), 50°C for 12h) forming the stamp or micro-channel.

A1.2. Fabrication of microfluidic chip devices

The microfluidic chip was made by covalently attaching a PDMS channel micro-structure to a glass cover using oxygen-plasma-induced bonding. Glass cover was cleaned by sonication in isopropanol and deionized water baths for 40 and 60 min respectively and dried under a nitrogen flow. The PDMS channel was cut and peeled from the master, placed in the plasma cleaner together with the cleaned glass cover and chemically activated by exposing them to oxygen plasma (Femto Diener plasma generator at 10 W power, 3 min exposure). PDMS and glass surfaces were brought into contact immediately after treatment, causing the creation of Si–O–Si bonds between them.

A1.3. Cell culture

Human hepatocellular carcinoma cells (Huh-7; I.A.Z., Munich, Germany), human lung carcinoma cells (A549; ATCC CCL-185), wild-type human cervix carcinoma KB cells (KB/WT; Leibniz Institute DSMZ-German Collection of Microorganisms and Cell Cultures GmbH, Braunschweig, Germany) and KB cells stably transfected with the enhanced green fluorescent protein/luciferase gene (KB/eGFPLuc) were used. Huh-7 cells were cultivated in RPMI-1640 GlutaMAX media (Gibco, Life Technologies GmbH, Darmstadt, Germany) supplemented with 10% (v/v) FBS, 2 mM sodium pyruvate and 5 mM HEPES (all from Life Technologies). A549 cells were cultivated in MEM media (C-C-pro, Oberdorla, Germany) supplemented with 10% (v/v) FBS and 2,5 mM L-glutamine (both from Life Technologies). KB cells were cultivated in folate-free Gibco RPMI-1640 supplemented with 10% (v/v) FBS (Life Technologies GmbH, Darmstadt, Germany). Additionally, the media for KB/eGFPLuc cell cultivation was supplemented with penicillin (100 U mL⁻¹) and streptomycin (100 µg mL⁻¹). All cell lines were grown at 37 °C in ventilated flasks in a humidified atmosphere containing 5% CO₂. The cells were passaged every 3–4 days after reaching 80% surface confluency. For long-term microscopy

experiments, Huh-7 and A549 cells were incubated in the absence of CO₂ in phenol-red-free L-15 medium supplemented with 10% FBS.

A1.4. mNALP assembly and activity

A1.4.1. Materials

Used lipids, namely DOTAP, 1,2-dioleoyl-3-trimethylammonium-propane (chloride salt); DOPE, 1,2-dioleoyl-sn-glycero-3-phos-phoethanolamine; DOPC, 1,2-di-(9Z-octadecenoyl)-sn-glycero-3-phosphocholine; DSPE-PEG(2000), 1,2-distearoyl-sn-glycero-3-phosphoethanolamine-N-[methoxy(polyethylene glycol)-2000] (ammonium salt) and DSPE-PEG(2000)-FolA, 1,2-distearoyl-sn-glycero-3-phosphoethanolamine-N-[folate(polyethylene glycol)-2000] (ammonium salt) were provided by Avanti Polar Lipids Inc., Alabaster, Ala., USA and used without further purification. Single-stranded DNA oligonucleotides (lyophilized, HPLC-purified), sense and antisense strand, were purchased from Eurofins Genomics (Ebersberg, Germany). For FCS experiments the 5'-end of sense strand was conjugated with Cy3 dye; Cy3-dsDNA. For flow cytometry and confocal microscopy the 5'-end of both strands was conjugated with ATTO488. Oligonucleotides were diluted in 30 mM HEPES-KOH, 100 mM KCl, 2 mM MgCl₂, 50mM NH₄Ac, pH 7,5 to a concentration of 100 μM and stored in -20 °C until further use. For gene-silencing studies, two siRNA duplexes (Axolabs GmbH Kulmbach, Germany) namely the GFP-targeted sequence siGFP and the control sequence siCtrl were used. Chloroquine (N4-(7-chloro-4-quinoliny)-N1,N1-dimethyl-1,4-pentanediamine diphosphate salt) and folate (folic acid) were purchased from Sigma-Aldrich (Munich,Germany).

A1.4.2. dsDNA and siRNA sequences

Cy3-dsDNA:

Sense strand: 5'-Cy3-CCAACAGTAAAAGGAATATCC-3'

Antisense strand: 5'-GGATATTCCTTTTACTGTTGG-3'

ATTO488-dsDNA:

Sense strand: 5'-ATTO488-CCAACAGTAAAAGGAATATCC-3'

Antisense strand: 5'- ATTO488-GGATATTCCTTTTACTGTTGG-3'

siGFP:

Sense strand: 5'-AuAucAuGGccGA cAAGcAdTsdT-3'

Antisense strand: 5'-UGCUUGUCGGCcAUGAuAU dTsdT-3'

siCtrl:

Sense strand: 5'-AuGuAuu GGccuGuAuuAGdTsdT-3'

Antisense strand: 5'-CuAAuAcAGGCcAAuAc AUdTsdT-3'

A1.4.3. Annealing of complementary oligonucleotides

In order to obtain double stranded Cy3-dsDNA and ATTO488-dsDNA duplexes the complementary single strands (sense and antisense strands) were annealed. Two strands in equimolar amounts (20 μ M:20 μ M; 120 ml) were incubated at 96 °C for 2 min and slowly cooled overnight at room temperature. The 21 bp dsDNA was then dialysed against 20 mM TRIS-HCl, 2 mM EDTA (2 \times TE, pH 8) buffer and stored in -20 °C until further use.

A1.4.4. Blood serum and blood plasma collection

Blood samples were collected from healthy volunteer donors and informed consent was obtained from all of them. S-monovette coagulation sodium citrate (Sarstedt, Germany) system was used for blood plasma extraction and an S-monovette serum clotting activator (Sarstedt, Germany) system for blood serum extraction. Samples were centrifuged (10 min, 2300 rpm). Subsequently, the supernatant was collected. Centrifugation was done immediately in the case of blood plasma, and after incubation at room temperature for 30 min in the case of blood serum. The blood plasma and serum supernatants were aliquoted and stored at -80 °C until further use. Each of 0,5 ml aliquotes were used once. Blood plasma/serum was thawed slowly at room temperature to avoid degradation or deactivation of plasma/serum components.

A1.4.5. Preparation of mNALP samples

Firstly, the required amounts of lipids dissolved in chloroform in the molar ratios 1 : 5 : 6 : 1,2 DOTAP : DOPE : DOPC : DSPE-PEG(2000) for non-targeted mNALPs, or 1 : 5 : 6 : 1 : 0,2 DOTAP : DOPE : DOPC : DSPE-PEG(2000) : DSPE-PEG(2000)-FolA for folate-targeted FolA-mNALPs, were mixed together in flat bottom glass vials, dried under a nitrogen flow and placed in a vacuum oven at room temperature for evaporation of chloroform residues. Lipids were then re-diluted in a mixture of isopropanol (UV/IR grade) and deionized water (60% (v/v) isopropanol/H₂O) to the final DOTAP concentration of 300 μ M. Obtained lipid stock solution was sonicated using tip sonicator before further use. Secondly, molecular solutions containing lipids and dsDNA/siRNA in 50% (v/v)

isopropanol/H₂O were prepared by gentle stirring. Importantly, this step can result in premature micro-precipitation of dsDNA/siRNA. For this reason, vigorous shaking, presence of multivalent cations (*e.g.* Mg²⁺) in the solution. Additionally, to avoid abrupt changes in lipid saturation that can also result in formation of precipitants, the following pipetting sequence should be adhered to: H₂O, isopropanol, lipid stock solution, dsDNA/siRNA stock in 2 × TE. Finally, Lipid/siRNA nanoparticles were synthesized using solvent exchange method, by ten-fold dilution of molecular solutions in deionized water. Dilution of molecular solutions was done by vortex mixing by hand or hydrodynamic focusing in a microfluidic chip. In the first case, 75 µL of molecular solution was added drop by drop into 675 µL of water in a 4 mL glass vial and gently vortexed. In the second case, dilution was accomplished by hydrodynamic focusing of the molecular solution with deionized water and diffusive mixing. Flow rates were maintained at the same continuous level of 0,1 and 0,9 mL h⁻¹ for molecular solution and water, respectively. Two TSE Systems syringe pumps (Model 540200) were used to control the flow rates. Subsequently, sample quality was investigated by fluorescence correlation spectroscopy (FCS). In addition, samples prepared by microfluidic mixing were used for stability, uptake and silencing experiments. Here, the samples were concentrated to the desired degree in an Eppendorf concentrator at 45 °C under high vacuum and re-diluted in cell culture medium, serum/PBS or plasma/PMS mixture. In this step, the residual isopropanol content is further reduced.

During stability experiments Fola-mNALPs were concentrated 10 times and re-diluted in biological fluids up to a starting concentration of Cy3-dsDNA. In the same time, final plasma and serum concentrations were kept in the ranges of 30 to 90% (v/v) and 10 to 80% (v/v) respectively for plasma and serum samples. To gain varying plasma/serum content biological fluids were mixed with PBS (pH 7,5) prior to addition of nanoparticles. Serum samples were stored at 21 °C in the dark. Plasma samples were kept at 4 °C to minimize sample coagulation. To investigate the shelf lifetime the non-diluted, non-concentrated sample was stored at 21 °C in the dark for up to 24 days.

A1.4.6. Cell binding and uptake experiments – Confocal Microscopy

The KB/WT cells (25 × 10⁴ cells per mL) were seeded on a µ-Slide VI0,4 ibiTreat (Ibidi, Munich, Germany) in folate-free RPMI-1640 medium (90 µL per channel) and incubated under standard cultivation conditions (see Cell culture section). An additional

batch of cells was grown in RPMI-1640 medium supplemented with 100 μ M folate for 7 days and kept under high Fola conditions during the experiment to block the receptor-mediated uptake. 24 hours after seeding, RPMI-1640 medium containing Fola-mNALPs (50 nM of ATTO488-dsDNA) and the lysosome-specific dye LysoTracker Red DND-99 (40 nM; Thermo Fisher Scientific) was placed on the cells and incubated for 50 min under standard growth conditions. Cells incubated with non-targeted mNALPs and uncoated 21 bp ATTO488-dsDNA were used as controls. After rinsing twice with PBS (pH 7,5) cells were re-incubated in Lebovitz's L-15 phenol-red-free CO₂-independent medium (Gibco) and imaging was performed.

A1.4.7. Cell binding and uptake experiments – Flow Cytometry

Wild-type KB/WT cells were seeded in 24-well plates in folate-free RPMI-1640 medium (400 μ L, 5×10^4 cells per well) and incubated under standard cultivation conditions (see Cell culture section). Flow cytometry experiments were performed 24 h after seeding.

During dose-dependent receptor binding and uptake studies, cells were incubated in folate-free RPMI-1640 medium (300 μ L) containing Fola-mNALPs (10–85 nM of ATTO488-dsDNA) for 50 min under standard culture conditions. Cells incubated with medium containing the same amount of non-targeted mNALPs and uncoated 21 bp dsDNA were used as negative controls. After rinsing twice with ice-cold PBS (pH 7,5) the cells were detached using PBS containing 10 mM EDTA (pH 7,5). Subsequently, the cells were re-suspended in ice-cold PBS, pelleted, re-suspended once again and stored on ice in 1,5 mL Eppendorf vials prior to FC analysis.

Time-dependent receptor binding and uptake studies were performed in the similar workflow. Cells were incubated with medium containing Fola-mNALPs (50 nM; ATTO488-dsDNA) for 7,5–37,5 min, depending on the sample batch. To differentiate between the nanoparticles bound to cell surface receptors and nanoparticles incorporated into cells, surface-bound Fola-mNALPs were detached by exposing the cells to low pH, which induces dissociation of folate from the folate receptor. For this purpose two additional washing steps (~10s each) with ice-cold acidified (pH 3,4) saline (10 mM sodium acetate, 150 mM NaCl + acetic acid) were performed before washing with PBS. The same negative controls were kept as in case of dose-dependent receptor binding and uptake studies used with according variations regarding incubation times.

A1.4.8. mNALP-induced silencing experiments – luciferase assay

KB/eGFPLuc cells were seeded in 96-well plates in folate-free RPMI-1640 medium (4×10^3 cells per well) and incubated under standard cultivation conditions (see Cell culture section). GFP-siRNA (siGFP) was used for silencing the expression of the eGFPLuc protein, and the randomized siRNA sequence (siCtrl) was used as the negative control. 24 h after seeding cells were incubated with cultivation medium containing Fola-mNALPs (50 nM of siGFP or siCtrl) diluted in culture medium (100 μ L) under standard cultivation conditions for 48 h. Cells incubated with medium containing the same amount of non-targeted mNALPs loaded with siGFP or siCtrl were used as negative controls. In a second set, experiments were performed as described above (including all mentioned controls) but in media supplemented with 100 μ M chloroquine. Both experimental sets were carried out in parallel, with the same seeding batch and nanoparticle samples. After the incubation medium was removed and 100 μ L of the lysis reagent (Promega, Mannheim, Germany) per well was added. Luciferase activity was evaluated using the luciferase assay kit (Promega, Mannheim, Germany). Fluorescence measurement was carried out using Centro LB 960 luminometer (Berthold, Bad Wildbad, Germany). Silencing efficiency was quantified as a relative light units (RLU; fluorescence intensity level divided the value obtained in untreated control cells and represented as percent).

A1.5. siRNA mediated mRNA degradation kinetics

A1.5.1. Surface patterning and microscopy slide preparation

Surface micro-patterns were prepared by selective oxygen plasma treatment (Femto Diener plasma generator at 40 W power, 3-min exposure) and passivation of activated surface areas of polymer coverslips (uncoated, Ibbi GmbH, Munich, Germany).^{169,170} Selectivity was achieved by using polydimethylsiloxane (PDMS) stamps (Fig.2.8.) as a mask. Activated surface areas were passivated by a 20-min incubation with a PLL(20k)-g(3,5)-PEG(2k) (SuSoS AG, Dübendorf, Switzerland) solution (1 mg mL⁻¹) in aqueous buffer (10 mM HEPES, 150 mM NaCl pH 7,4). Washed and dried coverslips were then glued to bottomless slides (6-channel sticky-Slide VI 0,4; Ibbi GmbH). The remaining, non-passivated areas (30 μ m \times 30 μ m squares) were then exposed for 1 h to fibronectin (50 μ g mL⁻¹; YO Proteins AB, Huddinge, Sweden), rendering these areas cell adherent. Each channel was then thoroughly rinsed with PBS and stored at 4 °C until further use.

A1.5.2. *In vitro* transcription

In vitro transcription was performed using pVAX-eGFP-A120 and pVAX-CayRFP-A120 plasmids (plasmid maps are given in Fig.A1.3.) as templates for the synthesis of eGFP (mRNA^G) and CayRFP mRNAs (mRNA^R) respectively. The CayRFP (Atum, Newark, CA, US) and eGFP (Clontech, CA, US) genes were cloned into the pVAX-A120 plasmid (kindly provided by Ethris GmbH, Planegg, Germany), which contains a T7 promoter region and a 120-bp poly-A tail. Plasmids were linearized by digestion with *NotI*, which cleaves the sequence located immediately downstream of the poly-A tail. The linearized and purified plasmids were used as templates for *in vitro* transcription performed using the MessageMAX T7 ARCA-Capped Message Transcription Kit (Biozym Scientific GmbH, Hessisch Oldendorf, Germany) in accordance with the kit manufacturer's protocol. One μg of plasmid was used to produce up to 2 μg of mRNA transcripts with an Anti-Reverse Cap Analog (ARCA) ($m_2^{7,3'}\text{-}^0\text{G}[5']\text{ppp}[5']\text{G}$) on the 5' end. mRNAs were purified by precipitation with ammonium acetate and ethanol. Purified mRNA products were diluted to a final concentration of 100 ng μl^{-1} in RNase-free water, divided into 10- μl aliquots and stored at -80 °C until further use.

A1.5.3. LISCA - silencing experiments

Huh-7 or A549 cells were grown on micro-patterned 6 channel sticky-Slide VI 0,4 (Ibidi, Munich, Germany). 1×10^4 cells were seeded in each channel 4h before experiment. The equimolar amounts of eGFP- and CayRFP-encoding pDNA or mRNA were used (total amount of 0,03pmol/channel and 0,38 pmol/channel in case of pDNA and mRNA respectively). pEGFP-N1 (pDNA^G; Clontech, CA, US) and fpb-55-609_CayenneRFP (pDNA^R; Atum, Newark, CA, US) plasmids were used (plasmid maps are given in Fig.A1.2.). mRNA was synthesized as described above. To prepare the transfection complexes 154,5 ng/179 ng of pDNA^G/pDNA^R or 152 ng/148 ng of mRNA^G/mRNA^R was diluted in OptiMEM transfection media (Gibco) to a total volume of 150 μL and incubated for 5 min in room temperature. Similarly, 0,8 μL (in case of pDNA) or 0,748 μL (in case of mRNA) of Lipofectamine (Life Technologies) was diluted in OptiMEM (Gibco) to a total volume of 150 μL . pDNA/mRNA and Lipofectamine solutions were mixed together by pipetting, followed by another 20 min incubation at room temperature for forming transfection complexes.

In case of pDNA transfection cells were washed twice with PBS and once with OptiMEM immediately before transfection. 90 mL of pDNA/Lipofectamine complexes was placed in each channel and incubated for 1h under standard cultivation conditions (see Cell culture section). Simultaneously, the siRNA/lipofectamine complexes were made. 75 pmol of GFP Duplex I siRNA (Dharmacon) was diluted in OptiMEM to a total volume of 150 mL and incubated for 5 min in room temperature. Similarly, 1,2 mL of Lipofectamine was diluted in OptiMEM (Gibco) to a total volume of 150 mL. siRNA and Lipofectamine solutions were mixed together by pipetting and then incubated at room temperature for 20 min for forming transfection complexes. Half of the cells transfected with pDNA were washed OptiMEM, each channel was filled with 90 mL of siRNA/lipofectamine complexes and incubated under standard cultivation conditions for another 30 min. As a positive control second half of cells transfected with pDNA were washed and incubated in culture medium for the same 30 min period. Subsequently, the transfection solution or culture medium were removed, all cells were washed twice with PBS and re-incubated in Leibovitz's L-15 CO₂-independent phenol-red-free media, 10% (v/v) FBS. Cells were imaged immediately after channels were sealed with anti-evaporation oil (Ibidi).

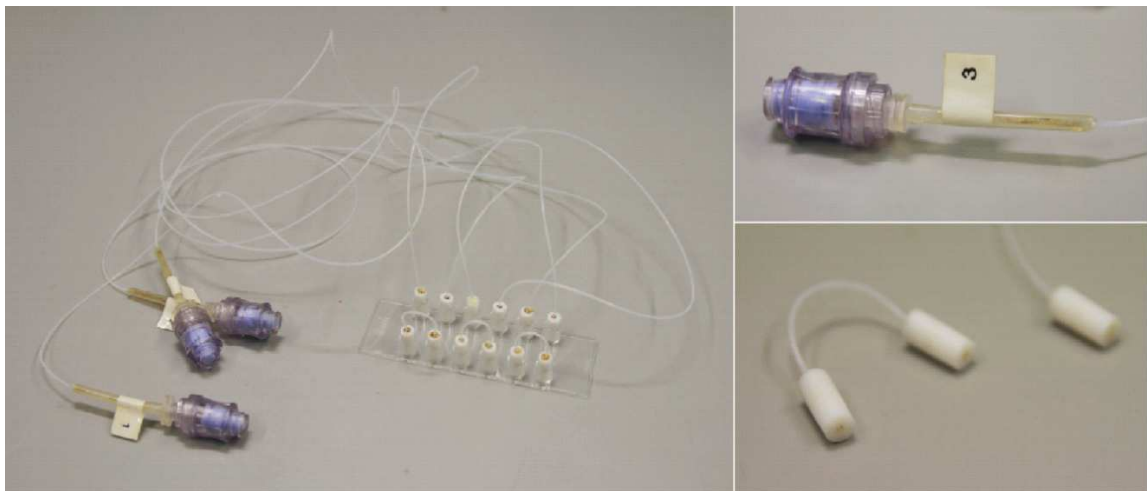


Fig.A1.1. Crafted system of tubing used to exchange the fluids inside the microscopy slide

Crafted system of tubing used to exchange the fluids inside the microscopy slide directly during the experiment. PTFE Tube 0,3 mm ID 0,76 mm ID was from one side glued using NOA81 adhesive (Norland Products) to in-house-made teflon male luer lock connectors (design to minimize the slide volume). The other side was connected via female luer connector to needle-free swabable valve (Nordstrom Medical). The connection was sealed using a 3 cm piece of elastic Tygon tubing 0,8 mm ID 2,8 mm OD and a drop of NOA81 on its end. Two channels on the Ibidi Slide VI 0,4 were connected and the tube with the blind end was used as an outlet to dispose the waste. 1 ml syringes were used to exchange the fluids. Short incubation (20 min) with FBS containing medium resulted in the tubing surface passivation and the losses of Lipofectamine2000 complexes were not seen.

The mRNA transfection was done directly on the microscope stage during imaging to resolve the full dynamic range of changes in cell fluorescence. Media exchange was done using customized system of tubing (Fig.A1.1). Before starting the measurement, the cells were washed with PBS and the media was exchanged to Leibovitz's L-15. Then, the tubing was connected and immediately before mRNA transfection, each condition (two channels interconnected with tubing, details presented on Fig.A1.1) was washed with OptiMEM. Right after, mRNA/Lipofectamine2000 were flushed into each channel. Cells were incubated on the heated microscopy stage at 37 °C for 30 min. Simultaneously, the siRNA/lipofectamine complexes were prepared as described above. 2x 300 mL of complexes were prepared for a single experiment (300 mL per condition). After 30 min incubation mRNA/Lipofectamine complexes were washed away and four out of six channels were filled with formed siRNA/Lipofectamine complexes for second 30min cell incubation. As a positive control mRNA-transfected cells in remaining channels were washed and incubated with Leibovitz's L-15 media for the same 30 min period. Finally, the transfection complexes were then removed by washing and the cells were re-incubated with Leibovitz's L-15, 10% (v/v) FBS media. In pDNA transfection experiments total of 110 and 131 of siRNA-treated and control Huh-7 cells respectively were analysed. Similarly, in mRNA experiments 1252 (1216) and 411 (312) of siRNA-treated (control) Huh-7 and A549 cells respectively were analysed.

A1.5.4. LISCA – translation inhibition experiments

The mRNA transfection experiments were performed according to the pipeline described in the silencing protocol except for modifications of the mRNA amounts. To prepare the transfection complexes, 148 ng of mRNA^R or 152 ng of mRNA^G was diluted in OptiMEM (Gibco) to a total volume of 150 µL. Similarly, 0.374 µL or 0.379 µL of Lipofectamine for mRNA^R and mRNA^G respectively was diluted in OptiMEM (Gibco) to a total volume of 150 µL. mRNA and Lipofectamine solutions were mixed together by pipetting and then incubated at room temperature for 20 min. The transfection was done directly on the microscope stage using the tubing system described above during the first hours of 30h-long time-lapse experiment. After 30 min of incubation, the particle-containing medium was exchanged with Leibovitz's L-15, 10% (v/v) FBS. Subsequently, during the initial phase of protein expression (after 3, 5 or 7 hours post transfection) the media was exchanged and cells were exposed to Leibovitz's L-15, medium 10% (v/v) FBS medium (Gibco) containing 15 µg mL⁻¹ cycloheximide (Thermo Fisher). Cells were

incubated with cycloheximide-containing media throughout the rest of experiment. The measurements were done in two separate experiments for eGFP and CayRFP. In all, 461 and 786 Huh-7 cells were analysed in eGFP and CayRFP experiments respectively.

A1.5.5. Protein expression and purification

To convert fluorescence intensities into numbers of eGFP and CayRFP molecules, these proteins were first expressed and purified. The eGFP or CayRFP gene sequence was cloned into the pET-23b(+) (Novagen, Merck Millipore, Darmstadt, Germany) expression vector. BL21 competent *E.coli* strain (New England Biolabs, Ipswich, MA, USA) was transformed with pET-23b(+)-eGFP or pET-23b(+)-CayRFP plasmid (plasmid maps are given in Fig.A1.4.). Both plasmids contained genes of His-tagged eGFP or CayRFP under the control of an IPTG-inducible promoter. For protein expression, an overnight culture of transformed cells was diluted 100 times up to a total volume of 50 mL in LB medium containing 0,1 mg mL⁻¹ ampicillin and incubated at 37 °C during vigorous shaking. When the culture reached 0,4 OD the cells were induced with 1 mM IPTG and incubated for 6 h at 27 °C. Subsequently cultures were centrifuged and the pellets were re-suspended in lysis buffer (50 mM NaH₂PO₄, 300 mM NaCl, 10 mM imidazole pH 8,0). For complete lysis, cells were flash frozen multiple times in liquid nitrogen, slowly thawed on ice and tip sonicated. The suspensions of lysed cells were centrifuged again and the protein-containing supernatants were filtered through sterile 0,2 µm syringe filters. The His-tagged eGFP and CayRFP were purified using HPLC (ÄKTAexplorer Box-900, General Electric). Purified proteins were then dialyzed using 3,5 K Slide-A-Lyser cassettes (Life Technologies) against PBS pH 7,4 and stored at 4 °C until further use.

A1.5.6. Plasmid and siRNA sequences, plasmid maps

GFP Duplex I siRNA:

Sense strand: 5'- GCAAGCUGACCCUGAAGUUC – 3'

Antisense strand: 5'- GAACUUCAGGGUCAGCUUGC – 3'

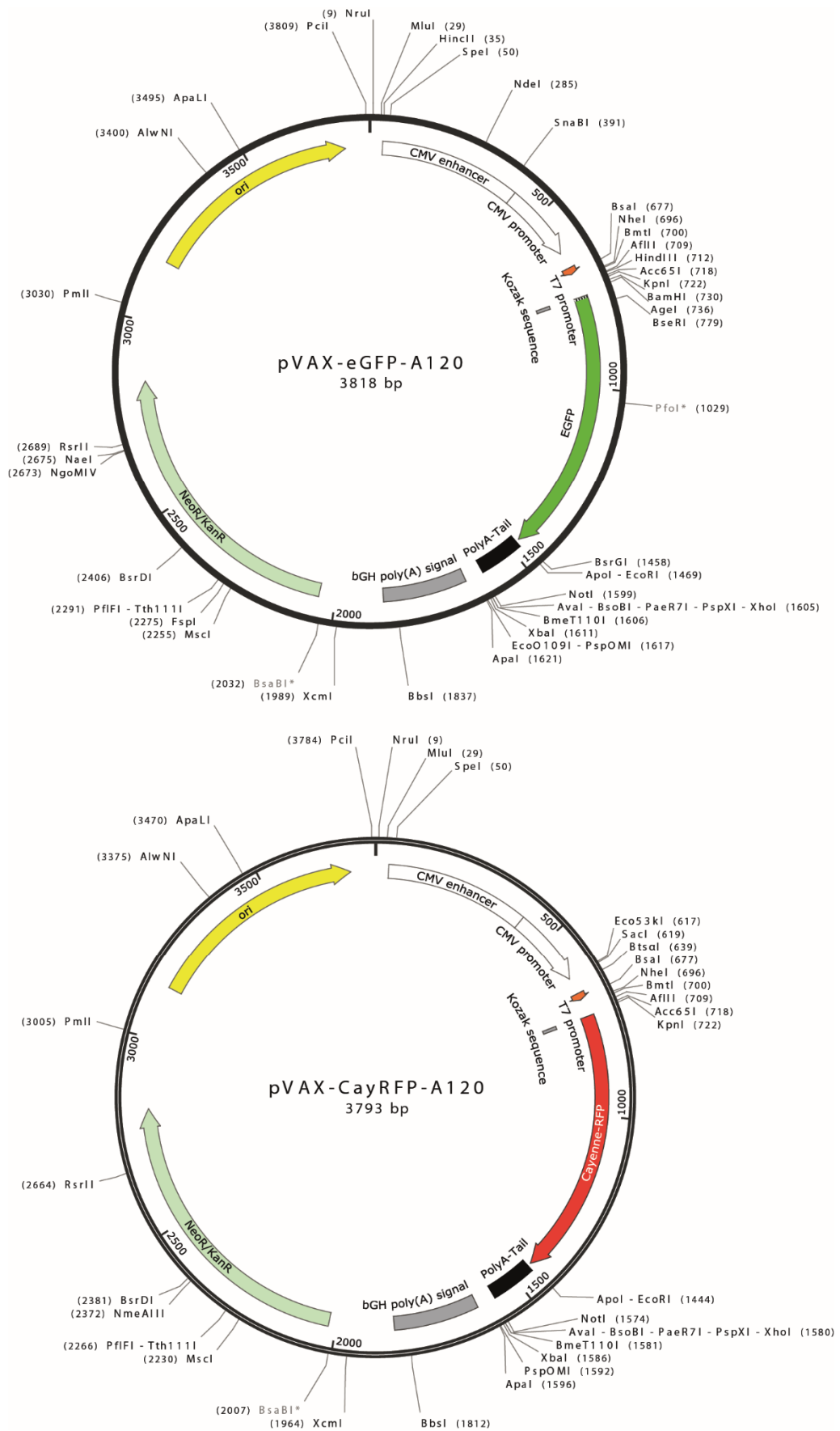


Fig.A1.3. pVAX-eGFP-A120 and pVAX-CayRFP-A120 plasmid maps

pVAX-CayRFP-A120 (3793bp)

GACTCTTCGCGATGTACGGGCCAGATATACGCGTTGACATTGATTATTGACTAGTTATTAATAGTAATCAA
 TTACGGGGTTCATTAGTTCATAGCCCATATATGGAGTTCGCGTTACATAACTTACGGTAAATGGCCCGCCT
 GGCTGACCGCCCAACGACCCCCGCCATTGACGTCAATAATGACGTATGTTCCCATAGTAACGCCAATAG
 GGACTTTCCATTGACGTCAATGGGTGGACTATTTACGGTAAACTGCCCACTTGGCAGTACATCAAGTGTAT
 CATATGCCAAGTACGCCCCCTATTGACGTCAATGACGGTAAATGGCCCGCCTGGCATTATGCCAGTACA
 TGACCTTATGGGACTTTCCTACTTGGCAGTACATCTACGTATTAGTCATCGCTATTACCATGGTGATGCGG
 TTTTGGCAGTACATCAATGGGCGTGGATAGCGGTTTGACTCACGGGGATTTCCAAAGTCTCCACCCCATTGA
 CGTCAATGGGAGTTTGTGGTGGCACAAAATCAACGGGACTTTCAAAATGTCGTAACAACCTCCGCCCCA
 TTGACGCAAAATGGGCGGTAGGCGTGTACGGTGGGAGGTCTATATAAGCAGAGCTCTCTGGCTAACTAGAG
 AACCCACTGCTTACTGGCTTATCGAAATTAATACGACTTGGGGTGGGAAGCCAAATACCGAAATGCTTCCAGCGT
 AAACCTAAGCTTGGTACCGCCACCATGGTGTCAAAAAGGGGAGGAATTGATCAAAGAGAACATGCATATG
 AAACCTGTACATGGAGGGAACCTGTCAACAATCACCACTTCAAATGCACCTCAGAGGGCGAGGGAAAAGCCC
 TACGAAGGGACCCAGACCATGCGCATTAAAGGTGGTCAAGGGCGGACCCTCCCTTTTGCATTTCGACATCC
 TGGCTACCTCCTTATGTACGGATCGCGCACTTTTATCAAGTACCCGAAGGGGATCCCGGACTTCTTCAAG
 CAATCCTTCCCTGAGGGATTCACTTGGGAACGGGTCACGACCTACGAAGATGGAGGGCTGGTGACCGTGA
 TGCAAGACACTAGCCTGGAAGATGGCTGCCTGTCTACAACGTGAAGATCAGAGGTGTGAACCTCCCATC
 CAATGGCCCCGTGATGCAGAAAAAGACTCTGGGGTGGGAAGCCAAATACCGAAATGCTTCCAGCGT
 CGGAGGACTCGAAGGCCGGTCTGACATGGCCCTGAAGCTGGTTCGAGGAGGACATTTGTCGTGTAGCTTT
 GTGACTACGTACCGGTCAAGAAAGCCGGCCAAAACCTGAAGATGCCGGGTATCCACGCGGTGGACCAT
 AGACTGGAACGCCTGGAGGAGAGCGATAACGAGATGTTTCGTTCAGAGGGAACACGCTGTGGCACGA
 TATTGCGATCTCCCGTCAAGCTTGGTCAAAAGCTCAATTAGGAATTCTGCAAAAAAAAAAAAAAAAAAAAA
 AAA
 AAA
 CCGCTGATCAGCCTGACTGTGCCTTCTAGTTGCCAGCCATCTGTTGTTTGGCCCTCCCGCTCCCTTCCT
 TGACCCTGGAAGGTGCCACTCCACTGTCTTTCCTAATAAAATGAGGAAATTGCATCGCATTGTCTGAGT
 AGGTGTCATTCTATTCTGGGGGGTGGGGTGGGGCAGGACAGCAAGGGGGAGGATTGGGAAGACAATAGC
 AGGCATGCTGGGGATGCGGTGGGCTCTATGGCTTCTACTGGGCGGTTTTATGGACAGCAAGCGAACCGGA
 ATTGCCAGCTGGGGCGCCCTCTGGTAAGGTTGGGAAGCCCTGCAAAGTAAACTGGATGGCTTCTCGCCG
 CCAAGGATCTGATGGCGCAGGGGATCAAGCTCTGATCAAGAGACAGGATGAGGATCGTTTCGCATGATT
 GAACAAGATGGATTGCACGCAAGTTCCTCCGGCCGTTGGGTGGAGAGGCTATTTCGGTATGACTGGGCAC
 AACAGACAATCGGCTGTGATGCCCGCTTCCGGCTGTCAGCGCAGGGGCGCCCGTCTTTTTGTGTC
 AAGACCGACCTGTCCGGTGCCTGAATGAATGAACTGCAAGACGAGGCAGCGCGGCTATCGTGGCTGGCCACG
 ACGGGCGTTCCTTGGCAGCTGTGCTCGACGTTGTACTGAAGCGGGAAGGGACTGGCTGCTATTGGGCG
 AAGTCCGGGGCAGGATCTCCTGTCATCTCACCTTGTCTCCTGCCGAGAAAGTATCCATCATGGCTGATGC
 AATGCGGCGGCTGCATACGCTTATCCGGCTACCTGCCCATTCGACCACCAAGCGAAACATCGCATCGAG
 CGAGCACGTACTCGGATGGAAGCCGGTCTTGTGATCAGGATGATCTGGACGAAGAGCATCAGGGGCTC
 GCGCCAGCCGAACCTGTTCCGCAAGGCTCAAGGCGAGCATGCCCGACGGCGAGGATCTCGTCGTGACCCATG
 GCGATGCCTGCTTGCCTGAATATCATGGTGGAAAATGGCCGCTTTTCTGGATTCATCGACTGTGGCCGGCTG
 GGTGTGGCGGACCGCTATCAGGACATAGCGTGGCTACCCGTGATATTGCTGAAGAGCTTGGCGCGCAAT
 GGGCTGACCGCTTCTCGTGTCTTACGGTATCGCCGCTCCCGATTTCGACGCGCATCGCCTTCTATCGCCTT
 CTTGACGAGTCTTCTGAATTATTAACGCTTACAATTTCTGATGCGGTATTTTCTCCTTACGCATCTGTGC
 GGTATTCACACCGCATAACAGGTGGCACTTTTCGGGAAATGTGCGCGGAACCCCTATTTGTTATTTTTC
 TAAATACATTCAAATATGTATCCGCTCATGAGACAATAACCCTGATAAATGCTTCAATAATAGCACGTGC
 TAAAACCTCATTTTAATTTAAAAGGATCTAGGTGAAGATCCTTTTTGATAATCTCATGACCAAAATCCCT
 TAACGTGAGTTTTCGTCCACTGAGCGTCAGACCCCGTAGAAAAGATCAAAGGATCTTCTTGAGATCCTTT
 TTTCTGCGCGTAATCTGCTGCTTGCAAAACAAAAAACCACCGCTACCAGCGGTGGTTTGTGGCCGATC
 AAGAGCTACCAACTCTTTTTCCGAAGGTAAGTGGCTTACGAGAGCGCAGATACCAATACTGTCTTCT
 AGTGTAGCCGTAGTTAGGCCACCACTTCAAGAACTCTGTAGCACCGCCTACATACCTCGCTCTGCTAATCC
 TGTTACCAGTGGCTGCTGCCAGTGGCGATAAGTCTGTGTTTACCGGGTTGGACTCAAGACGATAGTTACC
 GGATAAGGGCGCAGCGGTCCGGCTGAACGGGGGGTTCGTGCACACAGCCAGCTTGGAGCGAACGACCTA
 CACCGAACTGAGATACCTACAGCGTGAGCTATGAGAAAGCGCCACGCTTCCCGAAGGGAGAAAGGCGGA
 CAGGTATCCGGTAAGCGGCAGGGTCCGAACAGGAGAGCGCACGAGGGAGCTTCCAGGGGAAACGCTT
 GGTATCTTATAGTCTGTGCGGTTTCGCCACCTCTGACTTGAGCGTCGATTTTGTGATGCTCGTCAGGG
 GGGCGGAGCCTATGGAAAAACGCCAGCAACGCGGCTTTTTACGGTTCTGGGCTTTTGTGGCCTTTTGTG
 TCACATGTTCTT

pVAX-eGFP-A120 (3835bp)

GACTCTTCGCGATGTACGGGCCAGATATACGCGTTGACATTGATTATTGACTAGTTATTAATAGTAATCAA
 TTACGGGGTCATTAGTTCATAGCCCATATATGGAGTTCCGCGTTACATAACTTACGGTAAATGGCCCCCT
 GGCTGACCGCCCAACGACCCCCGCCATTGACGTCAATAATGACGTATGTTCCCATAGTAACGCCAATAG
 GGACTTTCCATTGACGTCAATGGGTGGACTATTTACGGTAAACTGCCCACTTGGCAGTACATCAAGTGTAT
 CATATGCCAAGTACGCCCCCTATTGACGTCAATGACGGTAAATGGCCCCGCTGGCATTATGCCAGTACA
 TGACCTTATGGGACTTTCCTACTTGGCAGTACATCTACGTATTAGTCATCGCTATTACCATGGTGTATGCGG
 TTTTGGCAGTACATCAATGGGCGTGGATAGCGTTTACTCACGGGGATTTCCAAGTCTCCACCCCATGTA
 CGTCAATGGGAGTTTGTGGTGGCACAAAATCAACGGGACTTTCAAAATGTGCTAACAACCTCCGCCCCA
 TTGACGCAAAATGGGCGGTAGGCGTGTACGGTGGGAGGTCTATATAAGCAGAGCTCTCTGGCTAACTAGAG
 AACCCACTGCTTACTGGCTTATCGAAATTAATACGACTCACTATAGGGAGACCCAAGCTGGCTAGCGTTT
 AAACCTAAGCTTGGTACCGAGCTCGGATCCACCGGTCGCCACCATGGTGAGCAAGGGCGAGGAGCTGTTT
 ACCGGGGTGGTGCCATCCTGGTCGAGCTGGACGGCGACGTAAACGGCCACAAGTTCAGCGTGTCCGGC
 GAGGGCGAGGGCGATGCCACCTACGGCAAGCTGACCTGAAGTTCATCTGCACCACCGGCAAGCTGCC
 GTGCCCTGGCCACCCTCGTGACCACCTGACCTACGGCGTGCAGTGCTCAGCCGCTACCCCGACCACA
 TGAAGCAGCAGACTTCTTCAAGTCCGCCATGCCCGAAGGCTACGTCCAGGAGCGCACCATCTTCTTCAA
 GGACGACGGCAACTACAAGACCCGCGCCGAGGTGAAGTTCGAGGGCGACACCCTGGTGAACCGCATCGA
 CGTGAAGGGCATCGACTTCAAGGAGGACGGCAACATCGACTGGGGCACAAAGCTGGAGTACAACATCAACAG
 CCACAACGTCTATATCATGGCCGACAAGCAGAAGAACGGCATCAAGGTGAACCTCAAGATCCGCCACAA
 CATCGAGGACGGCAGCGTGCAGCTCGCCGACCACTACCAGCAGAACACCCCATCGGGCAGCGCCCCGT
 GCTGCTGCCGACAACCACTACCTGAGCACCCAGTCCGCCCTGAGCAAAGACCCCAACGAGAAGCGCGA
 TCACATGGTCTGCTGGAGTTCGTGACCGCCGCCGGATCACTCTCGGCATGGACGAGCTGTACAAGTAA
 GAATTCTGCAA
 AAAGCGG
 CCGCTCGAGTCTAGAGGGCCGTTTAAACCCGCTGATCAGCCTCGACTGTGCCTTAGTTGCTAGGCCATC
 TGTTGTTTGGCCCTCCCCGTCCTTCTTACCCTGGAAGGTGCCACTCCCCTGTCTTCTTAATAAAA
 TGAGGAAATTGCATCGCATTGTCTGAGTAGGTGTCATTCTATTCTGGGGGTGGGGTGGGGCAGGACAGC
 AAGGGGGAGGATTGGGAAGACAATAGCAGGCATGCTGGGGATGCGGTGGGCTCTATGGCTTCTACTGGG
 CGGTTTTATGGACAGCAAGCGAACCAGGAAATGCCAGCTGGGGCGCCCTCTGGTAAGGTTGGGAAGCCCTG
 CAAAGTAAACTGGATGGCTTCTCGCCGCCAAGGATCTGATGGCGCAGGGGATCAAGCTCTGATCAAGAG
 ACAGGATGAGGATCGTTCGTCATGATTGACAGACAAGATGGATTGCACGCAGGTTCTCCGGCCGCTGGGTGG
 AGGGTATTTCGGTATGACTGGGCACAACAGACAACCGCTGCTGATGCCGCGTGTCCGGCTGAATGAAGTGAAGACGAG
 AGCGCAGGGGGCGCCGTTCTTTTTGTCAAGACCGACCTGTCCGGTGCCCTGAATGAAGTGAAGACGAG
 GCAGCGCGGCTATCGTGGCTGGCCACGACGGCGTTCCTTGCGCAGCTGTGCTCGACGTTGTCACTGAAG
 CGGGAAGGGACTGGCTGCTATTGGGCGAAGTGCCGGGGCAGGATCTCCTGTCATCTCACCTTGCTCCTGC
 CGAGAAAGTATCCATCATGGCTGATGCAATGCGGGCGCTGCATACGCTTGATCCGGCTACCTGCCATT
 GACCACCAAGCGAAACATCGCATCGAGCGAGCAGTACTCGGATGGAAGCCGGTCTTGTGATCAGGAT
 GATCTGGACGAAGAGCATCAGGGGCTCGCGCCAGCCGAAGTTCGCCAGGCTCAAGGGCAGCATGCC
 GACGGCGAGGATCTCGTGTGACCCATGGCGATGCCCTGCTTGCCGAATATCATGGTGGAAAATGGCCGCT
 TTTCTGGATTCATCGACTGTGGCCGGCTGGGTGTGGCGGACCGCTATCAGGACATAGCGTTGGCTACCCG
 TGATATTGCTGAAGAGCTTGGCGGCGAATGGGCTGACCGCTTCTCGTGTCTTACGGTATCGCCGCTCCCCG
 ATTCGCAGCGCATCGCCTTCTATCGCCTTCTTACGAGTCTTCTGAAATTATAACGCTTACAATTTCTGTA
 TGCGGTATTTCTCCTTACGCATCTGTGCGGTATTCACACCGCATAACAGGTGGCACTTTTCGGGGAAATG
 TCGCGGAACCCCTATTTGTTATTTTCTAAATACATTCAAATATGTATCCGCTCATGAGACAATAACCC
 TGATAAATGCTTCAATAATAGCACGTGCTAAAACCTTCAATTTTAAATTTAAAGGATCTAGGTGAAGATCCT
 TTTTGATAATCTCATGACCAAAATCCCTAACGTGAGTTTTTCGTTCCACTGAGCGTCAGACCCCGTAGAAA
 AGATCAAAGGATCTTCTGAGATCCTTTTTTCTGCGCGTAATCTGCTGCTTGCAAACAAAAAACCCG
 CTACCAGCGGTGGTTTTGTTGCCGGATCAAGAGCTACCAACTCTTTTTCCGAAGGTAAGTGGCTCAGCAG
 AGCGCAGATAACAAATACTGTCTTCTAGTGTAGCCGTAGTTAGGCCACCACTTCAAGAACTCTGTAGCA
 CCGCTACATACCTCGCTCTGCTAATCCTGTTACCAGTGGCTGCTGCCAGTGGCGATAAGTCGTGTCTTAC
 CGGGTTGGACTCAAGACGATAGTACCGGATAAGGCGCAGCGGTCCGGGCTGAACGGGGGGTTCGTGCAC
 ACAGCCCAGCTTGGAGCGAACGACCTACACCGAAGTACCTACAGCGTGAGCTATGAGAAAAGCGC
 CACGTTCCCGAAGGGAGAAAGGCGGACAGGTATCCGGTAAGCGGCAGGGTCGGAACAGGAGAGCGCA
 CGAGGGAGCTTCCAGGGGAAACGCCTGGTATCTTTATAGTCTGTGCGGGTTTCGCCACCTCTGACTTGA
 GCGTCGATTTTTGTGATGCTCGTCAGGGGGCGGAGCCTATGGAAAACGCCAGCAACGCGGCCCTTTTA
 CGGTTCTGGGCTTTTGTGCTGGCTTTTGTCTACATGTTCTT

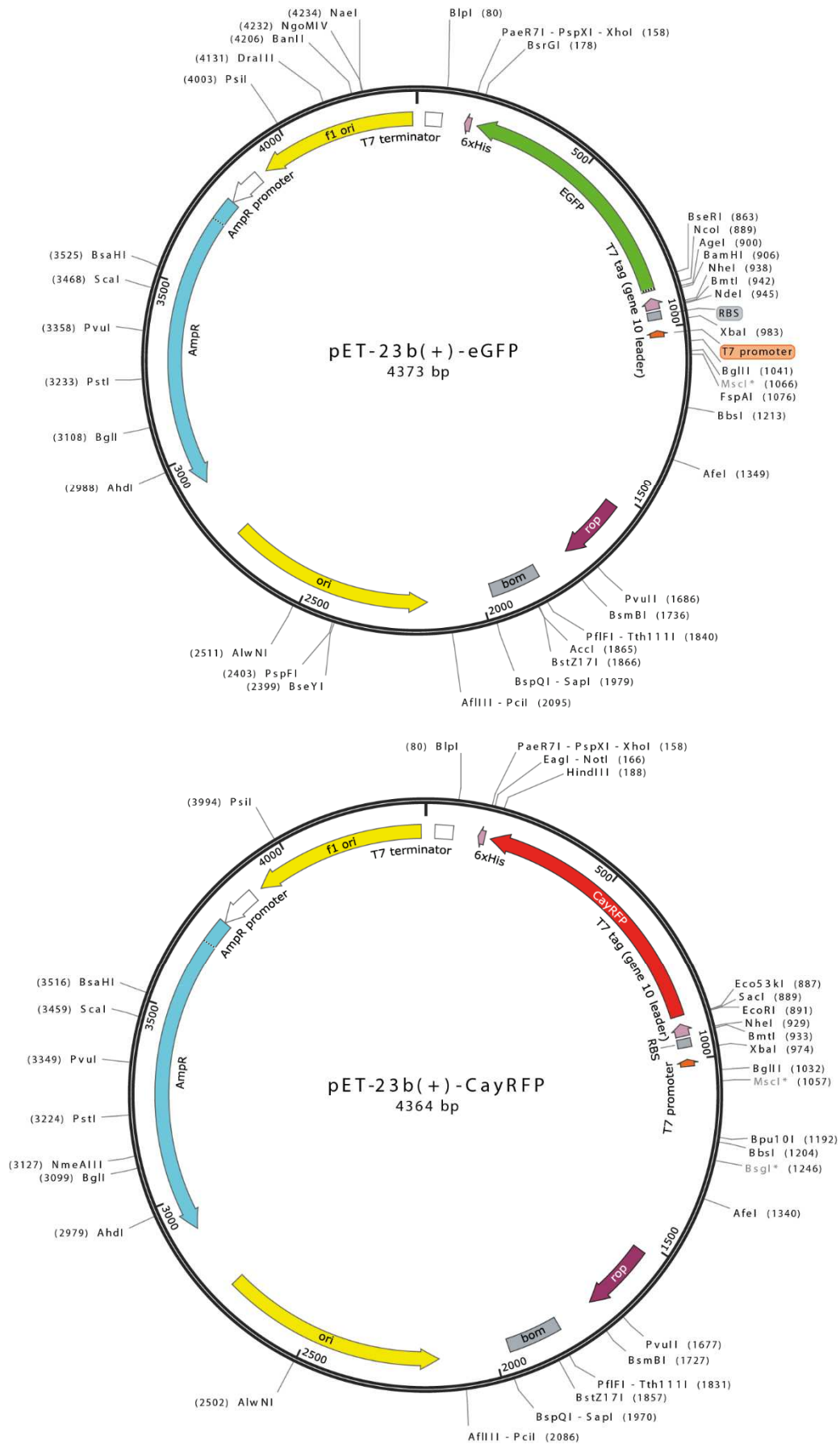


Fig.A1.4. pET-23b(+)-eGFP and pET-23b(+)-CayRFP plasmid maps

pET-23b(+)-eGFP (4373 bp)

ATCCGGATATAGTTTCCTCCTTTTCAGCAAAAAACCCCTCAAGACCCGTTTAGAGGCCCAAGGGTTATGC
 TAGTTATTGCTCAGCGGTGGCAGCAGCCAACCTCAGCTTCCTTTTCGGGCTTTGTTAGCAGCCGGATCTCAGT
 GGTGGTGGTGGTGGTGGTCTCGAGTGCCGCCGCTTTCCTGTACAGCTCGTCCATGCCGAGAGTGATCCCGGC
 GGCGGTACGAACCTCAGCAGGACCATGTGATCGCGCTTCTCGTTGGGGTCTTTGCTCAGGGCGGACTGG
 GTGCTCAGGTAGTGGTTGTCGGGCAGCAGCACGGGGCCGTCGCCGATGGGGGTGTTCTGCTGGTAGTGGT
 CGGCGAGCTGCACGCTGCCGCTCCTCGATGTTGTGGCGGATCTTGAAGTTCACCTTGATGCCGTTCTTCTGC
 TTGTCGGCCATGATATAGACGTTGTGGCTGTTGTAGTTGTACTCCAGCTTGTGCCCCAGGATGTTGCCGTC
 CTCCTTGAAGTCGATGCCCTTCAGCTCGATGCGGTTACCAGGGTGTCCGCTCGAACTTCACCTCGGGCG
 GGGTCTGTAGTTGCCGTCCTTGAAGAAGATGGTGCCTCCTGGACGTAGCCTTCGGGATGGCGGA
 CTTGAAGAAGTCGTGCTTTCATGTGGTCCGGGTAGCGGCTGAAGCACTGCACGCCGTAGGTCAGGGTG
 GTCACGAGGGTGGGCCAGGGCACGGGCAGCTTGGCGGTGGTGCAGATGAACTTCAGGGTCAGCTTGGCCG
 TAGGTGGCATCGCCCTCGCCCTCGCCGGACACGCTGAACTTGTGGCCGTTTACGTCGCCGTCAGCTCGAC
 CAGGATGGGCACCACCCCGGTGAACAGCTCCTCGCCCTTGCTACCATGGTGGCGACCCGGTGGATCCCGA
 CCCATTTGCTGTCCACCAGTCATGCTAGCCATATGTATATCTCCTTCTTAAAGTTAAACAAAATTATTTCTA
 GAGGAAACCGTTGTGGTCTCCCTATAGTGAGTCGTATTAATTTTCGCGGGATCGAGATCTCGGGCAGCGT
 TGGTCTTGGCCACGGGTGCGCATGCTGCTCCTGTGCTTGGAGACCCGGCTAGGCTGGCGGGGGTTCG
 CTTACTGTTAGCAGTAATCACCAGTACCGGATACGCGGACCGTGAAGCGACTGCTGCTGCAAAACGCTG
 CGACCTGAGCAACAACATGAATGGTCTTCGGTTCCTGTTTCGTAAGTCTGGAAACGCGGAAGTCAGC
 GCCCTGCACCATTATGTTCCGGATCTGCATCGCAGGATGCTGCTGGCTACCCTGTGGAACACCTACATCTG
 TATTAACGAAGCGCTGGCATTGACCCTGAGTGATTTTTCTCTGGTCCC GCCGATCCATACCGCCAGTTGT
 TTACCCTCACAACTTCCAGTAACCGGGCATGTTTCATCATCAGTAACCCGATCGTGAGCATCCTCTCTCG
 TTTTCATCGGTATCATTACCCCATGAACAGAAATCCCCCTTACACGGAGGCATCAGTGACCAACAGGAA
 AAAACCGCCCTTAACATGGCCCGCTTATCAGAAGCCAGACATTAACGCTTCTGGAGAACTCAACGAGC
 TGGACCGGATGAACAGGCAGACATCTGTGAATCGCTTACGACCACGCTGATGAGCTTTACCGCAGCTG
 CCTCGCGCGTTTCGGTGATGACGGTGAACCTCTGACACATGCAGCTCCCGGAGACGGTTCACAGCTTGT
 CTGTAAGCGGATGCCGGGAGCAGACAAGCCCGTCAGGGCGGTCAGCGGGTGTGGCGGGTGTGGGGC
 GCAGCCATGACCAGTCACGTAGCGATAGCGGAGTGTATACTGGCTTAACTATGCGGCATCAGAGCAGAT
 TGTACTGAGAGTGACCATATATGCGGTGTGAAATACCGCACAGATGCGTAAGGAGAAAATACCGCATC
 AGGCGCTCTCCGCTTCTCGCTCACTGACTCGCTGCGCTCGGTGCTTCCGGTGCAGGCGAGCGGTATCAGC
 TCACTCAAAGCGGTAATACGGTTATCCACAGAATCAGGGGATAACGCAGGAAAGAACATGTGAGCAAA
 AGGCAGCAAAAAGCGAGAACCGTAAAAAGCCGCTGCTGGCGTTTTTCCATAGGCTCCGCCCCCT
 GACGAGCATCACAAAATCGACGCTCAAGTCAGAGGTGAGCAGGAAACCCGACAGGACTATAAAGATACCCAG
 GCGTTTTCCCCCTGGAAGCTCCCTCGTGCCTCTCTGTTCCGACCCTGCCGCTTACCGGATACCTGTCCGC
 CTTTTCTCCCTTCGGGAAGCGTGGCGTTTTCTCATAGCTCAGCTGTAGGTATCTCAGTTCGGTGTAGGTG
 TTCGCTCCAAGCTGGGCTGTGTGCACGAACCCCGCTCAGCCCGACCGCTGCGCCTTATCCGGTAACTAT
 CGTCTTGAGTCCAACCCGGTAAGACACGACTTATCGCCACTGGCAGCAGCCACTGGTAACAGGATTAGCA
 GAGCGAGGTATGTAGGCGGTGCTACAGAGTTCTTGAAGTGGTGGCTAACTACGGCTACACTAGAAGGA
 CAGATTTGGTATCTGCGCTGTGCTGAAGCCACTTACCTCGGAAAAAGAGTTGGTAGCTCTTGTATCCGGC
 AAACAAACCACCGTGGTAGCGGTGGTTTTTTGTTTGAAGCAGCAGATTACGCGCAGAAAAAAGGAT
 CTCAAGAAGATCCTTTGATCTTTTCTACGGGGTCTGACGCTCAGTGGAACGAAAACCTACGTTAAGGGAT
 TTTGGTTCATGAGATTATCAAAAAGGATCTTACCTAGATCCTTTTAAATTAATAAATGAAGTTTTAAATCAA
 TCTAAAGTATATATGAGTAAACTTGGTCTGACAGTTACCAATGCTTAATCAGTGAGGCACCTATCTCAGC
 GATCTGTCTATTTTCGTTTCATCCATAGTTGCCTGACTCCCCGTCGTGTAGATAACTACGATACGGGAGGGCT
 TACCATCTGGCCCCAGTGTGCAATGATACCGCGAGACCCACGCTCACCAGGCTCCAGATTTATCAGCAAT
 AAACCAGCCAGCCGGAAGGGCCGAGCGCAGAAGTGGTCTGCAACTTTATCCGCCTCCATCCAGTCTATT
 AATTGTTGCCGGGAAGCTAGAGTAAGTAGTTCCGCAAGTAAATAGTTTGGCGAACGTTGTTGCCATTGCTGC
 AGGCATCGTGGTGTACGCTCGCTGTTGGTATGGCTTCACTCAGCTCCGGTTCCCAACGATCAAGGCGAG
 TTACATGATCCCCATGTTGTGCAAAAAAGCGGTTAGCTCCTTCGGTCTCCGATCGTTGTGAGAAGTAAG
 TTGGCCGAGTGTATCACTCATGGTTATGGCAGCACTGCATAATTCTTACTGTGATGCCATCCGTAAG
 ATGCTTTTCTGTGACTGGTGTGACTCAACCAAGTCATTCTGAGAATAGTGTATGCGGCGACCGAGTTGCT
 CTTGCCCGGCTCAATACGGGATAATACCGCGCCACATAGCAGAACTTTAAAAGTGCTCATCATTGGAAA
 ACGTTCTTCGGGGCGAAAACCTCAAGGATCTTACCCTGTTGAGATCCAGTTCGATGTAACCCACTCGTG
 CACCCAACTGATCTTACGATCTTTTACTTTCACCAGCGTTTCTGGGTGAGCAAAAACAGGAAGGCAAAA
 TGCCGCAAAAAGGGAATAAGGGCGACACGGAAATGTTGAATACTCATACTCTTCTTTTCAATATTAT
 TGAAGCATTTATCAGGGTTATTGTCTCATGAGCGGATACATATTTGAATGTATTTAGAAAAATAAACA
 TAGGGGTTCCGCGCACATTTCCCCGAAAAGTGCCACCTGAAATTGTAACGTTAATATTTTGTAAAATTC
 GCGTAAATTTTTGTAAAATCAGTCTATTTTTAAACCAATAGGCCGAAATCGGCAAAATCCCTTATAAATC
 AAAAGAATAGACCGAGATAGGGTGTGAGTGTGTTCCAGTTTGAACAAGAGTCCACTATTAAGAACGT
 GGACTCCAACGTCAAAGGGCGAAAACCGTCTATCAGGGCGATGGCCACTACGTGAACCATCACCTA
 ATCAAGTTTTTTGGGTCGAGGTGCCGTAAGCTACAAATCGGAACCCCTAAAGGGAGCCCGGATTTAGA
 GCTTGACGGGGAAAGCCGGCGAACGTGGCGAGAAAAGGAAGGGAAGAAAGCGAAAGGAGCGGGCGCTAG
 GGCGCTGGCAAGTGTAGCGGTACGCTGCGCGTAACCACCACACCCGCGCGCTTAAATGCGCCGCTACAG
 GGCGCTCCCATTCGCCA

Appendix.A2. Related publications

Krzysztoń, R., Salem, B., Lee, D.J., Schwake, G., Wagner, E. and Rädler, J.O. (2017) Microfluidic self-assembly of folate-targeted monomolecular siRNA-lipid nanoparticles. *Nanoscale*, 10.1039/C7NR01593C.

Westerhausen, C., Schnitzler, G.L., Wendel, D., **Krzysztoń, R.**, Lächelt, U., Wagner, E., Rädler, O.J. and Wixforth, A. (2016) Controllable Acoustic Mixing of Fluids in Microchannels for the Fabrication of Therapeutic Nanoparticles. *Micromachines*, **7**.

Krzysztoń, R., Woschée, D., Reiser, A., Schwake, G., Strey, H.H. and Rädler, J. O. (2018) Single-cell kinetics of siRNA-mediated mRNA Degradation. (*in preparation*)

Dabkowska A., Frank K., Reiser A., **Krzysztoń R.**, Yanez Arteta M., Nickel B., Rädler J.O. and Lindfors L. (2018) The pH-dependent phase transition in lipid nanoparticle cores leads to changes of protein expression in single cells. (*in preparation*)

Reiser, A., Woschée, D., Mehrotra N., **Krzysztoń, R.**, Strey, H.H. and Rädler, J. O. (2018) Time distribution of lipid-based mRNA delivery inferred from single-cell expression onsets. (*in preparation*)

Appendix.A3. Conference contributions

Krzysztoń R., Woschée D., Reiser A., Schwake G., Strey H.H. and Rädler J. O. “Single-cell kinetics of siRNA-mediated mRNA Degradation”: *Deutsche Physikalische Gesellschaft Spring Meeting*, Berlin, 2018 – poster presentation

Krzysztoń R., Salem B., Schwake G. and Rädler J. O. “Microfluidic Based Synthesis of Folate-Targeted Monomolecular siRNA-Lipid Particles”: *19th Annual Meeting of American Society of Gene and Cell Therapy (ASGCT)*, Washington, DC, 2016 – poster presentation (**outstanding poster presentation award**)

Krzysztoń R., Salem B., Schwake G. and Rädler J. O. “Microfluidic Assisted Self-Assembly of Folate-Targeted Monomolecular siRNA-lipid Particles”: *CeNS Workshop: Walk and Talk at the Nanoscale*, Venice, 2014 – poster presentation

Appendix.A4. List of abbreviations

A549	<i>human lung carcinoma A549 cells</i>
ACF	<i>Autocorrelation function</i>
AGO2	<i>Argonaute 2 protein</i>
ATTO488-dsDNA	<i>ATTO488-labelled dsDNA</i>
AzMMMan	<i>3-(azidomethyl)-4-methyl-2,5-furandione</i>
CayRFP	<i>Cayenne Red Fluorescent Protein</i>
CFP	<i>Cyan Fluorescent Protein</i>
Cy3-dsDNA	<i>Cy3-labelled dsDNA</i>
Dicer	<i>endoribonuclease Dicer</i>
DLinKC2-DMA	<i>2,2-dilinoleyl-4-(2-dimethylaminoethyl)-[1,3]-dioxolane</i>
DOPC	<i>1,2-di-(9Z-octadecenoyl)-sn-glycero-3-phosphocholine</i>
DOPE	<i>1,2-dioleoyl-sn-glycero-3-phos-phoethanolamine</i>
DOTAP	<i>1,2-dioleoyl-3-trimethylammonium-propane</i>
dsDNA	<i>double-stranded DNA</i>
dsRNA	<i>double-stranded RNA</i>
DSPE-PEG(2000)	<i>1,2-distearoyl-sn-glycero-3-phosphoethanolamine-N-[methoxy(polyethylene glycol)-2000]</i>
DSPE-PEG(2000)-FolA	<i>1,2-distearoyl-sn-glycero-3-phosphoethanolamine-N-[folate(polyethylene glycol)- 2000]</i>
Drosha	<i>Drosha ribonuclease III</i>
eGFP	<i>enhanced Green Fluorescent Protein</i>
eGFPLuc	<i>eGFP-Luciferae fusion protein</i>
FBS	<i>Fetal Bovine Serum</i>
FC	<i>Flow Cytometry</i>
FCS	<i>Fluorescence Correlation Spectroscopy</i>
FolA	<i>Folate, folic acid</i>
FolA-mNALP	<i>Folate-functionalized monomolecular Nucleic Acid/Lipid Particle</i>
GalNAc	<i>N-Acetylgalactosamine</i>
HBV	<i>Hepatitis B Virus</i>
Huh-7	<i>human hepatocellular carcinoma Huh-7 cells</i>
KB/WT	<i>wild-type human cervix carcinoma KB cells</i>
KB/eGFPLuc	<i>KB cells stably expressing eGFPLuc fusion protein</i>
LISCA	<i>Life-cell Imaging on Singe-Cell Arrays</i>
LNP	<i>Lipid Nanoparticle</i>
NA	<i>Nucleic Acid</i>
NF-κB	<i>Nuclear Factor-κB</i>
NP	<i>Nanoparticle</i>
miRNA	<i>microRNA</i>

mNALP	<i>monomolecular Nucleic Acid/Lipid Particle</i>
mRNA	<i>messenger RNA</i>
mRNA^G	<i>eGFP-encoding mRNA</i>
mRNA^R	<i>CayRFP-encoding mRNA</i>
ODE	<i>Ordinary Differential Equation</i>
PBS	<i>Phosphate Buffered Saline</i>
PCR	<i>Polymerase Chain Reaction</i>
PDMS	<i>Polydimethylsiloxane</i>
PEI	<i>Polyethylenimine</i>
pDNA	<i>plasmid DNA</i>
pDNA^G	<i>eGFP-encoding pDNA (pEGFP-N1)</i>
pDNA^R	<i>CayRFP-encoding pDNA (jpb-55-609_CayenneRFP)</i>
PEG	<i>Polyethylene glycol</i>
Pre-miRNA	<i>precursor microRNA</i>
Pri-miRNA	<i>primary microRNA</i>
RISC	<i>RNA-induced silencing complex</i>
RNAi	<i>RNA interference</i>
ROI	<i>Region Of Interest</i>
rRNA	<i>ribosomal RNA</i>
SEM	<i>Scanning Electron Microscope</i>
shRNA	<i>short hairpin RNA</i>
siGFP	<i>GFP-targeting siRNA</i>
siCtrl	<i>siRNA of randomized sequence</i>
siRNA	<i>small interfering RNA</i>
SNALP	<i>Stable Nucleic Acid/Lipid Particle</i>
tRNA	<i>transfer RNA</i>
YFP	<i>Yellow Fluorescent Protein</i>

Appendix.A5. List of figures and tables

A5.1. Figures

<i>Fig.1.1. Two major pathways of RNA interference in mammalian cells</i>	2
<i>Fig.1.2. Barriers on efficient systemic delivery of nucleic acid nanoparticles</i>	4
<i>Fig.1.3. Examples of microfluidic applications in bioscience and technology</i>	8
<i>Fig.1.4. Continuous flow microfluidic micro-mixers</i>	10
<i>Fig.1.5. Estimation of intrinsic and extrinsic cellular noise contributions</i>	12
<i>Fig.1.6. Examples of possible deterministic influence sources on cell-to-cell variability</i>	14
<i>Fig.1.7. Generic pipeline of quantitative time-lapse fluorescence microscopy experiment</i>	15
<i>Fig.1.8. Strategies for organizing single cells into spatial arrays</i>	17
<i>Fig.2.1. Hydrodynamic focusing chip design</i>	19
<i>Fig.2.2. Bright-field and fluorescence images of the T-junction during mixing</i>	21
<i>Fig.2.3. Bright-field and fluorescence images of first 6 turns of meandering outlet channel</i>	22
<i>Fig.2.4. Fluorescence calibration chip design</i>	23
<i>Fig.2.5. Typical confocal-microscopy-based setup for fluorescence (cross-)correlation spectroscopy</i>	30
<i>Fig.2.6. Simplified representation of the flow cytometry setup</i>	32
<i>Fig.2.7. Experimental workflow of live-cell imaging of single-cell arrays (LISCA)</i>	34
<i>Fig.2.8. Micro-pattern production – master structure and workflow</i>	35
<i>Fig.2.9. ImageJ plugin used for quantitative image analysis</i>	37
<i>Fig.2.10. Fluorescence calibration for conversion of single-cell fluorescence intensities into the numbers of expressed proteins</i>	38
<i>Fig.3.1. Structure and assembly of mNALPs in a hydrodynamic focussing chip device</i> ...	42
<i>Fig.3.2. Evaluation of starting solvent conditions</i>	44
<i>Fig.3.3. Effects of mixing mode – optimal charge ratio and DNA concentration</i>	46
<i>Fig.3.4. Detailed view of particle formation at optimal DNA concentration ($c_{DNA} = 40$ nM)</i>	47
<i>Fig.3.5. Effects of mixing mode on – encapsulation efficiency and sample homogeneity</i> .	48
<i>Fig.3.6. Effects of particle functionalization with Fola on mNALP formation</i>	49
<i>Fig.3.7. Effects of water evaporation on mNALP stability</i>	49

<i>Fig.3.8. Effects of serum/plasma concentration on diffusive behaviour of Cy3 and Cy3-dsDNA</i>	50
<i>Fig.3.9. Stability of Fola-mNALPs in blood serum and plasma</i>	51
<i>Fig.3.10. The shelf life time of Fola-mNALPs</i>	51
<i>Fig.3.11. Specific binding and uptake of Fola-mNALPs - confocal microscopy</i>	52
<i>Fig.3.12. Studies of dose dependence on Fola-mNALP binding and uptake by folate-receptor-overexpressing KB/WT cells</i>	53
<i>Fig.3.13. Studies of time dependence on Fola-mNALP binding and uptake by folate-receptor-overexpressing KB/WT cells</i>	54
<i>Fig.3.14. Quantification of silencing efficiency of Fola-mNALPs in KB cells expressing the eGFPLuc fusion protein (KB/eGFPLuc cells)</i>	56
<i>Fig.3.15. Dual-reporter assay in time-lapse fluorescence imaging experiments</i>	58
<i>Fig.3.16. The schematic representations of eGFP- and CayRFP-mRNA sequence constructs</i>	59
<i>Fig.3.17. Single-cell pDNA expression dynamics</i>	60
<i>Fig.3.18. Single-cell vs. population-averaged fluorescence analysis – silencing efficiency</i>	61
<i>Fig.3.19. Single-cell fluorescence analysis – population distributions</i>	62
<i>Fig.3.20. Single-cell mRNA expression kinetics in the presence of siRNA</i>	63
<i>Fig.3.21. Identifiability of fit parameters</i>	65
<i>Fig.3.22. Translation block experiments – single-cell time-courses and mathematical model</i>	66
<i>Fig.3.23. Population distributions of the maturation (k_m) and degradation (β) rate constants for CayRFP and eGFP</i>	67
<i>Fig.3.24. Single-cell correlations between parameters obtained from eGFP and CayRFP time-courses (m_0k_{tl} and t_0)</i>	69
<i>Fig.3.25. Correlation dot-plots of expression onset times t_0 and initial translation rate m_0k_{tl} (m_0k_{tl} vs. t_0)</i>	70
<i>Fig.3.26. Correlation analysis of mRNA degradation constants (δ)</i>	72
<i>Fig.3.27. Occurrences of codons encoding different amino acids as found in used eGFP and CayRFP coding sequences</i>	75
<i>Fig.3.28. Calculated dependence between CayRFP- and eGFP-mRNA degradation constants (δ^G vs. δ^R) overlaid with experimental data</i>	76

<i>Fig.A1.1. Crafted system of tubing used to exchange the fluids inside the microscopy slide</i>	89
<i>Fig.A1.2. pEGFP-N1 (pDNA^G) and fpb-55-609_CayenneRFP (pDNA^R) plasmid maps ..</i>	92
<i>Fig.A1.3. pVAX-eGFP-A120 and pVAX-CayRFP-A120 plasmid maps</i>	93
<i>Fig.A1.4. pET-23b(+)-eGFP and pET-23b(+)-CayRFP plasmid maps.....</i>	96

A5.2. Tables

<i>Tab.1. Fit parameters obtained during fluorescence calibration and used in fluorescence conversion into numbers of proteins.....</i>	39
<i>Tab.2. Experimental and theoretical diffusion coefficients of naked 21-bp ds DNA.....</i>	45
<i>Tab.3. Mean degradation (β) and maturation kinetic constants (k_m) (and related half-times τ_β and τ_m)</i>	68
<i>Tab.4. mRNA degradation rate constants δ (and related half-times τ_δ).....</i>	73

Acknowledgements

Firstly, I would like to express my sincere gratitude to my advisor **Prof. Dr. Joachim O. Rädler** for the continuous support of my Ph.D study and related research, for his patience, motivation, and immense knowledge.

Besides my advisor, I would like to thank: **Prof. Dr. Ernst Wagner, Prof. Dr. Helmut H. Strey, Dr. Frank Jaschinski, Dr. Lennart Lindfors, Dr. Ulrich Lächelt, Dr. Stefan Wuttke** and **Prof. Dr. Achim Wixforth** for their insightful comments and encouragement, but also for the hard question which incited me to widen my research from various perspectives.

My sincere thanks also goes to my collaborators: **Dr. Dian-Jang Lee, Anita Reiser, Daniel Woschée, Kilian Frank, Gerlinde Schwake, Dr. Aleksandra Dabkowska, Alexandra Götz, Christoph Westerhausen, Dominik Wendel, Patrick Hirschle, Lucas Schnitzler** and **Thomas Nicolaus**. Without their precious support it would not be possible to conduct this research.

I thank all of my friends and fellow labmates (list of whom is substantially longer than the length of presented thesis) for the stimulating discussions, for warm welcoming in the first months and for all the fun we have had in the last years.

From the depth of my heart, I would like to thank my mother for constantly supporting me in all of my endeavours. Finally, I would like to thank my father, who always kept showing me the right path and whom led me to the point I am standing at now.

Bibliography

1. Guerrier-Takada,C., Gardiner,K., Marsh,T., Pace,N. and Altman,S. (1983) The RNA moiety of ribonuclease P is the catalytic subunit of the enzyme. *Cell*, **35**, 849–857.
2. Matranga,C. and Zamore,P.D. (2007) Small silencing RNAs. *Curr Biol*, **17**, R789–R793.
3. Fire,A., Xu,S., Montgomery,M.K., Kostas,S.A., Driver,S.E. and Mello,C.C. (1998) Potent and specific genetic interference by double-stranded RNA in caenorhabditis elegans. *Nature*, **391**, 806–811.
4. Zamore,P.D., Tuschl,T., Sharp,P.A. and Bartel,D.P. (2000) RNAi: double-stranded RNA directs the ATP-dependent cleavage of mRNA at 21 to 23 nucleotide intervals. *Cell*, **101**, 25–33.
5. Napoli,C. (1990) Introduction of a Chimeric Chalcone Synthase Gene into Petunia Results in Reversible Co-Suppression of Homologous Genes in trans. *Plant Cell Online*, **2**, 279–289.
6. van der Krol,A.R. (1990) Flavonoid Genes in Petunia: Addition of a Limited Number of Gene Copies May Lead to a Suppression of Gene Expression. *Plant Cell Online*, **2**, 291–299.
7. Volpe,T. (2002) Regulation of heterochromatic silencing and histone H3 Lysine-9 by RNAi. *Science (80-.)*, **297**, 1833–1837.
8. McManus,M.T. and Sharp,P.A. (2002) Gene silencing in mammals by small interfering RNAs. *Nat. Rev. Genet.*, **3**, 737–747.
9. Chiu,Y.-L. and Rana,T.M. (2002) RNAi in human cells: basic structural and functional features of small interfering RNA. *Mol. Cell*, **10**, 549–561.
10. Fougerolles,A. De (2007) Interfering with disease: a progress report on siRNA-based therapeutics. *Nat. Rev. Drug Discov.*, **6**, 443–453.
11. Elbashir,S.M., Harborth,J., Lendeckel,W., Yalcin,A., Weber,K. and Tuschl,T. (2001) Duplexes of 21 ± nucleotide RNAs mediate RNA interference in cultured mammalian cells. *Nature*, **411**, 494–498.
12. Chen,C., Li,L., Lodish,H.F. and Bartel,D.P. (2004) Lineage Differentiation. *Science (80-.)*, **303**, 83–6.
13. Hashimi,S.T., Fulcher,J. a, Chang,M.H., Gov,L., Wang,S. and Lee,B. (2009) MicroRNA profiles identify miR-34a and miR-21 and their target genes. *Differentiation*, **114**, 404–414.
14. Suh,N., Baehner,L., Moltzahn,F., Melton,C., Shenoy,A., Chen,J. and Blelloch,R. (2010) MicroRNA Function Is Globally Suppressed in Mouse Oocytes and Early Embryos. *Curr. Biol.*, **20**, 271–277.
15. Wienholds,E., Kloosterman,W.P., Miska,E., Alvarez-saavedra,E., Berezikov,E., Bruijn,E. De, Horvitz,H.R., Kauppinen,S. and Plasterk,R.H. (2005) MicroRNA Expression in Zebrafish Embryonic Development Ant Nestmate and Non-Nestmate Discrimination by a Chemosensory Sensillum. *Science (80-.)*, **309**, 310–311.
16. Pulito,C., Donzelli,S., Muti,P., Puzzo,L., Strano,S. and Blandino,G. (2014) microRNAs and cancer metabolism reprogramming: the paradigm of metformin. *Ann. Transl. Med.*, **2**, 58.
17. Tomasetti,M., Lee,W., Santarelli,L. and Neuzil,J. (2017) Exosome-derived microRNAs in cancer metabolism: possible implications in cancer diagnostics and therapy. *Exp. Mol. Med.*, **49**, e285.
18. Di Leva,G. and Croce,C.M. (2013) MiRNA profiling of cancer. *Curr. Opin. Genet. Dev.*, **23**, 3–11.
19. Obbard,D.J., Gordon,K.H., Buck,A.H. and Jiggins,F.M. (2009) The evolution of RNAi as a defence against viruses and transposable elements. *Philos. Trans. R. Soc. B Biol. Sci.*, **364**, 99–115.
20. Haasnoot,J., Westerhout,E.M. and Berkhout,B. (2007) RNA interference against viruses: Strike and counterstrike. *Nat. Biotechnol.*, **25**, 1435–1443.
21. Lodish,H.F., Zhou,B., Liu,G. and Chen,C.Z. (2008) Micromanagement of the immune system by microRNAs. *Nat. Rev. Immunol.*, **8**, 120–130.
22. Welker,N.C., Habig,J.W. and Bass,B.L. (2007) Genes misregulated in *C. elegans* deficient in Dicer, RDE-4, or RDE-1 are enriched for innate immunity genes. *Rna*, **13**, 1090–1102.
23. Ding,S.W. and Voinnet,O. (2007) Antiviral Immunity Directed by Small RNAs. *Cell*, **130**, 413–426.
24. Li,H., Li,W.X. and Ding,S.W. (2002) Induction and suppression of RNA silencing by an animal virus. *Science (80-.)*, **296**, 1319–1321.

25. Tang,F., Kaneda,M., O'Carroll,D., Hajkova,P., Barton,S.C., Sun,Y.A., Lee,C., Tarakhovsky,A., Lao,K. and Surani,M.A. (2007) Maternal microRNAs are essential for mouse zygotic development. *Genes Dev.*, **21**, 644–648.
26. Murchison,E.P., Stein,P., Xuan,Z., Pan,H., Zhang,M.Q., Schultz,R.M. and Hannon,G.J. (2007) Critical roles for Dicer in the female germline. *Genes Dev.*, **21**, 682–693.
27. Echeverri,C.J. and Perrimon,N. (2006) High-throughput RNAi screening in cultured cells: a user's guide. *Nat. Rev. Genet.*, **7**, 373–384.
28. Mohr,S.E. and Perrimon,N. (2012) RNAi screening: New approaches, understandings, and organisms. *Wiley Interdiscip. Rev. RNA*, **3**, 145–158.
29. Reynolds,A., Leake,D., Boese,Q., Scaringe,S., Marshall,W.S. and Khvorova,A. (2004) Rational siRNA design for RNA interference. *Nat. Biotechnol.*, **22**, 326–330.
30. Hutvagner,G. and Zamore,P.D. (2002) A microRNA in a Multiple-Turnover RNAi Enzyme Complex. *Science (80-.)*, **297**, 2056 LP-2060.
31. Bartlett,D.W. and Davis,M.E. (2006) Insights into the kinetics of siRNA-mediated gene silencing from live-cell and live-animal bioluminescent imaging. *Nucleic Acids Res.*, **34**, 322–333.
32. Grimm,D., Streetz,K.L., Jopling,C.L., Storm,T.A., Pandey,K., Davis,C.R., Marion,P., Salazar,F. and Kay,M.A. (2006) Fatality in mice due to oversaturation of cellular microRNA/short hairpin RNA pathways. *Nature*, **441**, 537–541.
33. Sato,Y., Murase,K., Kato,J., Kobune,M., Sato,T., Kawano,Y., Takimoto,R., Takada,K., Miyanishi,K., Matsunaga,T., *et al.* (2008) Resolution of liver cirrhosis using vitamin A-coupled liposomes to deliver siRNA against a collagen-specific chaperone. *Nat. Biotechnol.*, **26**, 431–442.
34. Song,E., Lee,S.-K., Wang,J., Ince,N., Ouyang,N., Min,J., Chen,J., Shankar,P. and Lieberman,J. (2003) RNA interference targeting Fas protects mice from fulminant hepatitis. *Nat. Med.*, **9**, 347.
35. Halder,J., Kamat,A.A., Landen,C.N., Han,L.Y., Lutgendorf,S.K., Lin,Y.G., Merritt,W.M., Jennings,N.B., Chavez-Reyes,A., Coleman,R.L., *et al.* (2006) Focal adhesion kinasetargeting using in vivo short interfering RNA delivery in neutral liposomes for ovarian carcinoma therapy. *Clin. Cancer Res.*, **12**, 4916–4924.
36. Takeshita,F., Minakuchi,Y., Nagahara,S., Honma,K., Sasaki,H., Hirai,K., Teratani,T., Namatame,N., Yamamoto,Y., Hanai,K., *et al.* (2005) Efficient delivery of small interfering RNA to bone-metastatic tumors by using atelocollagen in vivo. *Proc. Natl. Acad. Sci. U. S. A.*, **102**, 12177–82.
37. Frank-Kamenetsky,M., Grefhorst,A., Anderson,N.N., Racie,T.S., Bramlage,B., Akinc,A., Butler,D., Charisse,K., Dorkin,R., Fan,Y., *et al.* (2008) Therapeutic RNAi targeting PCSK9 acutely lowers plasma cholesterol in rodents and LDL cholesterol in nonhuman primates. *Proc. Natl. Acad. Sci.*, **105**, 11915–11920.
38. Burnett,J.C. and Rossi,J.J. (2012) RNA-based therapeutics: Current progress and future prospects. *Chem. Biol.*, **19**, 60–71.
39. DiFiglia,M., Sena-Esteves,M., Chase,K., Sapp,E., Pfister,E., Sass,M., Yoder,J., Reeves,P., Pandey,R.K., Rajeev,K.G., *et al.* (2007) Therapeutic silencing of mutant huntingtin with siRNA attenuates striatal and cortical neuropathology and behavioral deficits. *Proc. Natl. Acad. Sci.*, **104**, 17204–17209.
40. de Fougères,A. and Novobrantseva,T. (2008) siRNA and the lung: research tool or therapeutic drug? *Curr. Opin. Pharmacol.*, **8**, 280–285.
41. Li,W. and Szoka,F.C. (2007) Lipid-based nanoparticles for nucleic acid delivery. *Pharm. Res.*, **24**, 438–49.
42. Barquinero,J., Eixarch,H. and Pérez-Melgosa,M. (2004) Retroviral vectors: New applications for an old tool. *Gene Ther.*, **11**, S3–S9.
43. Yun,Y.H., Lee,B.K. and Park,K. (2015) Controlled Drug Delivery: Historical perspective for the next generation. *J. Control. Release*, **219**, 2–7.
44. Koltover,I. (1998) An Inverted Hexagonal Phase of Cationic Liposome-DNA Complexes Related to DNA Release and Delivery. *Science (80-.)*, **281**, 78–81.
45. Semple,S.C., Akinc,A., Chen,J., Sandhu,A.P., Mui,B.L., Cho,C.K., Sah,D.W.Y., Stebbing,D., Crosley,E.J., Yaworski,E., *et al.* (2010) Rational design of cationic lipids for siRNA delivery. *Nat. Biotechnol.*, **28**, 172–6.
46. Akinc,A., Thomas,M., Klibanov,A.M. and Langer,R. (2005) Exploring polyethylenimine-mediated DNA transfection and the proton sponge hypothesis. *J. Gene Med.*, **7**, 657–663.

47. Morrissey,D. V, Lockridge,J. a, Shaw,L., Blanchard,K., Jensen,K., Breen,W., Hartsough,K., Macheimer,L., Radka,S., Jadhav,V., *et al.* (2005) Potent and persistent in vivo anti-HBV activity of chemically modified siRNAs. *Nat. Biotechnol.*, **23**, 1002–7.
48. Akinc,A., Zumbuehl,A., Goldberg,M., Leshchiner,E.S., Busini,V., Hossain,N., Bacallado,S. a, Nguyen,D.N., Fuller,J., Alvarez,R., *et al.* (2008) A combinatorial library of lipid-like materials for delivery of RNAi therapeutics. *Nat. Biotechnol.*, **26**, 561–9.
49. Belliveau,N.M., Huft,J., Lin,P.J., Chen,S., Leung,A.K., Leaver,T.J., Wild,A.W., Lee,J.B., Taylor,R.J., Tam,Y.K., *et al.* (2012) Microfluidic Synthesis of Highly Potent Limit-size Lipid Nanoparticles for In Vivo Delivery of siRNA. *Mol. Ther. Nucleic Acids*, **1**, e37.
50. Ogris,M., Steinlein,P., Carotta,S., Brunner,S. and Wagner,E. (2001) DNA/polyethylenimine transfection particles: influence of ligands, polymer size, and PEGylation on internalization and gene expression. *AAPS PharmSci*, **3**, E21.
51. Immordino,M.L., Dosio,F. and Cattel,L. (2006) Stealth liposomes: review of the basic science, rationale, and clinical applications, existing and potential. *Int. J. Nanomedicine*, **1**, 297–315.
52. Hayes,M.E., Drummond,D.C., Kirpotin,D.B., Zheng,W.W., Noble,C.O., Park,J.W., Marks,J.D., Benz,C.C. and Hong,K. (2006) Genospheres: self-assembling nucleic acid-lipid nanoparticles suitable for targeted gene delivery. *Gene Ther.*, **13**, 646–51.
53. Mui,B.L., Tam,Y.K., Jayaraman,M., Ansell,S.M., Du,X., Tam,Y.Y.C., Lin,P.J., Chen,S., Narayanannair,J.K., Rajeev,K.G., *et al.* (2013) Influence of polyethylene glycol lipid desorption rates on pharmacokinetics and pharmacodynamics of siRNA lipid nanoparticles. *Mol. Ther. Nucleic Acids*, **2**, e139.
54. Maier,K. and Wagner,E. (2012) Acid-labile traceless click linker for protein transduction. *J. Am. Chem. Soc.*, **134**, 10169–73.
55. Hatakeyama,H., Akita,H., Ito,E., Hayashi,Y., Oishi,M., Nagasaki,Y., Danev,R., Nagayama,K., Kaji,N., Kikuchi,H., *et al.* (2011) Systemic delivery of siRNA to tumors using a lipid nanoparticle containing a tumor-specific cleavable PEG-lipid. *Biomaterials*, **32**, 4306–4316.
56. Dohmen,C., Edinger,D., Fröhlich,T., Schreiner,L., Lächelt,U., Troiber,C., Rädler,J., Hadwiger,P., Vornlocher,H.P. and Wagner,E. (2012) Nanosized multifunctional polyplexes for receptor-mediated siRNA delivery. *ACS Nano*, **6**, 5198–5208.
57. Gabizon,A., Horowitz,A.T., Goren,D., Tzemach,D., Mandelbaum-shavit,F., Qazen,M.M. and Zalipsky,S. (1999) Targeting Folate Receptor with Folate Linked to Extremities of Poly (ethylene glycol) -Grafted Liposomes : In Vitro Studies. *Bioconjug. Chem.*, **10**, 289–298.
58. Leamon,C.P. and Low,P.S. (1991) Delivery of macromolecules into living cells: a method that exploits folate receptor endocytosis. *Proc. Natl. Acad. Sci. U. S. A.*, **88**, 5572–6.
59. Akinc,A., Querbes,W., De,S., Qin,J., Frank-Kamenetsky,M., Jayaprakash,K.N., Jayaraman,M., Rajeev,K.G., Cantley,W.L., Dorkin,J.R., *et al.* (2010) Targeted delivery of RNAi therapeutics with endogenous and exogenous ligand-based mechanisms. *Mol. Ther.*, **18**, 1357–1364.
60. Soutschek,J., Akinc,A., Bramlage,B., Charisse,K., Constien,R., Donoghue,M., Elbashir,S., Geick,A., Hadwiger,P., Harborth,J., *et al.* (2004) Therapeutic silencing of an endogenous gene by systemic administration of modified siRNAs. *Nature*, **432**, 173–178.
61. Paulos,C.M., Reddy,J. a, Leamon,C.P., Turk,M.J. and Low,P.S. (2004) Ligand binding and kinetics of folate receptor recycling in vivo: impact on receptor-mediated drug delivery. *Mol. Pharmacol.*, **66**, 1406–1414.
62. Gaumet,M., Vargas,A., Gurny,R. and Delie,F. (2008) Nanoparticles for drug delivery: The need for precision in reporting particle size parameters. *Eur. J. Pharm. Biopharm.*, **69**, 1–9.
63. Ernsting,M.J., Murakami,M., Roy,A. and Li,S.D. (2013) Factors controlling the pharmacokinetics, biodistribution and intratumoral penetration of nanoparticles. *J. Control. Release*, **172**, 782–794.
64. Cabral,H., Matsumoto,Y., Mizuno,K., Chen,Q., Murakami,M., Kimura,M., Terada,Y., Kano,M.R., Miyazono,K., Uesaka,M., *et al.* (2011) Accumulation of sub-100 nm polymeric micelles in poorly permeable tumours depends on size. *Nat. Nanotechnol.*, **6**, 815–823.
65. Jain,R.K. and Stylianopoulos,T. (2010) Delivering nanomedicine to solid tumors. *Nat. Rev. Clin. Oncol.*, **7**, 653–64.
66. Karnik,R., Gu,F., Basto,P., Cannizzaro,C., Dean,L., Kyei-Manu,W., Langer,R. and Farokhzad,O.C. (2008) Microfluidic platform for controlled synthesis of polymeric nanoparticles. *Nano Lett.*, **8**, 2906–12.

67. Zhigaltsev, I. V., Belliveau, N., Hafez, I., Leung, A.K.K., Huft, J., Hansen, C. and Cullis, P.R. (2012) Bottom-up design and synthesis of limit size lipid nanoparticle systems with aqueous and triglyceride cores using millisecond microfluidic mixing. *Langmuir*, **28**, 3633–3640.
68. Zhigaltsev, I. V., Tam, Y.K., Leung, A.K.K. and Cullis, P.R. (2015) Production of limit size nanoliposomal systems with potential utility as ultra-small drug delivery agents. *J. Liposome Res.*, **2104**, 1–7.
69. Jahn, A., Reiner, J.E., Vreeland, W.N., DeVoe, D.L., Locascio, L.E. and Gaitan, M. (2008) Preparation of nanoparticles by continuous-flow microfluidics. *J. Nanoparticle Res.*, **10**, 925–934.
70. Leung, A.K.K., Hafez, I.M., Baoukina, S., Belliveau, N.M., Zhigaltsev, I. V., Afshinmanesh, E., Tieleman, D.P., Hansen, C.L., Hope, M.J. and Cullis, P.R. (2012) Lipid nanoparticles containing siRNA synthesized by microfluidic mixing exhibit an electron-dense nanostructured core. *J. Phys. Chem. C*, **116**, 18440–18450.
71. Whitesides, G.M. (2006) The origins and the future of microfluidics. *Nature*, **442**, 368–373.
72. Ong, S.E., Zhang, S., Du, H.J. and Fu, Y.Q. (2008) Fundamental principles and applications of microfluidic systems. *Front. Biosci.*, **13**, 2757–2773.
73. Teh, S.Y., Lin, R., Hung, L.H. and Lee, A.P. (2008) Droplet microfluidics. *Lab Chip*, **8**, 198–220.
74. Nie, Z., Li, W., Seo, M., Xu, S. and Kumacheva, E. (2006) Janus and ternary particles generated by microfluidic synthesis: Design, synthesis, and self-assembly. *J. Am. Chem. Soc.*, **128**, 9408–9412.
75. Wyatt Shields Iv, C., Reyes, C.D. and López, G.P. (2015) Microfluidic cell sorting: A review of the advances in the separation of cells from debulking to rare cell isolation. *Lab Chip*, **15**, 1230–1249.
76. Terray, A., Oakey, J. and Marr, D.W.M. (2002) Microfluidic Control Using Colloidal Devices. *Science (80-.)*, **296**, 1841 LP-1844.
77. Jeon, N.L., Dertinger, S.K.W., Chiu, D.T., Choi, I.S., Stroock, A.D. and Whitesides, G.M. (2000) Generation of solution and surface gradients using microfluidic systems. *Langmuir*, **16**, 8311–8316.
78. Suh, Y.K. and Kang, S. (2010) A review on mixing in microfluidics. *Micromachines*, **1**, 82–111.
79. Zheng, B., Tice, J.D., Roach, L.S. and Ismagilov, R.F. (2004) A droplet-based, composite PDMS/glass capillary microfluidic system for evaluating protein crystallization conditions by microbatch and vapor-diffusion methods with on-chip X-ray diffraction. *Angew. Chemie - Int. Ed.*, **43**, 2508–2511.
80. Zheng, B., Roach, L.S. and Ismagilov, R.F. (2003) Screening of protein crystallization conditions on a microfluidic chip using nanoliter-size droplets. *J. Am. Chem. Soc.*, **125**, 11170–11171.
81. Carlo, D. Di, Wu, L.Y. and Lee, L.P. (2006) Dynamic single cell culture array. *Lab Chip*, **6**, 1445–1449.
82. Chung, B.G., Flanagan, L.A., Rhee, S.W., Schwartz, P.H., Lee, A.P., Monuki, E.S. and Jeon, N.L. (2005) Human neural stem cell growth and differentiation in a gradient-generating microfluidic device. *Lab Chip*, **5**, 401–406.
83. McDonald, J.C., Duffy, D.C., Anderson, J.R., Chiu, D.T., Wu, H., Schueller, O.J. and Whitesides, G.M. (2000) Fabrication of microfluidic systems in poly(dimethylsiloxane). *Electrophoresis*, **21**, 27–40.
84. Haeberle, S., Mark, D., Von Stetten, F. and Zengerle, R. (2012) Microfluidic platforms for lab-on-a-chip applications. *Microsystems Nanotechnol.*, **9783642182938**, 853–895.
85. Liu, J., Fu, H., Yang, T. and Li, S. (2015) Automatic sequential fluid handling with multilayer microfluidic sample isolated pumping. *Biomicrofluidics*, **9**, 1–9.
86. Mogensen, K.B., Klank, H. and Kutter, J.P. (2004) Recent developments in detection for microfluidic systems. *Electrophoresis*, **25**, 3498–3512.
87. Ottesen, E.A., Hong, J.W., Quake, S.R. and Leadbetter, J.R. (2006) Microfluidic Digital PCR Enables Multigene Analysis of Individual Environmental Bacteria. *Science (80-.)*, **314**, 1464 LP-1467.
88. Lagally, E.T., Medintz, I. and Mathies, R.A. (2001) Single-molecule DNA amplification and analysis in an integrated microfluidic device. *Anal. Chem.*, **73**, 565–570.
89. Zeng, Y., Novak, R., Shuga, J., Smith, M.T. and Mathies, R.A. (2008) High-Performance Single Cell Genetic Analysis Using Microfluidic Emulsion Generator Arrays. *Anal. Chem.*, **xxx**, 117–124.
90. Kalisky, T. and Quake, S.R. (2011) Single-cell genomics. *Nat. Methods*, **8**, 311–314.
91. Abdallah, B.G., Roy-Chowdhury, S., Fromme, R., Fromme, P. and Ros, A. (2016) Protein Crystallization in an Actuated Microfluidic Nanowell Device. *Cryst. Growth Des.*, **16**, 2074–2082.

92. Scheler, O., Pacocha, N., Debski, P.R., Ruszczak, A., Kaminski, T.S. and Garstecki, P. (2017) Optimized droplet digital CFU assay (ddCFU) provides precise quantification of bacteria over a dynamic range of 6logs and beyond. *Lab Chip*, **17**, 1980–1987.
93. McMullen, J.P. and Jensen, K.F. (2011) Rapid determination of reaction kinetics with an automated microfluidic system. *Org. Process Res. Dev.*, **15**, 398–407.
94. Stratz, S., Eyer, K., Kurth, F. and Dittrich, P.S. (2014) On-chip enzyme quantification of single Escherichia coli bacteria by immunoassay-based analysis. *Anal. Chem.*, **86**, 12375–12381.
95. Huh, D., Matthews, B.D., Mammoto, A., Montoya-Zavala, M., Hsin, H.Y. and Ingber, D.E. (2010) Reconstituting Organ-Level Lung Functions on a Chip. *Science (80-.)*, **328**, 1662 LP-1668.
96. Ziółkowska, K., Kwapiszewski, R. and Brzózka, Z. (2011) Microfluidic devices as tools for mimicking the in vivo environment. *New J. Chem.*, **35**, 979–990.
97. Mahto, S.K., Yoon, T.H. and Rhee, S.W. (2010) A new perspective on in vitro assessment method for evaluating quantum dot toxicity by using microfluidics technology. *Biomicrofluidics*, **4**.
98. van der Helm, M.W., van der Meer, A.D., Eijkel, J.C.T., van den Berg, A. and Segerink, L.I. (2016) Microfluidic organ-on-chip technology for blood-brain barrier research. *Tissue Barriers*, **4**.
99. Kim, H.J., Huh, D., Hamilton, G. and Ingber, D.E. (2012) Human gut-on-a-chip inhabited by microbial flora that experiences intestinal peristalsis-like motions and flow. *Lab Chip*, **12**, 2165–2174.
100. Toh, Y.C., Lim, T.C., Tai, D., Xiao, G., Van Noort, D. and Yu, H. (2009) A microfluidic 3D hepatocyte chip for drug toxicity testing. *Lab Chip*, **9**, 2026–2035.
101. Yin, H. and Marshall, D. (2012) Microfluidics for single cell analysis. *Curr. Opin. Biotechnol.*, **23**, 110–119.
102. Di Carlo, D., Aghdam, N. and Lee, L.P. (2006) Single-cell enzyme concentrations, kinetics, and inhibition analysis using high-density hydrodynamic cell isolation arrays. *Anal. Chem.*, **78**, 4925–4930.
103. Brouzes, E., Medkova, M., Savenelli, N., Marran, D., Twardowski, M., Hutchison, J.B., Rothberg, J.M., Link, D.R., Perrimon, N. and Samuels, M.L. (2009) Droplet microfluidic technology for single-cell high-throughput screening. *Proc. Natl. Acad. Sci.*, **106**, 14195–14200.
104. Valencia, P. and Farokhzad, O. (2012) Microfluidic technologies for accelerating the clinical translation of nanoparticles. *Nat.*, **7**, 623–629.
105. Besson, C., Finney, E.E. and Finke, R.G. (2005) A mechanism for transition-metal nanoparticle self-assembly. *J. Am. Chem. Soc.*, **127**, 8179–8184.
106. Gu, F.X., Karnik, R., Wang, A.Z., Alexis, F., Levy-Nissenbaum, E., Hong, S., Langer, R.S. and Farokhzad, O.C. (2007) Targeted nanoparticles for cancer therapy. *Nano Today*, **2**, 14–21.
107. Bringer, M.R., Gerds, C.J., Song, H., Tice, J.D. and Rustem, F. (2003) Microfluidic Systems for Chemical Kinetics That Rely on Chaotic Mixing in Droplets Ismagilov Source : Philosophical Transactions : Mathematical , Physical and Engineering Sciences , Vol . Published by : Royal Society Stable URL : <http://www.jstor.org/stab.362>, 1087–1104.
108. Marre, S. and Jensen, K.F. (2010) Synthesis of micro and nanostructures in microfluidic systems. *Chem. Soc. Rev.*, **39**, 1183–1202.
109. Kikkeri, R., Laurino, P., Odedra, A. and Seeberger, P.H. (2010) Synthesis of carbohydrate-functionalized quantum dots in microreactors. *Angew. Chemie - Int. Ed.*, **49**, 2054–2057.
110. Shestopalov, I., Tice, J.D. and Ismagilov, R.F. (2004) Multi-step synthesis of nanoparticles performed on millisecond time scale in a microfluidic droplet-based system. *Lab Chip*, **4**, 316–321.
111. Stroock, A.D., Dertinger, S.K.W., Ajdari, A., Mezić, I., Stone, H.A. and Whitesides, G.M. (2002) Chaotic Mixer for Microchannels. *Science (80-.)*, **295**, 647 LP-651.
112. Johnson, B.K. and Prud'homme, R.K. (2003) Mechanism for rapid self-assembly of block copolymer nanoparticles. *Phys. Rev. Lett.*, **91**, 1–4.
113. Nguyen, J., Walsh, C.L., Motion, J.P.M., Perttu, E.K. and Szoka, F. (2012) Controlled nucleation of lipid nanoparticles. *Pharm. Res.*, **29**, 2236–48.
114. Chen, T., Hynninen, A., Prud'homme, R.K., Kevrekidis, I.G. and Panagiotopoulos, A.Z. (2008) Coarse-Grained Simulations of Rapid Assembly Kinetics for Polystyrene-. *J. Phys. Chem. B*, **112**, 16357–16366.

115. Capretto,L., Cheng,W., Hill,M. and Zhang,X. (2011) Micromixing Within Microfluidic Devices. In Lin,B. (ed), *Microfluidics: Technologies and Applications*. Springer Berlin Heidelberg, Berlin, Heidelberg, pp. 27–68.
116. Belliveau,N.M., Huft,J., Lin,P.J., Chen,S., Leung,A.K., Leaver,T.J., Wild,A.W., Lee,J.B., Taylor,R.J., Tam,Y.K., *et al.* (2012) Microfluidic Synthesis of Highly Potent Limit-size Lipid Nanoparticles for In Vivo Delivery of siRNA. *Mol. Ther. Nucleic Acids*, **1**, e37.
117. Lee,J.B., Zhang,K., Tam,Y.Y.C., Tam,Y.K., Belliveau,N.M., Sung,V.Y.C., Lin,P.J.C., LeBlanc,E., Ciufolini,M.A., Rennie,P.S., *et al.* (2012) Lipid nanoparticle siRNA systems for silencing the androgen receptor in human prostate cancer in vivo. *Int. J. Cancer*, **131**.
118. Taniguchi,Y., Choi,P.J., Li,G., Chen,H., Babu,M., Hearn,J., Emili,A. and Xie,X.S. (2011) Sensitivity in Single Cells. *Science*, **329**, 533–539.
119. Smits,W.K., Kuipers,O.P. and Veening,J.-W. (2006) Phenotypic variation in bacteria: the role of feedback regulation. *Nat. Rev. Microbiol.*, **4**, 259–271.
120. Elowitz,M.B., Levine,A.J., Siggia,E.D. and Swain,P.S. (2002) Stochastic gene expression in a single cell. *Science*, **297**, 1183–1186.
121. Raj,A. and van Oudenaarden,A. (2009) Single-Molecule Approaches to Stochastic Gene Expression. *Annu. Rev. Biophys.*, **38**, 255–270.
122. Eldar,A. and Elowitz,M.B. (2010) Functional roles for noise in genetic circuits. *Nature*, **467**, 167–173.
123. Ben-Jacob,E. and Schultz,D. (2010) Bacteria determine fate by playing dice with controlled odds. *Proc. Natl. Acad. Sci. U. S. A.*, **107**, 13197–8.
124. Thattai,M. and van Oudenaarden,A. (2001) Intrinsic noise in gene regulatory networks. *Proc. Natl. Acad. Sci.*, **98**, 8614–8619.
125. Tian,T. and Burrage,K. (2006) Stochastic models for regulatory networks of the genetic toggle switch. *Proc. Natl. Acad. Sci.*, **103**, 8372–8377.
126. Newman,J.R.S., Ghaemmaghami,S., Ihmels,J., Breslow,D.K., Noble,M., DeRisi,J.L. and Weissman,J.S. (2006) Single-cell proteomic analysis of *S. cerevisiae* reveals the architecture of biological noise. *Nature*, **441**, 840–846.
127. Shahrezaei,V., Ollivier,J.F. and Swain,P.S. (2008) Colored extrinsic fluctuations and stochastic gene expression. *Mol. Syst. Biol.*, **4**, 1–9.
128. Volfson,D., Marciniak,J., Blake,W.J., Ostroff,N., Tsimring,L.S. and Hasty,J. (2006) Origins of extrinsic variability in eukaryotic gene expression. *Nature*, **439**, 861–864.
129. Lestas,I., Vinnicombe,G. and Paulsson,J. (2010) Fundamental limits on the suppression of molecular fluctuations. *Nature*, **467**, 174–178.
130. Stelling,J., Sauer,U., Szallasi,Z., Doyle,F.J. and Doyle,J. (2004) Robustness of cellular functions. *Cell*, **118**, 675–685.
131. Sopko,R., Huang,D., Preston,N., Chua,G., Papp,B., Kafadar,K., Snyder,M., Oliver,S.G., Cyert,M., Hughes,T.R., *et al.* (2006) Mapping pathways and phenotypes by systematic gene overexpression. *Mol. Cell*, **21**, 319–330.
132. Isalan,M., Lemerle,C., Michalodimitrakis,K., Horn,C., Beltrao,P., Raineri,E., Garriga-Canut,M. and Serrano,L. (2008) Evolvability and hierarchy in rewired bacterial gene networks. *Nature*, **452**, 840–845.
133. Singh,D.K., Ku,C.J., Wichaidit,C., Steining,R.J., Wu,L.F. and Altschuler,S.J. (2010) Patterns of basal signaling heterogeneity can distinguish cellular populations with different drug sensitivities. *Mol. Syst. Biol.*, **6**, 1–10.
134. Cohen,A.A., Eden,E., Issaeva,I., Sigal,A., Milo,R., Liron,Y., Kam,Z., Cohen,L., Danon,T., Perzov,N., *et al.* (2008) Dynamic Proteomics of Individual Cancer Cells in Response to a Drug. *Science (80-)*, **322**, 1511–1517.
135. Spencer,S.L., Gaudet,S., Albeck,J.G., Burke,J.M. and Sorger,P.K. (2009) Non-genetic origins of cell-to-cell variability in TRAIL-induced apoptosis. *Nature*, **459**, 428–432.
136. Smith,Z.D., Nachman,I., Regev,A. and Meissner,A. (2010) Dynamic single-cell imaging of direct reprogramming reveals an early specifying event. *Nat. Biotechnol.*, **28**, 521–526.
137. Ungrin,M.D., Joshi,C., Nica,A., Bauwens,C. and Zandstra,P.W. (2008) Reproducible, ultra high-throughput formation of multicellular organization from single cell suspension-derived human embryonic stem cell aggregates. *PLoS One*, **3**.
138. Dennis E. Discher, David J. Mooney and Peter W. Zandstra (2009) Growth factors, matrices, and forces combine

- and control stem cells. *Science* (80-.), **324**, 1673–1677.
139. Brock,A., Chang,H. and Huang,S. (2009) Non-genetic heterogeneity a mutation-independent driving force for the somatic evolution of tumours. *Nat. Rev. Genet.*, **10**, 336–342.
140. Hoek,K.S., Eichhoff,O.M., Schlegel,N.C., Döbbeling,U., Kobert,N., Schaerer,L., Hemmi,S. and Dummer,R. (2008) In vivo switching of human melanoma cells between proliferative and invasive states. *Cancer Res.*, **68**, 650–656.
141. Roesch,A., Fukunaga-Kalabis,M., Schmidt,E.C., Zabierowski,S.E., Brafford,P.A., Vultur,A., Basu,D., Gimotty,P., Vogt,T. and Herlyn,M. (2010) A Temporarily Distinct Subpopulation of Slow-Cycling Melanoma Cells Is Required for Continuous Tumor Growth. *Cell*, **141**, 583–594.
142. Zeng,L., Skinner,S.O., Zong,C., Sippy,J., Feiss,M. and Golding,I. (2010) Decision Making at a Subcellular Level Determines the Outcome of Bacteriophage Infection. *Cell*, **141**, 682–691.
143. Snijder,B., Sacher,R., Rämö,P., Damm,E.-M., Liberali,P. and Pelkmans,L. (2009) Population context determines cell-to-cell variability in endocytosis and virus infection. *Nature*, **461**, 520–523.
144. Tay,S., Hughey,J.J., Lee,T.K., Lipniacki,T., Quake,S.R. and Covert,M.W. (2010) Single-cell NF-B dynamics reveal digital activation and analogue information processing. *Nature*, **466**, 267–271.
145. Colman-Lerner,A., Gordon,A., Serra,E., Chin,T., Resnekov,O., Endy,D., Pesce,C.G. and Brent,R. (2006) Erratum: Regulated cell-to-cell variation in a cell-fate decision system. *Nature*, **439**, 502–502.
146. Yu,R.C., Pesce,C.G., Colman-Lerner,A., Lok,L., Pincus,D., Serra,E., Holl,M., Benjamin,K., Gordon,A. and Brent,R. (2008) Negative feedback that improves information transmission in yeast signalling. *Nature*, **456**, 755–761.
147. Waters,C.M. and Bassler,B.L. (2005) QUORUM SENSING: Cell-to-Cell Communication in Bacteria. *Annu. Rev. Cell Dev. Biol.*, **21**, 319–346.
148. Blango,M.G. and Mulvey,M.A. (2009) Bacterial landlines: contact-dependent signaling in bacterial populations. *Curr. Opin. Microbiol.*, **12**, 177–181.
149. Danino,T., Tsimring,L., Hasty,J., Diego,S., Jolla,L., Diego,S., Jolla,L., Section,B. and Diego,S. (2010) A synchronized quorum of genetic clocks. **463**, 326–330.
150. Balaban,N.Q., Merrin,J., Chait,R., Kowalik,L. and Leibler,S. (2004) Bacterial Persistence as a Phenotypic Switch. *Science* (80-.), **305**, 1622–1625.
151. Snijder,B. and Pelkmans,L. (2011) Origins of regulated cell-to-cell variability. *Nat. Rev. Mol. Cell Biol.*, **12**, 119–125.
152. Slack,M.D., Martinez,E.D., Wu,L.F. and Altschuler,S.J. (2008) Characterizing heterogeneous cellular responses to perturbations. *Proc. Natl. Acad. Sci.*, **105**, 19306–19311.
153. Sharma,S. V., Lee,D.Y., Li,B., Quinlan,M.P., Takahashi,F., Maheswaran,S., McDermott,U., Azizian,N., Zou,L., Fischbach,M.A., *et al.* (2010) A Chromatin-Mediated Reversible Drug-Tolerant State in Cancer Cell Subpopulations. *Cell*, **141**, 69–80.
154. Gascoigne,K.E. and Taylor,S.S. (2008) Cancer Cells Display Profound Intra- and Interline Variation following Prolonged Exposure to Antimitotic Drugs. *Cancer Cell*, **14**, 111–122.
155. Campbell,L.L. and Polyak,K. (2007) Breast tumor heterogeneity: Cancer stem cells or clonal evolution? *Cell Cycle*, **6**, 2332–2338.
156. Neumann,B., Walter,T., Hériché,J.K., Bulkescher,J., Erfle,H., Conrad,C., Rogers,P., Poser,I., Held,M., Liebel,U., *et al.* (2010) Phenotypic profiling of the human genome by time-lapse microscopy reveals cell division genes. *Nature*, **464**, 721–727.
157. Pepperkok,R. and Ellenberg,J. (2006) High-throughput fluorescence microscopy for systems biology Rainer. *Nat. Rev. Mol. Cell Biol.*, **7**, 690–696.
158. Gordon,A., Colman-Lerner,A., Chin,T.E., Benjamin,K.R., Yu,R.C. and Brent,R. (2007) Single-cell quantification of molecules and rates using open-source microscope-based cytometry. *Nat. Methods*, **4**, 175–181.
159. Elowitz,M.B. (2010) Stochastic Gene Expression in a Single Cell. **1183**.
160. Leonhardt,C., Schwake,G., Stögbauer,T.R., Rapp,S., Kuhr,J.-T., Ligon,T.S. and Rädler,J.O. (2014) Single-cell mRNA transfection studies: delivery, kinetics and statistics by numbers. *Nanomedicine*, **10**, 679–88.

161. Lidstrom, M.E. and Meldrum, D.R. (2003) Life-on-a-chip. *Nat. Rev. Microbiol.*, **1**, 158–164.
162. Neumann, B., Held, M., Liebel, U. and Erfle, H. (2006) High-throughput RNAi screening by time-lapse imaging of live human cells. *Nat. ...*, **3**, 385–390.
163. Ando, H., Hirose, M., Kurosawa, G., Impey, S. and Mikoshiba, K. (2017) Time-lapse imaging of microRNA activity reveals the kinetics of microRNA activation in single living cells. *Sci. Rep.*, **7**, 1–16.
164. Young, J.W., Locke, J.C.W., Altinok, A., Rosenfeld, N., Bacarian, T., Swain, P.S., Mjolsness, E. and Elowitz, M.B. (2011) Measuring single-cell gene expression dynamics in bacteria using fluorescence time-lapse microscopy. *Nat. Protoc.*, **7**, 80–88.
165. Ferizi, M., Leonhardt, C., Meggle, C., Aneja, M.K., Rudolph, C., Plank, C. and Rädler, J.O. (2015) Stability analysis of chemically modified mRNA using micropattern-based single-cell arrays. *Lab Chip*, **15**, 3561–3571.
166. Perlman, Z.E., Slack, M.D., Feng, Y., Mitchison, T.J., Lani, F. and Altschuler, S.J. (2016) Multidimensional Drug Profiling by Automated Microscopy Published by : American Association for the Advancement of Science Stable URL : <http://www.jstor.org/stable/3839493>. **306**, 1194–1198.
167. Xiaowei, C., Xiaobo, Z. and Stephen, W. (2006) Automated Segmentation, Classification, and Tracking of Cancer Cell Nuclei in Time-Lapse Microscopy. *Nucleus*, **53**, 762–766.
168. Rettig, J.R. and Folch, A. (2005) Large-Scale Single-Cell Trapping And Imaging Using Microwell Arrays. **77**, 5628–5634.
169. Röttgermann, P.J.F., Alberola, A.P. and Rädler, J.O. (2014) Cellular self-organization on micro-structured surfaces. *Soft Matter*, **10**, 2397–404.
170. Reiser, A., Zorn, M.L., Murschhauser, A. and Joachim Oskar Rädler (2018) Single Cell Microarrays Fabricated by Microscale Plasma-Initiated Protein Patterning (μ PIPP). In *Cell-Based Microarrays: Methods and Protocols*. Vol. 1771, p. 41-.
171. Wood, D.K., Weingeist, D.M., Bhatia, S.N. and Engelward, B.P. (2010) Single cell trapping and DNA damage analysis using microwell arrays. *Proc. Natl. Acad. Sci.*, **107**, 10008–10013.
172. Röttgermann, P.J.F., Dawson, K.A. and Rädler, J.O. (2016) Time-Resolved Study of Nanoparticle Induced Apoptosis Using Microfabricated Single Cell Arrays. 10.3390/microarrays5020008.
173. Schauer, K., Duong, T., Bleakley, K., Bardin, S., Bornens, M. and Goud, B. (2010) Probabilistic density maps to study global endomembrane organization. *Nat. Methods*, **7**, 560.
174. Ochsner, M., Dusseiller, M.R., Grandin, H.M., Luna-Morris, S., Textor, M., Vogel, V. and Smith, M.L. (2007) Microwell arrays for 3D shape control and high resolution analysis of single cells. *Lab Chip*, **7**, 1074–1077.
175. Krzysztoń, R., Salem, B., Lee, D.J., Schwake, G., Wagner, E. and Rädler, J.O. (2017) Microfluidic self-assembly of folate-targeted monomolecular siRNA-lipid nanoparticles. *Nanoscale*, 10.1039/C7NR01593C.
176. Jahn, A., Vreeland, W.N., Locascio, L.E. and Gaitan, M. (2004) Controlled Vesicle Self-Assembly in Continuous Two Phase Flow Microfluidic Channels. *Hilt. Head*.
177. Tosun, I., Uner, D. and Ozgen, C. (1988) Critical Reynolds Number for Newtonian Flow in Rectangular Ducts. *Ind. Eng. Chem. Res.*, **27**, 1955–1957.
178. Debus, J.D., Mendoza, M. and Herrmann, H.J. (2014) Dean instability in double-curved channels. *Phys. Rev. E - Stat. Nonlinear, Soft Matter Phys.*, **90**, 1–10.
179. Petrov, E.P. and Schwille, P. (2008) State of the art and novel trends in fluorescence correlation spectroscopy. *...and Qual. Assur. Fluoresc. ...*, 10.1007/4243.
180. Loudon, R. (1973) The quantum theory of light / Rodney Loudon Clarendon Press, Oxford.
181. Saleh, B. (1978) Photoelectron statistics, with applications to spectroscopy and optical communication Springer-Verlag, Berlin ; New York.
182. Kapusta, P. and Gmbh, P. (2010) Absolute Diffusion Coefficients : Compilation of Reference Data for FCS Calibration.
183. Petrášek, Z. and Schwille, P. (2008) Precise Measurement of Diffusion Coefficients using Scanning Fluorescence Correlation Spectroscopy. *Biophys. J.*, **94**, 1437–1448.
184. Holt, B. Van Der (2007) CSF flow cytometry greatly improves diagnostic accuracy in CNS hematologic malignancies.

185. Vignali, D.A.A. (2000) Multiplexed particle-based flow cytometric assays. **243**, 243–255.
186. Davey, H.M. and Kell, D.B. (1996) Flow Cytometry and Cell Sorting of Heterogeneous Microbial Populations: the Importance of Single-Cell Analyses. **60**, 641–696.
187. Zamai, L., Zauli, G. and Cataldi, A. (1993) Optimal Detection of Apoptosis by Flow Cytometry Depends on Cell Morphology'. **897**.
188. Mateus, C. and Avery, S. V (2000) Destabilized green fluorescent protein for monitoring dynamic changes in yeast gene expression with flow cytometry.
189. Mcmanus, M.T., Petersen, C.P., Haines, B.B., Chen, J. and Sharp, P.A. (2002) Gene silencing using micro-RNA designed hairpins.
190. Stricker, J., Cookson, S., Bennett, M.R., Mather, W.H., Tsimring, L.S. and Hasty, J. (2008) A fast, robust and tunable synthetic gene oscillator. *Nature*, **456**, 516–519.
191. Vermes, I., Haanen, C. and Reutelingsperger, C. (2000) Flow cytometry of apoptotic cell death. **243**, 167–190.
192. Riccardi, C. and Nicoletti, I. (2006) Analysis of apoptosis by propidium iodide staining and flow cytometry. 10.1038/nprot.2006.238.
193. Hawkins, B.J. and Madesh, M. (2007) Simultaneous detection of apoptosis and mitochondrial superoxide production in live cells by flow cytometry and confocal microscopy. **2**, 2295–2301.
194. Shattil, S.J., Cunningham, M. and Hoxie, J.A. (1987) Detection of activated platelets in whole blood using activation-dependent monoclonal antibodies and flow cytometry. *Blood*, **70**, 307 LP-315.
195. Benedict, C.A., Mackrell, A.J. and Anderson, W.F. (1997) Determination of the binding affinity of an anti-CD34 single-chain antibody using a novel flow cytometry based assay.
196. Röttgermann, P.J.F., Hertrich, S., Berts, I., Albert, M., Segerer, F.J., Moulin, J.F., Nickel, B. and Rädler, J.O. (2014) Cell motility on polyethylene glycol block copolymers correlates to fibronectin surface adsorption. *Macromol. Biosci.*, **14**, 1755–1763.
197. Schwarzfischer, M., Marr, C., Krumsiek, J., Hoppe, P.S., Schroeder, T. and Theis, F.J. (2011) Efficient fluorescence image normalization for time lapse movies. In *Proc. Microscopic Image Analysis with Applications in Biology*. Heidelberg, Germany, pp. 5–5.
198. Ester, M., Kriegel, H.P., Sander, J. and Xu, X. (1996) A Density-Based Algorithm for Discovering Clusters in Large Spatial Databases with Noise. *Proc. 2nd Int. Conf. Knowl. Discov. Data Min.*, 10.1.1.71.1980.
199. Rudorf, S. and Rädler, J.O. (2012) Self-assembly of stable monomolecular nucleic acid lipid particles with a size of 30 nm. *J. Am. Chem. Soc.*, **134**, 11652–11658.
200. Woodle, M.C. and Lasic, D.D. (1992) Sterically stabilized liposomes. *Biochim. Biophys. Acta - Rev. Biomembr.*, **1113**, 171–199.
201. Tirado, M.M., Martínez, C.L. and de la Torre, J.G. (1984) Comparison of theories for the translational and rotational diffusion coefficients of rod-like macromolecules. Application to short DNA fragments. *J. Chem. Phys.*, **81**, 2047–2052.
202. Jackson, A.L. and Linsley, P.S. (2010) Recognizing and avoiding siRNA off-target effects for target identification and therapeutic application. *Nat. Rev. Drug Discov.*, **9**, 57–67.
203. Tschuch, C., Schulz, A., Pscherer, A., Werft, W., Benner, A., Hotz-Wagenblatt, A., Barrionuevo, L.S., Lichter, P. and Mertens, D. (2008) Off-target effects of siRNA specific for GFP. *BMC Mol. Biol.*, **9**, 1–14.
204. Maiwald, T., Timmer, J., Kreutz, C., Klingmüller, U. and Raue, A. (2011) Addressing parameter identifiability by model-based experimentation. *IET Syst. Biol.*, **5**, 120–130.
205. Hammond, S.M. (2005) Dicing and slicing: the core machinery of the RNA interference pathway. *FEBS Lett.*, **579**, 5822–9.
206. Haley, B. and Zamore, P.D. (2004) Kinetic analysis of the RNAi enzyme complex. *Nat. Struct. Mol. Biol.*, **11**, 599–606.
207. van den Berg, A., Mols, J. and Han, J. (2008) RISC-target interaction: Cleavage and translational suppression. *Biochim. Biophys. Acta - Gene Regul. Mech.*, **1779**, 668–677.
208. Wang, Y. and Huang, L. (2013) A window onto siRNA delivery. *Nat. Biotechnol.*, **31**, 611–612.

209. Wittrup,A., Ai,A., Liu,X., Hamar,P., Trifonova,R., Charisse,K., Manoharan,M., Kirchhausen,T. and Lieberman,J. (2015) Visualizing lipid-formulated siRNA release from endosomes and target gene knockdown. *Nat. Biotechnol.*, **33**, 1–9.
210. Presnyak,V., Alhusaini,N., Graveley,B.R., Collier,J., Presnyak,V., Alhusaini,N., Chen,Y., Martin,S., Morris,N., Kline,N., *et al.* (2015) Codon Optimality Is a Major Determinant of mRNA Article Codon Optimality Is a Major Determinant of mRNA Stability. *Cell*, **160**, 1111–1124.
211. Harigaya,Y. and Parker,R. (2016) Codon optimality and mRNA decay. *Cell Res.*, **26**, 1269–1270.
212. Cheng,J., Maier,K.C., Avsec,Ž., Rus,P. and Gagneur,J. (2017) *Cis* -regulatory elements explain most of the mRNA stability variation across genes in yeast. *Rna*, **23**, 1648–1659.
213. Hanson,G. and Collier,J. (2018) Translation and Protein Quality Control: Codon optimality, bias and usage in translation and mRNA decay. *Nat. Rev. Mol. Cell Biol.*, **19**, 20–30.
214. Radhakrishnan,A., Chen,Y., Martin,S., Alhusaini,N., Green,R., Collier,J., Radhakrishnan,A., Chen,Y., Martin,S., Alhusaini,N., *et al.* (2016) The DEAD-Box Protein Dhh1p Couples mRNA Decay and Translation by Monitoring Codon Optimality Article The DEAD-Box Protein Dhh1p Couples mRNA Decay and Translation by Monitoring Codon Optimality. *Cell*, **167**, 122–128.e9.
215. Mishima,Y. and Tomari,Y. (2016) Codon Usage and 3' UTR Length Determine Maternal mRNA Stability in Zebrafish Article Codon Usage and 3' UTR Length Determine Maternal mRNA Stability in Zebrafish. *Mol. Cell*, **61**, 874–885.
216. Koutmou,K.S. and Radhakrishnan,A. (2015) Synthesis at the Speed of Codons. *Trends Biochem. Sci.*, **40**, 717–718.
217. Viswanathan,P., Chen,J., Chiang,Y. and Denis,C.L. (2003) Identification of Multiple RNA Features That Influence CCR4 Deadenylation Activity *. **278**, 14949–14955.
218. Kalek,M., Jemielity,J., Darzynkiewicz,Z.M., Bojarska,E., Stepinski,J., Stolarski,R., Davis,E. and Darzynkiewicz,E. (2006) Enzymatically stable 5' mRNA cap analogs : Synthesis and binding studies with human DcpS decapping enzyme. **14**, 3223–3230.
219. Balatsos,N.A.A., Anastasakis,D., Stathopoulos,C., Balatsos,N.A.A., Anastasakis,D. and Stathopoulos,C. (2009) Inhibition of human poly (A) -specific ribonuclease (PARN) by purine nucleotides : kinetic analysis. **6366**.
220. Banerjee,H., Palenchar,J.B., Lukaszewicz,M., Bojarska,E., Stepinski,J., Jemielity,J., Guranowski,A., Ng,S., Wah,D.A., Darzynkiewicz,E., *et al.* (2009) Identification of the HIT-45 protein from *Trypanosoma brucei* as an FHIT protein / dinucleoside triphosphatase : Substrate specificity studies on the recombinant and endogenous proteins. 10.1261/rna.1426609.hypermethylated.
221. Westerhausen,C., Schnitzler,G.L., Wendel,D., Krzysztoń,R., Lächelt,U., Wagner,E., Rädler,O.J. and Wixforth,A. (2016) Controllable Acoustic Mixing of Fluids in Microchannels for the Fabrication of Therapeutic Nanoparticles. *Micromachines*, **7**.
222. Chan,C.L., Majzoub,R.N., Shirazi,R.S., Ewert,K.K., Chen,Y.J., Liang,K.S. and Safinya,C.R. (2012) Endosomal escape and transfection efficiency of PEGylated cationic liposome-DNA complexes prepared with an acid-labile PEG-lipid. *Biomaterials*, **33**, 4928–4935.
223. Tavernier,G., Andries,O., Demeester,J., Sanders,N.N., De Smedt,S.C. and Rejman,J. (2011) mRNA as gene therapeutic: How to control protein expression. *J. Control. Release*, **150**, 238–247.
224. Kormann,M.S.D., Hasenpusch,G., Aneja,M.K., Nica,G., Flemmer,A.W., Herber-Jonat,S., Huppmann,M., Mays,L.E., Illenyi,M., Schams,A., *et al.* (2011) Expression of therapeutic proteins after delivery of chemically modified mRNA in mice. *Nat. Biotechnol.*, **29**, 154–159.